Simplified Physics Package for Atmospheric Global Climate Models

Climatology of a Simplified Atmospheric Model: Coupling a Simple Dry Physics Package to a Dynamically Adaptive Dynamical Core

By Gabrielle Ching-Johnson, B.Sc.

A Thesis Submitted to the School of Graduate Studies in the Partial Fulfillment of the Requirements for the Degree Master of Science

McMaster University
Master of Science (2023)
Hamilton, Ontario (Computational Sciences and Engineering)

TITLE: Climatology of a Simplified Atmospheric Model: Coupling a Simple Dry Physics Package to a Dynamically Adaptive Dynamical Core
AUTHOR: Gabrielle Ching-Johnson (McMaster University)
SUPERVISOR: Dr. Nicholas Kevlahan
NUMBER OF PAGES: xi, 109

Abstract

Over the years, global climate modelling has advanced, aiming for realistic and precise models by increasing their complexity. An integral component of climate models, the physics parameterizations, are a major limitation, but are required due to limited computational power. Grid adaptivity is an avenue that is being explored to mitigate these challenges, but comes with its own difficulties. For example, the question of whether the physics should be "scale-aware", by adjusting according to the resolution and the fact that parameterizations are optimized for specific grid ranges. To research these challenges, test cases that work in both the adaptive and non-adaptive cases are required. This thesis concentrates on physics parameterizations of Atmospheric Global Climate Models (AGCMs), presenting the current hierarchy of idealized physics parameterizations found in the literature. It focuses on and provides a comprehensive explanation of a simplified dry physics model for AGCMs, exploring where it is situated in the current hierarchy and its steady states in the uncoupled case. A coupling of the physics model to the adaptive dynamical core WAVETRISK is explained and explored. This includes characterizing the results in the non-adaptive case for time convergence, grid convergence, and the effects of the soil, while also benchmarking the climatology of the coupling. The simplified dry physics model introduces another level of complexity in the current dry physics hierarchy and is stable in the coupled and uncoupled cases. A decreasing temperature trend with height is observed, however warmer surface temperatures and cooler upper atmosphere temperatures, than that of Earth, are produced in the steady states. Additionally a linear rate of convergence in space is noted and an improvement in parallel efficiency with resolution is required. Overall these results can be used as a benchmark for future coupling in the adaptive case.

Acknowledgements

I wish to express my deepest gratitude to my supervisor Dr. Nicholas Kevlahan. Thank you for being my mentor, introducing me to a new field and for recognizing my potential. Through his continuous support and guidance, he empowered me to pursue excellence and conduct a Masters thesis that I never envisioned accomplishing.

I would like to extend my gratitude, Dr. Altaf Arain and Dr. James Cotton, for their valuable time as my examination committee.

Finally, I would like to express my gratitude to my friends and family, particularly my parents, for their unwavering love and support during my academic journey.

Contents

List of Figures

List of Tables

Abbreviations

2D two-dimensional

3D three-dimensional

AGCM Atmospheric Global Climate Model

AOGCM Atmospheric Ocean Global Climate Model

DCMIP Dynamical Core Intercomparison Project

ESM Earth System Models

GCM Global Climate Model

GFDL Geophysical Fluid Dynamic Laboratory

IPCC Intergovernmental Panel on Climate Change

ISA International Standard Atmosphere

KE kinetic energy

PBL Planetary Boundary Layer

Chapter 1

Introduction

Global Climate Models (GCMs) are numerical simulations that predict the general circulation of a planet. These models are represented by systems of mathematical equations that utilize numerical methods to simulate different planetary components on a three-dimensional (3D) grid. These components are coupled together and the model is run for a desired time period, producing a climate prediction. GCMs are widely known for simulating the climate of Earth, but are also created and used for other planets, including Earth-like rocky planets like Mars and Venus, gas planets like Jupiter and Saturn and exoplanets. In many cases, especially when modeling Earth, GCMs are used to predict climate for seasonal, decadal and centurial time scales. Furthermore, these models can also be used to simulate past climates ("paleoclimatology"). Intercomparison projects and techniques like hind-casting are used to compare models and test their accuracy. In general, many models, especially simplified models, are used to gain more knowledge on complex and unknown components of climate.

Climate models have been used and developed continuously since the 1970s. Over the years a multitude of climate models have been created by a diverse range of groups. The Intergovernmental Panel on Climate Change (IPCC) has published regular assessments since the 1990s on different evolutionary aspects of climate models. These models have undergone various transformations and improvements. For example, the types of model processes included in GCMs has progressed from the inclusion of precipitation, radiation, and CO_2 effects in the 1970s, to more recently the inclusion of models for land surface (e.g. vegetation), clouds, chemistry and aerosols (Le Treut et al. 2007). Furthermore, the horizontal and vertical grid resolution of Atmospheric Global Climate Models (AGCMs) has increased from $\sim$ 500 km (about 5°) and $\sim$ 10–15 vertical layers respectively in the 1990s (Le Treut et al. 2007), to a minimum $\sim$ 10–50 km (about 1/10°) and $\sim$ 80–90 vertical levels respectively in current operational models (Chen et al. 2021).

While the climate community is tirelessly striving to improve climate models, there are still many bottlenecks and challenges that remain to be conquered. The question of model accuracy in light of tuning of subgrid models is one such challenge. Many components of models are tested individually, making choices for certain parameters, before coupling it all together into a GCM. When components are assembled to build the GCM, these parameters are tuned to ensure observational and numerical constraints

are met. However, this tuning raises the question of the reliability of models (Flato et al. 2013).

Furthermore, our lack of scientific understanding of certain climate components and interactions is a challenge that many researchers are exploring. Through the use of well-understood simplified models researchers are working towards developing a deeper understanding of many aspects of climate.

Lastly, a major bottleneck of climate models is the enormous computational power and associated computational time required to produce useful results. Any increase in complexity, though the inclusion of more processes and higher resolution, requires more computational power. With only limited computational power, modelers are required to make numerous trade-offs between CPU time, physical and numerical accuracy, and the number of physical processes represented. A fundamental constraint is the maximum horizontal and vertical grid resolutions. In many cases, modelers choose a relatively coarse horizontal resolution (e.g. $\sim$ 100 km). However, this lack of resolution requires more processes to be modelled because they occur on a smaller scale and cannot be resolved by the grid. These approximations are called the subgrid scale (SGS) physics parameterizations of the model and are a challenging and less well understood part of climate models. It is these parameterizations that require the tuning. While these modelled physical processes are essential, they are also a major limitation in the accuracy of the climate models.

With these challenges in mind, this thesis focuses on simplified models and the physics parameterizations of AGCMs. More specifically, it will present and explore a simplified dry physics model for AGCMs. Subsequent sections of this chapter will elaborate on certain subjects to provide a basic understanding of concepts pertaining to climate modeling and to further emphasize the challenges mentioned above. Subjects explored include parameterization and resolution of physical processes, the components of GCMs (characterizing the physics and the dynamics of models), common simplifications of GCMs and grid adaptivity. Lastly, an in-depth overview of the objectives and contributions of this paper will be provided.

1.1 Parameterizing versus resolving

To simulate the climate of a planet, the atmosphere or ocean is partitioned into a 3D grid of cells (generally divided into horizontal grids and vertical layers, making a shallow atmosphere approximation). Within each cell, only one value is predicted for the climate variables that are solved for by the model. This act of creating discrete regions and simplifying the complexity of the planet and atmosphere is called discretization. When discretizing a planet's atmosphere or oceans the length between each spatial grid point, also known as the spatial scale, can vary. The scale chosen for the model is referred to as the "resolved scale". There is also a temporal discretization ("time step"), usually proportional to the horizontal grid size (to ensure numerical stability).

Different processes occur at different spatial and temporal scales. For example, in Figure 1.1, for Earth, turbulence occurs at a very small spatial and temporal scale (down to millimetre scales) compared to extratropical cyclones, which occur at a larger time and space scale.

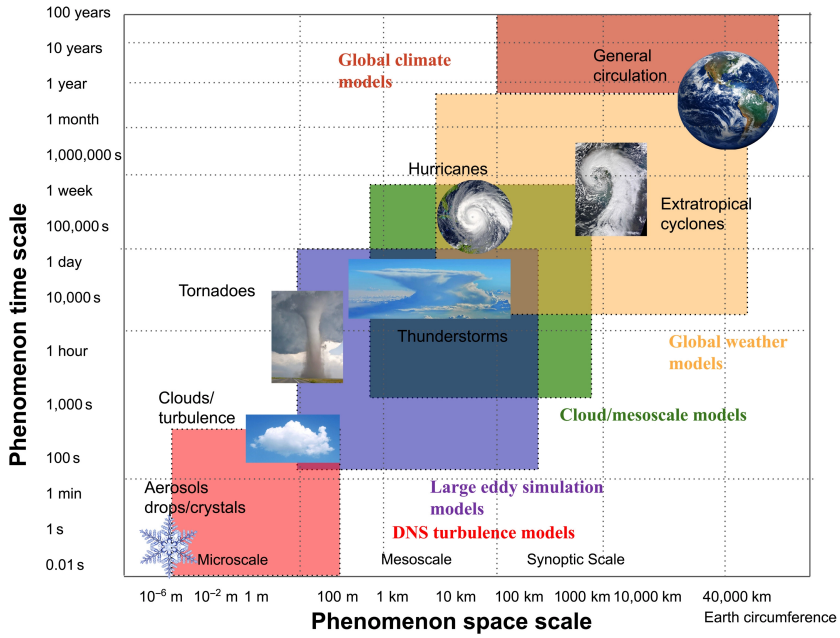

FIGURE 1.1: Temporal and spatial scale diagram, created by Gettelman et al. (2022), illustrating the time and space scales of different processes of climate. Limitations in computational power affects the scales chosen for the model, which in many cases are larger than the scales of some physical processes, like small scale turbulence. These processes are deemed "small scale" or "subgrid scale" processes and must be parameterized. It can also be seen the different scales of models in the colored boxes with the labels matching in color. The GCMs occur at a larger scale compared to that of large eddy simulation models. Therefore, the overall scale chosen depends on the processes being modeled, as some processes, like the general circulation of a planet, occurs at larger scales.

Depending on the chosen grid scale, only certain quantities and processes are resolved and explicitly solved for by the climate model. Some examples of quantities that are resolved include temperature and velocity/momentum. While it would be desirable to be able to use a scale which resolves all processes, this is not possible. Modelers only have a certain amount of computational power and need to find a balance between the total computational time of the model, the resolution of the grid and the complexity and number of processes included. Therefore, the chosen resolved scale usually cannot accommodate all processes. For example, the resolution of current operational climate models' are O(100–200) km, even though numerical weather prediction (NWP) models use scales as small as $\sim$ 10 km.

Processes included in the model which occur on a smaller length scale than the resolved length scale are deemed "subgrid scale scale processes". For example, atmospheric turbulence and cloud micro-physics occur on a smaller grid scale than a typical GCM resolved scale. These small scale processes cannot be solved for on the larger scales and their effects on the resolved scales must therefore be approximated and parameterized.

Parameterization is the procedure of representing an unresolved physical process's effects on the larger resolved scale through the use of resolved variables. These sub-grid parameterizations are a simplification of the process it is representing. Processes may also be parameterized when they are too complex or there is a lack of knowledge of the phenomenon. In some cases, to simplify the model, processes are deliberately under-resolved and approximated. This occurs when only certain quantities are solved for and not every aspect is included or resolved. For example, the process of convection and (small-scale) turbulence can be modeled as an under-resolved process, thus keeping a certain aspect of simplicity while gaining some accuracy.

Sadly, while parameterizations are required due to the computational power bottleneck, they are a limitation of many climate models. Parameterizations may not fully capture certain effects of processes or entire phenomena due to their simplicity or our lack of understanding of the process. Furthermore, the integration and coupling of parameterizations into a model is another limitation and can lead to inaccurate results. Since these parameterizations are approximations, they include parameters that maybe accurate for only certain assumptions, limiting their use. There may also be inconsistencies between assumptions made by the dynamical core and in the subgrid scale physical model. Therefore parameterizations are a field of climate modeling that modelers are actively researching and attempting to improve in order to further enhance current GCMs.

1.1.1 Horizontal and vertical grid resolution

Typically, in many GCMs, horizontal spatial grid scales are $O(100)$ km (Mcfarlane 2011). In contrast, in most GCMs, the total vertical height into the atmosphere is smaller than the horizontal spatial scale. This results in a much smaller vertical grid scale ($\sim$ 10km or less) compared to the horizontal scale. Therefore, the term "resolved scale" typically refers to the horizontal spatial grid scale, not the vertical scale.

1.1.2 Prognostic and diagnostic variables

Within GCMs, resolved processes solve for a specific "prognostic" variable in the model. The equations that govern the prognostic variables incorporate time and space derivatives of the variables and must be integrated in order to be resolved. These variables are being solved for over the grid space and time, usually using numerical integration techniques, and are deemed prognostic variables. In most GCMs temperature, velocity and density are prognostic variables. Variables that are not prognostic are known as "diagnostic variables" and usually depend on the the prognostic variables in their governing equations.

1.2 Global climate model components

GCMs consist of multiple inter-coupled models, each containing their own systems of equations evaluated on a grid to simulate desired effects. When breaking down a GCM, there are three major components, the atmosphere, the ocean (including sea ice) and land. Each component uses a different grid and has its own set of sub-processes. In an ideal case, the desired spatial and temporal scales would be represented by a single discretization for the entire system of equations. This allows all processes and quantities to be resolved, for all components. Sadly, as explained above, this is a challenge as it would require an extreme amount of computational power. Therefore, with this in mind, within both the ocean and atmosphere components, processes can be categorized into two major sub groups: the "dynamical core" and the "physics", while the land component only contains physics processes.

1.2.1 The dynamical core

The dynamical core, sometimes also referred to as the "dynamics", includes key fluid dynamic and thermodynamic processes that occur and can be solved on the chosen resolved scales. These processes' representing equations are known as the governing equations, and include equations for conservation laws (of mass, momentum and energy), as well as equation relating thermodynamic variables (known as the equation of state). Depending on the conditions, and if the dynamical core is running for the ocean or atmosphere, other conservation equations, for tracers, might also be included. For example, an equation for the conservation of water and salinity or for aerosols.

The level of complexity of the governing equations in a dynamical core depends on the assumptions and conditions used, which can lead to either simplification or increased complexity. A hierarchy of governing equations can be established for geophysical fluid dynamics, based on the different complexities and variants of these approximated equations. Figure 1.2 displays a compact hierarchy of the governing equations with the 3D Navier–Stokes equations at the complex end. As one moves down the hierarchy, an increasing number of simplifications and assumptions are made. While the nonlinear Navier–Stokes equations are well understood and studied within the field of fluid dynamics, they are complex and not computationally feasible to be used in GCMs. More realistic nonhydrostatic models have gained popularity recently and are used within some dynamical cores, so much so that a dynamical core inter-comparison project was run on participating nonhydrostatic dynamical cores (e.g. Ullrich et al. (2017)). However the primitive equations, which assumes hydrostatic balance, are highly relevant and still dominant in GCMs, especially when simplified models are sufficient. It is important to note that different formulations of the equations can be utilized for each approximation in the hierarchy. For example, in the hydrostatic primitive equations, viscous effects might not be included, thus producing a different formulation but retaining the the basic hydrostatic approximation.

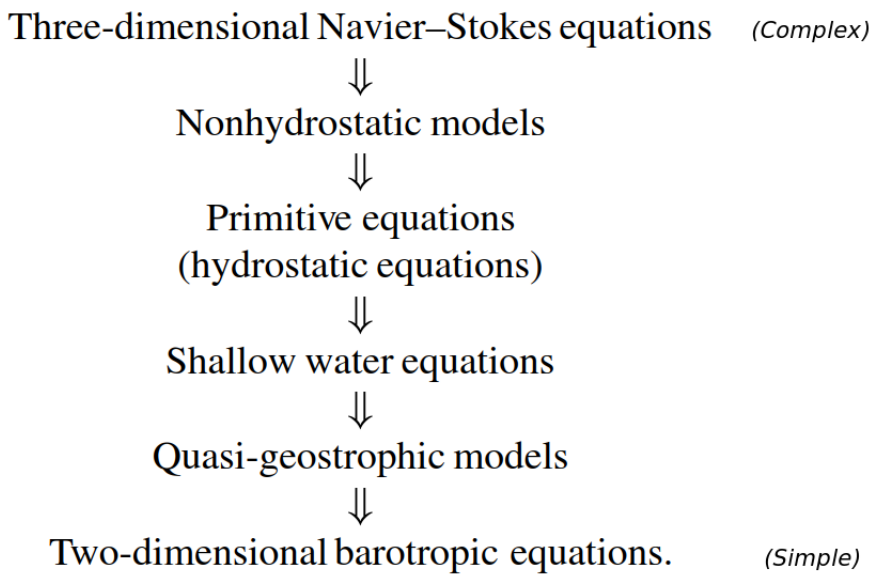

FIGURE 1.2: A Hierarchy of the governing equations of motion of fluids presented by Temam and Ziane (2005). Starting at the complex end of the hierarchy with the 3D Navier–Stokes equations, approximations and simplifications are made in order to move down and obtain the simpler approximate equations. A highly relevant set of equations that are commonly used in GCMs are the primitive equations, which assume hydrostatic balance in the vertical.

The Navier–Stokes for the atmosphere are (Temam and Miranville 2005):

$$\frac{D\boldsymbol{V}}{Dt} = -\frac{1}{\rho}\nabla_3 p + G - \omega \times \boldsymbol{V} + D \qquad (\textit{Conservation of Momentum})$$

$$\frac{D\rho}{Dt} + \rho\nabla \cdot \boldsymbol{V} = 0 \qquad (\textit{Conservation of mass})$$

$$c_p\frac{DT}{Dt} - \frac{RT}{\rho}\frac{Dp}{Dt} = \frac{DQ}{DT} \qquad (\textit{Conservation of energy})$$

$$p = R\rho T \qquad (\textit{The Equation of State})$$

where:

- $\boldsymbol{V} = (u, v, w)$ and is velocity
- ρ = density, p = pressure, T = temperature
- $G = (0, 0, -g)$ is gravity
- c_p = specific heat, R = specific gas constant
- ω = angular velocity
- D is viscosity terms (dissipative terms)
- $\frac{DQ}{Dt}$ is heat flux by unit volume

- $\frac{D}{Dt} = \frac{\partial}{\partial t} + \boldsymbol{V} \cdot \nabla$ represents the material derivative.

To derive the primitive equations, the hydrostatic approximation is applied to the above equation. This approximation assumes that the horizontal grid scale is much larger than the vertical grid scale. Therefore, the small scale terms in the vertical momentum equation are negligible. The dominant vertical terms are gravity and the vertical pressure gradient term. This means we assume that that the air in the vertical direction is static and does not accelerate. This simplification of the conservation of momentum equation in the vertical direction is called the hydrostatic approximation,

$$\frac{\partial p}{\partial z} = -\rho g. \tag{1.1}$$

Since the governing equations must be solved for the prognostic variables at each grid point, these continuous partial differential equations need to be suitably discretized by the dynamical core using techniques from numerical analysis. A fundamental characteristic of the dynamical core is that the discretization is based on a relatively small number of thin two-dimensional (2D) quasi-horizontal layers. This layered structure is appropriate for the large aspect ratio between the horizontal scale, in which the large scale dynamics of the oceans and atmosphere occur on, and the small vertical scales. Therefore, the dynamics are approximated on the horizontal grid, assuming vertical homogeneity between each layer. Moreover, as the dynamics' equations incorporate horizontal fluxes, the requirement for numerical interpolation arises. Scalar values, for example tracers, are evaluated at the center of the each grid cell. On the other hand the fluxes, which represent the amount of a specific variable flowing through from one cell to the other, are evaluated at the interfaces of the cell. However when utilizing a numerical integration scheme, the values of both fluxes and scalars are required for each grid cell, but the values supplied are at different points on the grid. Therefore, numerical interpolation is used to average the value of a scalar at the interfaces and thus the values of the scalar in horizontal neighbouring grid cells are required.

The dynamical core also has boundary and initial conditions and constraints applied to the equations. While the dynamical core can be run on its own, most models couple it with physical processes to gain a more realistic representation of the model being simulated.

1.2.2 Physical processes

The physical processes of a climate model, sometimes also referred to as the physics, contains all unresolved or under-resolved dynamical processes and non-dynamic processes. Therefore, the physics includes parameterizations of small-scale processes and under-resolved processes. Some of the major dynamic processes that are included in the physics are turbulence and some types of convection, while non-dynamic processes includes solar radiation.

Within the atmosphere the major physical processes that are modelled include radiation, convection, a turbulent boundary layer scheme, condensation, clouds and turbulence. The ocean has its own set of physical processes that are modeled. Some of the prominent ocean physics include boundary layer mixing at both the ocean floor and surface, bottom friction, internal ocean mixing, convection, vertical turbulent diffusion of heat and momentum, surface heat flux, horizontal turbulence and topographic effects. Lastly while the category of land does not contain a dynamical core, it does have a group of processes that are represented, for example soil and vegetation. In general, even though the physics are only approximations of the underlying processes, they allow models to be simplified when desired and includes effects that in some cases cannot otherwise be modeled.

While both the dynamics and physics represent significant components of a planet's climate, there is another major distinction among the two, other than the resolution of the variables for the models. As mentioned above, the dynamics are evaluated in 2D layers of the grid. However, due to the difference in scales of the horizontal and vertical, many of the physics processes can be considered horizontally uncoupled in each time step. Therefore, the physics trends are evaluated as part of each time step in 1D columns (i.e. the dynamical prognostic variables are computed in horizontal layers and their values are modified by physical processes computed as a set of vertical columns). Due to this difference in evaluation based on both the resolution and the orientation, the dynamics and the physics must be included as separate steps within a given time steps.

1.2.3 Physics-dynamics coupling

In early models the physics and dynamics were solved at the same time. This method of solving all processes at once is called the concurrent method (Dubal et al. 2004). However, over time the complexity of models and resolution increased and our understanding of the unresolved physical processes improved. Therefore, the separation of the physics from the dynamics was explored. The separation of the physics from the dynamics allowed researchers to develop models in a more modular and easy way (Gross et al. 2018), but also meant that their impacts and results must be coupled together. This idea of coupling the physics and the dynamics also comes with the challenge of determining how each process is evaluated and estimating and controlling the resulting errors.

Splitting is a procedure that is used to couple the physics and dynamics, where each process and its impact are evaluated at the model state in isolation of one another (Gross et al. 2018). There are two main types of splitting that are utilized by GCMs called "Process Splitting" and "Time Splitting".

In process splitting all physics and dynamics processes step forward in time in parallel, using the results from the previous model state as input and evaluates for the time tendencies of the prognostic variables independently (Gross et al. 2016). At the end of the time step the model state is updated with each tendency and then another time step

is taken, starting with the new model state. This method is also known as the parallel split method, as architecturally each process can be evaluated in parallel and independent of one another, but also each process does not see the impact of another process based on the previous state. This method constrains the size of the time step, as it has to be short in order to acceptably ignore the actual effects of process interactions (Gross et al. 2016).

Time splitting orders all processes is a specific sequence and evaluates each sequentially (Gross et al. 2016). The first split step evaluates the time tendencies for a given process (e.g. the dynamics) using the previous model state as input. After the initial step, the model state is updated and serves as input for the subsequent processes (e.g. the physics models). This sequential sequence continues for all processes until the last scheme is assessed, completing the time step. This method is also known as the sequential split method due to the sequential evaluation of processes and updating of the model state. While there are fewer restrictions on the time step of this method, the processes cannot be evaluated in parallel and the order chosen restricts the method (Gross et al. 2016). Different orders chosen for time splitting can produce different outcomes. Processes often compete for the same resources and they also can be sources or sinks of certain resources (Gross et al. 2018). Therefore, their order can drastically alter the output. Time splitting methods are limited to second order in time, $O(\Delta t^2)$.

The previous two methods are core coupling methods, but there is a third method which is a hybrid method of the two core splitting methods. The hybrid approach has some processes run using parallel splitting, while others run sequentially. The processes that run in parallel usually have shorter time steps, while those that run sequentially have time steps that are comparable to the time step of the GCM (Gross et al. 2016). The hybrid approach is the best of both core coupling methods, but is more complex in terms of the software architecture (Gross et al. 2016).

While each splitting process has pros and cons, the chosen method is dependent on different aspects of the model. For example, numerical stability. The implicit or explicit nature of the time step can affect the method chosen (Gross et al. 2016). Generally, the interaction of physics and dynamics produces inaccuracies in climate models. A lack of understanding of feedbacks and other effects, and an inaccurate representation of these effects due to the trade-offs of the coupling are a two reasons physics-dynamics coupling remains an active field of research. Researchers are working towards understanding and improving this coupling to provide accurate and realistic climate simulations.

1.3 Simplified and comprehensive climate models

GCMs are categorized as either comprehensive or simplified. Comprehensive models are very complex and contain sophisticated sub-models of the atmosphere, ocean and land to obtain a realistic simulation or prediction of the climate. These models are used, for example, by the United Nations IPCC to set standards for the evaluation of climate change and provide up-to-date information on global warming for policy makers within many

countries. There are multiple comprehensive models, especially for earth called Earth System Models (ESM), for example ESM4 by the Geophysical Fluid Dynamic Laboratory (GFDL) and CanESM5 by the Canadian Centre for Climate Modelling and Analysis. Since many of the models are created by different groups and organizations, these comprehensive models can vary and thus Coupled Modeled Intercomparison Projects are run, incorporating coupled models and ESMs in order to compare and review models.

Figure 1.3a shows a basic interpretation of the constituents of a comprehensive GCM. It displays the basic structure of a model, including its major components (atmosphere, ocean and land surface) and some of their processes. The coupling of processes is also displayed, and while the idea of coupling physics and dynamics has already been explained, the same concept is used to couple each major group and bring together the model as one. An overarching display of the interactions and exchanges between groups can also be found in figure 1.3b and adds a layer of complexity to their coupling.

While this diagram is a basic interpretation, it nevertheless shows how intricate a GCM can be, and also how convoluted a model can get! There are still many aspects of the general circulation of a planet that we do not fully understand. While researches are looking to explore these physical phenomena, they are also attempting to gain further understanding of the numerical model parameterizations, coupling and interactions among all process in order to realistically model a planet. Therefore, simplifications and simplified models are a useful aid to improving our understanding of climate.

The simplification of GCMs can vary depending on the desired effects. Models can be simplified based on the type of climate component treated in the model. For example, AGCMs simulate the general circulation of the atmosphere, while Atmospheric Ocean Global Climate Model (AOGCM) couples the ocean and atmosphere sub models to simulate the general circulation. Further simplification can occur through simpler dynamical cores and physical processes of the sub models, as well as different combinations of physical processes that are coupled. These simplified models are sometimes referred to as "idealized models", and are used to improve our understanding of climate components. The climate community is working actively on creating a hierarchy of models, including a full range of both idealized and comprehensive models, that will form the basis of our understanding of climate. A branch of the hierarchy focuses on AGCMs which contains a sub-branch focusing on the physics models of AGCMs.

Physics models are important, as they can be used in combination with a dynamical core to research climate processes and interactions, but also in model intercomparison projects of dynamical cores. Furthermore, these models can be used to study the challenges of coupling and parameterization in general. This thesis focuses on relatively simple AGCMs, and while the dynamical core is an integral part of the model, the composition and simplification of the physical processes used is the main focus of this thesis.

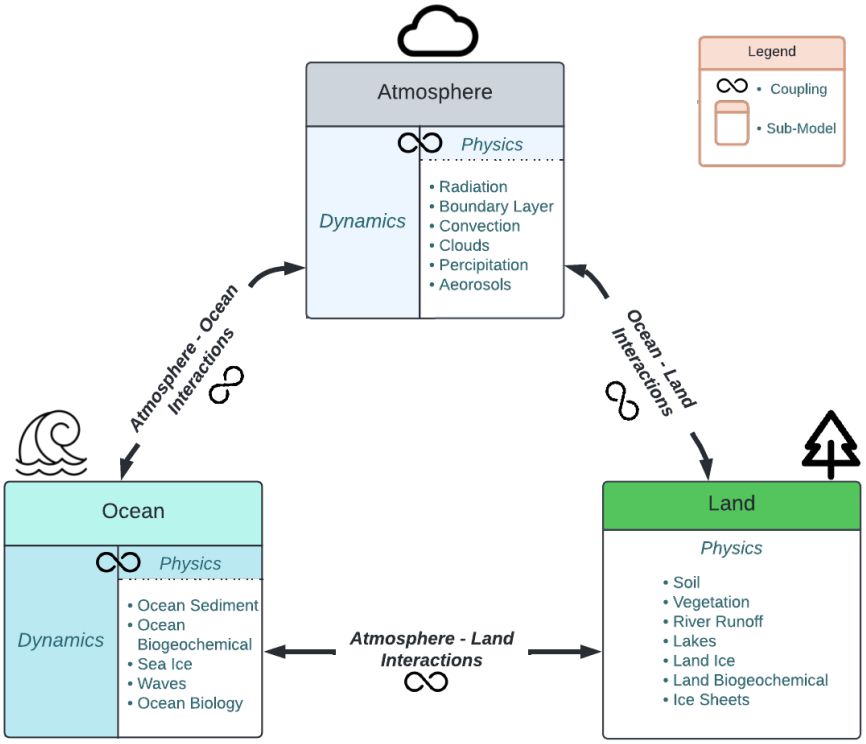

(a) GCM comprehensive diagram with the basics of interactions, couplings and sub-models. The sub-models displayed are Atmosphere, Ocean and Land. Each sub-model includes major physical processes that might be considered in a comprehensive model, as well as if the sub-model contains a dynamical core.

Atmosphere – Ocean Interactions	Exchange in: • Energy (Heat) • Moisture • Momentum • Mass (e.g. Freshwater on Earth) • Gases & Chemicals Biogeochemical Interactions
Atmosphere – Land Interactions	Exchange in: • Moisture • Energy • Gases & Aerosols Affects of Forcers & Feedbacks
Ocean – Land Interactions	Exchange in: • Freshwater • Nutrients • Carbon • Particles

(b) The basic interactions between the atmosphere, ocean and land models. The interactions include exchanges of constituents between the sub-models.

Figure 1.3: Comprehensive GCM diagram and interactions.

1.4 Atmospheric physics

AGCMs play a major role within the climate hierarchy and can be used to model planets besides Earth. The physical processes represented in an AGCM can differ depending on the modeling goals and class of model used (simple or complex). For example, whether moisture is incorporated in the idealized model can determine the type of processes coupled and the fidelity with which certain effects are represented. The major physical processes that are usually included in AGCMs are: radiation, convection, the turbulent planetary boundary layer, vertical and horizontal turbulent diffusion, condensation and clouds.

The radiation model attempts to capture the radiative effects of incident solar radiation, the atmosphere and the planet itself (e.g. infrared radiation from the ground). Solar radiation determines the equilibrium energy balance, as a planet can gain or lose energy through radiation absorption and emission from the upper atmosphere. This radiation model is the most important component determining the planet's equilibrium mean temperature. A simple example of a well known radiation parameterization is Newtonian cooling, which relaxes the temperature to a pre-determined equilibrium temperature.

Convection is an important processes that can either be parameterized or resolved (models often include both resolved and parameterized convection). In many AGCMs convection must be parameterized due to lack of resolution, or due to the hydrostatic assumption (which does not allow overturning). Convection transports moisture, heat and momentum, and is dependent upon the assumptions made (e.g. the inclusion of moisture).

Planetary Boundary Layer (PBL) schemes model the lower part (the troposphere) and represents the effects of the interaction with the surface of the planet. Surface friction has a significant influence upon the layer, for example the influence on winds, and its effect reduces away from the surface. Another aspect of climate modeled by the PBL is turbulence, which naturally occurs due to velocity shear at high Reynolds numbers.

Turbulence has a big impact on the atmosphere, as it transports and mixes tracers, heat and momentum. While large scale turbulence can be resolved by the model, not all turbulence occurs at the resolved grid scale of the model. This small scale turbulence and its effects are important to the general circulation of the planet and must be parameterized (usually as a so-called "eddy viscosity").

Condensation and its numerical representation has multiple effects. It can produce precipitation and releases heat, thus it should be taken into account when moisture is incorporated in a model.

Clouds can both cool and warm the Earth, and there are many different types of clouds. A sub-component of cloud models is cloud microphysics, which refers to processes that occur at the microscopic scale and affect both the generation and development of clouds. Clouds are not well represented by idealized physics, but due to their extremely

important impact determining climate, scientists have emphasized the need to further research and improve its parameterizations (Maher et al. 2019; Jeevanjee et al. 2017).

The physical processes mentioned above are some of the major processes that can be found in AGCMs. However, depending on the complexity of the model, some processes may be neglected and other processes maybe included. For example, a basic simplification is neglecting the effects of moisture, as is done in so-called "dry models".

1.5 Dry and moist physics

Excluding moisture and its effects from physics models is an assumption that some simple models make. Therefore, physics models for AGCMs can be classified into dry and moist models. The incorporation of moisture means that condensible substances and their effects on the atmosphere of a planet are taken into consideration. Condensible substances are those which can change phases within the atmosphere. The only significant condensible substance on Earth is water, but can be different substances on other planets. For example, on Earth water exists in all three phases, while on Mars and Titan CO_2 and methane are the condensible substances, respectively. The addition of moisture to the atmosphere adds another layer of complexity to the physics. The phase changes have a major affect on the thermodynamics and the energy budget since, for a substance to change phases, energy must be absorbed or released, represented by latent heat. Latent heat is the amount of energy required for a substance to transition phases while temperature is held constant. Within moist physics models a latent heat flux and the effects of the transitioning of phases are usually considered depending on the desired complexity. Most physics schemes typically include convection, condensation, precipitation and cloud formation. Even though moist processes, for example clouds, are in need of further research, a full understanding of physics parameterizations in the dry case is the first step to building a realistic and reliable climate model.

1.6 Grid adaptivity

As mentioned earlier, due to the computational bottleneck, a lack of resolution requires processes to be parameterized instead of resolved. To mitigate these challenges, climate researchers have explored adaptive resolution. Adaptive resolution allows models to use finer horizontal grids at different locations and times. The two types of adaptivity are static adaptivity and dynamic adaptive refinement. Static adaptivity is a type of mesh refinement in which only predetermined regions are locally refined. A type of static refinement is nested adaptivity. Nested adaptivity occurs in local regions in which a finer grid is nested within the coarser grid. The finer grids get their boundary conditions from the coarser grids. Nested grids allow higher resolution over regional forecast areas, such as North America. Dynamic adaptivity locally refines and coarsens the grid as a function of time and location based on dynamical, physical or numerical accuracy criteria (Jablonowski et al. 2004). Beyond capturing the evolution of the small scale physics, dynamic adaptivity aids in capturing the effects of the interactions between

small-scale and large scale processes and makes better use of the available computational resources (Jablonowski et al. 2004).

In theory, adaptive grids could improve the realism and accuracy of model simulations, but there are known complications and challenges that come with adaptivity. Most notable, the physics parameterization of models are often optimized for particular grid ranges, and may not be suitable when a mesh is refined (Collins et al. 2013). Therefore, understanding the scale dependence of each physics process is essential. The question of whether physics processes should be "scale-aware" is one challenge that many researchers are exploring (e.g. Frassoni et al. 2018; Park et al. 2022). Scale-aware physics parameterizations adjust themselves based on the current local resolution of the grid. In the case where the resolution is refined enough to allow for the process to be fully resolved, the parameterization is deactivated. Specifically, in the case of dynamic adaptivity, a refinement criteria needs to be met before local refinement (or coarsening) can occur. A central challenge of adaptivity is whether these criteria should be based on both the physics and the dynamics, or the dynamics alone. In many cases the criteria is flow-based, for example based on gradients or vorticity (e.g., St-Cyr et al. 2008) or based on the numerical approximation (e.g., Skamarock et al. 1989) (Ferguson et al. 2016). In order to make progress addressing the questions that come with these challenges researchers need physics models that can work in both the adaptive and non-adaptive case.

1.7 Thesis structure

This thesis researches and explores simple atmospheric physics models, more specifically dry physics models. Motivated by the challenges of computational power, physics parameterization limitations and adaptivity, the goals of this thesis are to first explore the current physics models in AGCMs and then present and investigate the climatology of a particular simple dry physics model. In general, the goal for the dry physics model is to provide a simple physics model that can be coupled with different dynamical cores, in both the adaptive and non-adaptive cases, and can be used to model different planets, in hopes of researching, resolving and understanding the challenges of atmospheric physics. Therefore, a further objective of this thesis is to investigate this package first in the non-adaptive case by coupling it with an existing dynamical core, and characterizing its climatology at various grid resolutions. With these initial tests and the understanding of the physics model in the non-adaptive case, it will allow us to investigate the package in the adaptive case in the future and will allow for further investigation into the scale-dependence of certain physics processes.

Section 2 presents an overview of current idealized dry and moist physics models. First, an explanation of the different climate processes and their variations within dry and moist physics is introduced. Additionally, the advancements of dry and moist physics models over recent years is summarized, along with their current hierarchies. Finally, in this section the current gaps found within both dry and moist climate hierarchies are highlighted.

Section 3 introduces the dry atmospheric physics model we focus on and explains its special position in the climate model hierarchy. Its assumptions, numerical properties and sub-processes, including the complexity of each sub-process chosen, are described.

Section 4 documents the results for the uncoupled model's equilibrium states (i.e. when run without any horizontal dynamics), including a summary of the initial conditions used for the simulations.

Section 5 explains how the simple dry physics model is coupled to a general dynamical core. More specifically, we explain how to couple the dynamically adaptive dynamical core WAVETRISK (Kevlahan and Dubos 2019) to the physics package, detailing all modifications made to the software. Lastly an initial overview of the sensitivities of the physics package will be included.

Section 6 presents and discusses results of implementing the dry simple physics model with Wavetrisk (i.e. its equilibrium statistical states). As a first step we explore simulations in the non-adaptive case, benchmarking and characterizing the results of the coupling, as well as exploring the differences with and without the soil model. Furthermore, results for time convergence, grid convergence and performance of the physics, for four different grid sizes, are presented.

Section 7 documents the climatology of the physics package coupling with WAVETRISK. The climatology is presented for key prognostic and diagnostic variables and compared to the simple Held–Suarez model and the temperature profile for the standard atmosphere.

Section 8 discusses and summarizes the work presented in this thesis, as well proposing possible next steps.

The principal contributions of this thesis include the synthesis of specific concepts required for understanding the overarching ideas behind climate, a review of a simple dry physics package, with assumptions clearly stated and a concise explanation of the current atmospheric physics found in literature and its hierarchy. This explanation is important, as it provides readers with a concrete understanding of the state-of-the-art of atmospheric physics parameterizations. Further contributions include an extension to WAVETRISK dynamical core to permit coupling with the simple dry physics package and the extension of the physics package to allow for single column evaluations and future coupling with adaptive dynamical cores. The final contributions include a review and evaluation of the importance of the soil column model (not present in most models), coupling the simple dry physics package with a dynamical core in the non-adaptive case and benchmarking the results.

Chapter 2

Literature Review

Throughout the years as computational power increased and our understanding of climate phenomena grew, in particular our understanding of individual atmospheric subprocesses, we saw an increase in the complexity of Global Climate Models (GCMs). A drawback of this increase is our lack of knowledge of the intricacies of these models and how their different components interact. In many situations we understand how each individual component works, but we lack the understanding of effects and feedbacks produced through different component couplings. To improve upon our knowledge and understanding, many researches are turning to simplified climate models to research different climate interactions and dynamics. These simple models, also known as idealized models, have allowed scientists to broaden their understanding of climate interactions and to further develop realistic models of climate processes and GCMs themselves. Idealized climate models is a topic that has gained immense popularity in the climate community in the past two decades. In 2005, Issac Held emphasized the need for idealized climate model research and the creation of a climate model hierarchy as the foundation of our understanding of the general circulation of planets (Held 2005). Even with the creation of complex GCMs, scientists turn to the well understood idealized models to isolate and explore climate processes and interactions. Over the years the climate hierarchy has evolved as the range of idealized models has broadened.

Within the Atmospheric Global Climate Model (AGCM) branch of the climate hierarchy, physical processes and their coupling includes two major components: moist and dry physics. While moist physics includes the effect of moisture (i.e. water in all its phases), much research has utilized the next level of complexity beyond moist physics: the "aquaplanet" model. Aquaplanet models are idealized atmospheric climate models that include a slab of ocean serving as the planet's surface. These simulations can be used to compare different atmospheric climate conditions and in many cases have different couplings of physical processes. Overall, the climate community has progressed in the physics branch of the hierarchy, but continues to explore ways to close the remaining gaps.

The following sections review the different physics sub-models and their various numerical schemes, in both moist and dry physics configurations. This will include schemes

for radiation, convection, turbulence, the planetary boundary layer, and land. Furthermore, the sections explore the different compositions of physics models used and will evaluate how they have changed over the years with the inclusions of different variations of the sub-model schemes. Lastly, the current gaps in both moist and dry idealized physics packages are explored.

2.1 Dry physics models

Dry physics models resolve a multitude of different coupled physical phenomena and also include additional physical effects through parameterizations and under-resolved sub-models. Specific sub-models include radiation, a planetary boundary layer scheme, vertical diffusion, convection and, most recently, chemistry and aerosols. Many of the schemes use parameterizations of the underlying process to keep the models and coupling simple to simulate and focus on specific effects. For example, a study presented by Komacek and Showman (2016) explored the relationship between the day-side and night-side temperature differences of Hot Jupiters using an AGCM with simplified physics of a radiation and planetary boundary layer scheme. Over the years different variations of sub-models have been used in dry physics models of AGCMs, and the following subsections will explore the evolution of each individual process and the hierarchies of models in the dry case.

2.1.1 Radiation schemes

Radiation is included in most dry models. Radiation has major effects on the prognostic variables and the climate in general. The simplest radiation scheme, called Newtonian cooling, was included in the Held–Suarez test case in 1994 (Held and Suarez 1994). This scheme is a simple parameterization that relaxes the temperature field to a prescribed temperature equilibrium depending on time, latitude and height (Held and Suarez 1994). Due to its simplicity, it is still relevant today, for example Mbengue and Woollings (2019) implemented it in their physics model for the Earth, with a modification to the equilibrium temperature. The Held–Suarez scheme has also been utilized in non-Earth cases, as it is commonly used to compare dynamical cores and explore certain planetary dynamics. Polichtchouk et al. (2014) coupled such a scheme to a dynamical core to compare GCMs for hot extrasolar planets. In contrast, Lee et al. (2007) and Komacek and Showman (2016) incorporate the scheme to explore the supperotation of Venus and the dayside-nightside temperatures of Hot Jupiters respectively. While the simplicity of the scheme is its main attraction for many researchers, this is also a limitation as it is not a realistic representation of the effects of radiation.

Idealized dry physics models for non-Earth planets, have evolved to incorporate a more complex scheme called the two-stream approximation. Sometimes referred to as the single band two-stream approximation, it includes only infrared (i.e. longwave) radiation and solves the upward and downward fluxes of longwave radiation. This scheme has been extended to incorporate two wave bands by adding shortwave radiation and has been

used most recently by Innes and Pierrehumbert (2022) in their physics model simulating the climate for temperate sub-Neptunes. This dual band two-stream approximation is an intermediate complexity radiation scheme which is relatively simple. Dual band two-stream radiation models are still dominant in idealized physics models due to their simplicity (e.g. Schneider and Liu 2009; Heng et al. 2011; Lee et al. 2020). Simulations of Hot Jupiters (Showman et al. 2009; Amundsen, David S. et al. 2016) have incorporated a more complex radiation model that utilizes the two-stream formulations, but with additional frequency bands using the correlated-k method to treat opacities.

2.1.2 Boundary layer schemes

Even though radiation schemes have been utilized on their own to simulate and investigate the general circulation, in many cases they have been coupled with an atmospheric boundary layer model. The simplest model of the boundary layer is a drag scheme, modeling the important effects of surface friction on the atmosphere. The Held–Suarez test case models this enhanced drag as a Rayleigh friction. Rayleigh friction is a linear drag model which damps the low altitude winds (Held and Suarez 1994). Idealized dry earth cases (e.g. Schneider 2004; Mbengue and Woollings 2019) improved upon the linear drag parameterization with a damping of near surface winds using is a quadratic drag on the horizontal velocity. Differences among drag schemes beyond the degree is attributed to calculation of the drag coefficients. Simple non-Earth dry physics models have incorporated drag schemes and illustrate this concept. For example, Komacek and Showman (2016) and Tan and Komacek (2019) have included a boundary layer linear drag in horizontal momentum, whose drag coefficient is calculated differently, comprising of two components. These components are a spatially independent drag and a basal drag at the bottom of the domain. A drag model which simulates the effects of friction is a significant component in the boundary layer, especially when simulating a planet with a solid surface. However, more complex boundary layer models use a surface flux/drag scheme, with drag coefficient calculated using 'Monin–Obukhov' turbulent boundary layer drag laws, in conjunction with schemes to model small-scale turbulence (e.g. Heng et al. 2011; Mbengue and Woollings 2019).

Turbulence is an important aspect within climate as a turbulent flow greatly enhances mixing and diffusion of momentum, heat and scalars and this affects the general circulation. Turbulence parameterized as 1D vertical diffusion of momentum and energy can be represented within a fixed or dynamic vertical height. The dry Earth physics of Schneider and Walker (2006) and Mbengue and Woollings (2019) only includes a vertical turbulent diffusion scheme within the boundary layer at fixed heights of 2.5 m and 2500 m respectively. Non-Earth cases Heng et al. (2011) and Koll and Abbot (2015) utilize the scheme of an aquaplanet simulation (Frierson et al. 2006) to include a vertical diffusion scheme in the boundary layer. The scheme incorporates a dynamic boundary layer height dependent on a determined parameter: the critical Richardson number which determines the onset of vertical convective mixing in the layer (in a hydrostatic model that does not permit resolved vertical mixing). The Richardson number is a computed dimensionless

number used to determine whether turbulence exists. If the calculated Richardson number is below the critical Richardson number, then dynamic instability and turbulence occurs within the atmosphere. These vertical diffusion schemes are based on modelling enhanced turbulent diffusion coefficients and differ in the way the diffusion constants are computed.

Finally, surface fluxes have also been included in the boundary layer scheme for dry non-Earth cases through a constant in time heat flux (Schneider and Liu 2009) or internal flux acting as a time tendency (Innes and Pierrehumbert 2022) at the lowest boundary layer.

In summary, boundary layer schemes model complex small-scale climate dynamics that occur near the boundary of a planet and the major components currently integrated into these schemes are drag affects, surface fluxes and turbulence modelled as enhanced vertical diffusion.

While vertical diffusion has only been incorporated in the planetary boundary in simple dry cases and is used to parameterize the phenomenon of turbulence, the same cannot be said for horizontal diffusion parameterizations. Horizontal diffusion, in physics models, is a form of dissipation, modelled as a simple form of the turbulence diffusion model. A variant called horizontal hyperdiffusion is usually incorporated to ensure numerical stability occurs throughout the simulation, especially at the smallest scales. This scheme can be found incorporated in both earth and non-earth physics models including Schneider (2004) and Lee et al. (2007) respectively. While there may be different causes for the need of these schemes, generally many physics models utilize different variants of horizontal diffusion for stability reasons.

2.1.3 Dry convection schemes

The final physical effect included in a typical dry physics package is a convection scheme. While convection could in principle be fully resolved with the dynamics, the use of the hydrostatic approximation in most climate models, especially idealized cases, formally prohibits this. Therefore, convection, which is predominantly vertical motion and driven by buoyancy forces, must be parameterized. The parameterization might attempt to mimic the effects of moist convection, or only model the effects convection can have on a dry climate. A simple dry convective adjustment scheme is a parameterization which simulates the vertical transfer of heat. Hammond and Pierrehumbert (2017) incorporated this scheme in their research of the atmospheric dynamics of temperate sub-Neptunes. In contrast, the quasi-equilibrium convective scheme attempts to mimic moist convection and its impacts. Both Earth and non-Earth dry physics models have used the scheme, for example Mbengue and Woollings (2019) and Schneider and Liu (2009) respectively. Although the simplest physics models do not include a scheme for convection, more complex idealized physics models couple at least a dry convective adjustment scheme in attempt to simulate some convective processes in a hydrostatic model.

2.1.4 Recent sub-models in dry physics

Recently researchers have started exploring the incorporation of chemistry and aerosols in simple dry physics packages. The model presented by Hong and Reichler (2021) incorporated a simplified linear ozone scheme along with a modified Held–Suarez scheme and realistic bottom topography.

2.1.5 Hierarchy of dry physics models

Over the years simple dry physics models have become more complex by including different physical processes and schemes. From the original basic radiation and boundary layer models to the more recent inclusion of chemistry and aerosols, dry physics models have been developed progressively to produce a hierarchy of increasingly realistic models for climate. We describe this hierarchy of dry physics models below, portraying their progression over the years through the various couplings of sub-model variations.

Dry physics models, especially those tailored to the Earth, have evolved hierarchically by building off one another. The simplest model, presented by Held and Suarez (1994), incorporates Newtonian Cooling and Rayleigh drag schemes that are the basis of many models. Schneider (2004) expanded on the simple Held–Suarez model by incorporating hyperdiffusion (i.e. an iterated Laplacian operator with even derivative order greater than two) and, more importantly, by swapping in a more complex quadratic damping boundary layer scheme. Later Schneider and Walker (2006) introduced a vertical diffusion scheme with a surface flux representation within a 2.5 m fixed height to represent a turbulent boundary layer and include a quasi-equilibrium convection scheme to round out the increase in complexity. Lastly, Mbengue and Woollings (2019) presented a new physics model through the addition of an enhanced quadratic drag on top of the surface flux scheme and extending the height in which vertical diffusion is simulated to 2500 m. Figure 2.1 displays the taxonomy of the Earth dry hierarchy. Starting with the first physics model presented by Held and Suarez (1994) and building in complexity as one moves down the tree.

In contrast, in the case of non-Earth physics models, there has been no straightforward physics model development. In general, the way in which physics is incorporated depends on the planet being modelled. Many models have adapted the cases that were first developed for the Earth, as in the case of Heng et al. (2011), who modified the aquaplanet simulation of Frierson et al. (2006) for a super Earth and removed moist processes. Simultaneously, some non-Earth models, especially in the case of Jupiter, have reduced the number of sub-models, but increased the complexity of each retained model. For example, the physics of Showman et al. (2020) and Amundsen, David S. et al. (2016) includes only model radiation. However the radiation model is comprehensive, including multiple frequency bands and using the correlated-k method to treat opacities with the two-stream formulation. In contrast, a different physics design was explored for modelling hot Jupiters that combines Newtonian cooling with a more complex representation of linear fiction drag term in the boundary layer scheme (Komacek and Showman 2016). Komacek et al. (2017) modifies the model by updating the radiation scheme to a

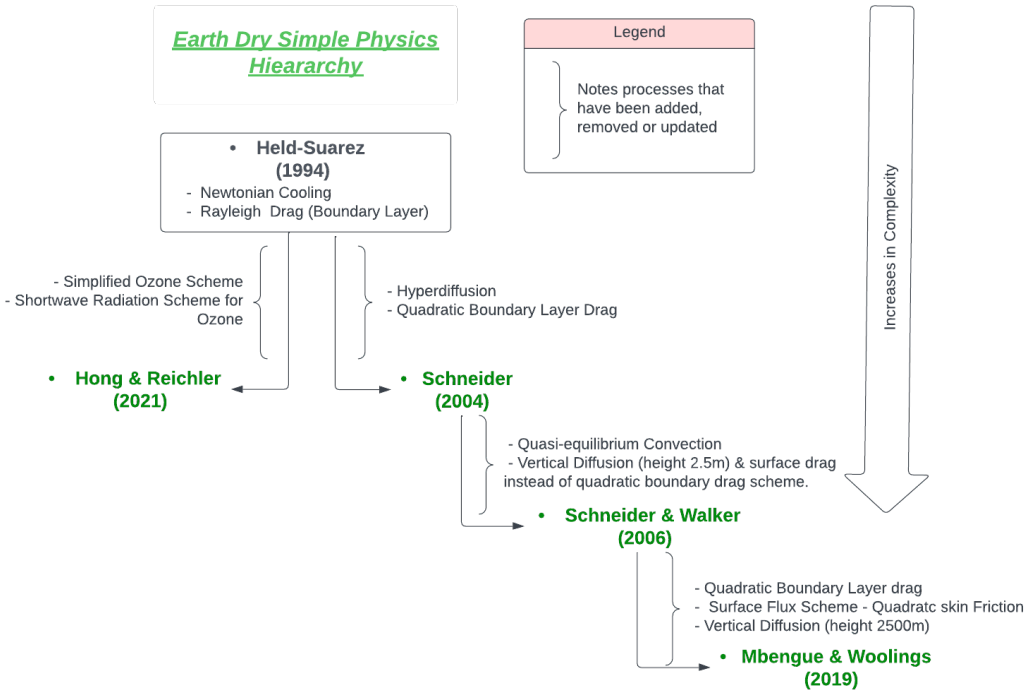

Figure 2.1: Hierarchy of the major dry Earth physics packages, starting with the first physics model presented by Held and Suarez (1994) and stating its physics involved. The figure builds in complexity as one moves down the tree, where the notes beside the arrows indicate any processes that have been added, removed or changed.

dual band two stream approximation and later adding a chemistry scheme for fractional atomic hydrogen (Tan and Komacek 2019).

To demonstrate the versatility of simple dry physics packages, Figure 2.2 displays not only the physics models that differ from the Earth dry physics, but also physics models that have been developed to model Earth and adapted to model different planets, from Hot Jupiter's to a Sub-Neptune. This figure portrays a hierarchy of dry physics models used to model Jupiter and Hot Jupiter's. Starting at the top with the Held-Suarez physics package, the figure displays a branch of only radiation schemes in the physics package coupled with a dynamical. The second branch in the figure illustrates the evolution of the physics package that updates both the boundary layer drag and radiation and ends the branch with a simple chemistry scheme. Lastly, the final branch displays more complex physics packages incorporating convection and vertical diffusion. The figure also displays simple physics packages used to model a Sub-Neptune (Innes and Pierrehumbert 2022) and a brown dwarf (Lee et al. 2020), thus portraying the adaptability of physics packages.

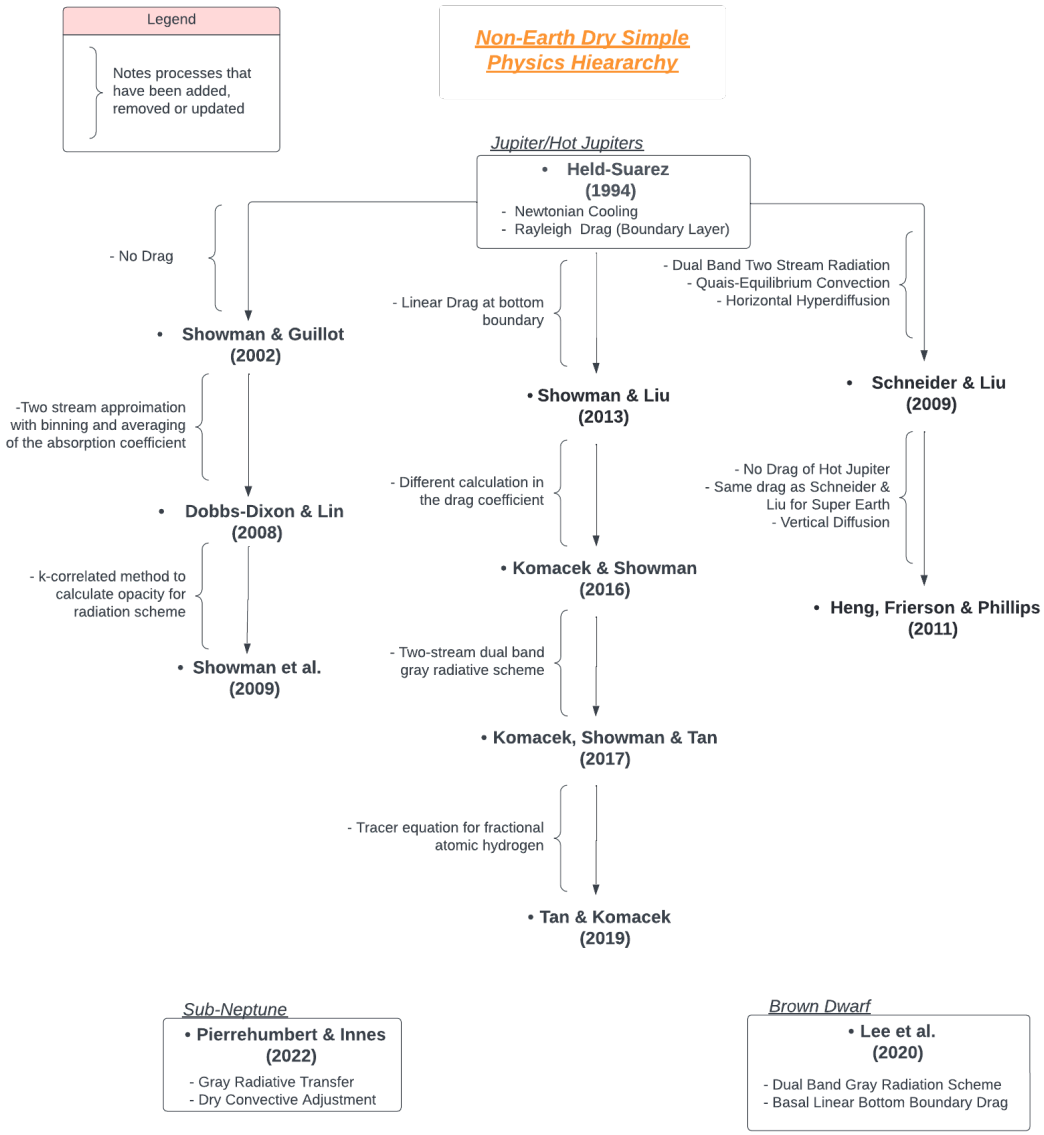

Figure 2.2: Major non-Earth physics packages used to model different planets and portraying the versatility of these models. Some of the models differ from those used to model Earth and add a different complexity as in the case of Tan and Komacek (2019), while other packages use the same physics as used to model earth but adapted for the planet. The figure portrays a package used to model a Sub-Neptune and a Brown-Dwarf, and also provides a small hierarchy of the packages used to model Jupiter and Hot Jupiters. This hierarchy starts with the physics model presented by Held and Suarez (1994) and branches off displaying different physics package usage and evolution. The notes beside the arrows indicate any processes that have been added, removed or changed.

Overall, both Earth and non-Earth dry physics models have expanded over the years via incremental increases in complexity which makes the models increasingly realistic and specialized. At the same time, the simplicity of these dry physics models allows them to be highly versatile and used to model and research a wide range of planets. However, while dry cases are useful in climate modeling, they are often not realistic enough, especially in the cases of planets where condensible moisture plays a significant role. The following section surveys idealized moist physics models.

2.2 Moist physics models

The incorporation of moisture in physics models builds on the dry physics model, and is the next step in the hierarchy of physics models. A moist atmosphere includes phase transitions (e.g. evaporation, from liquid to gas), adding a layer of complexity to the model and affecting the energy budget and thermodynamics. Moist physics packages are most commonly used in aquaplanet simulations. However, one physics package (Reed and Jablonowski 2012) was proposed with the goal of reducing the gap between aquaplanet simulations and dry physics models. This model incorporates schemes for large scale condensation, surface fluxes and boundary layer turbulence of momentum, temperature and humidity. For simplicity, radiation and convection schemes were not included, however they have been explored in the physics of aquaplanet simulations. The following sections will explore the evolution of different physics schemes, beyond the dry models, that have been incorporated by a hierarchy of aquaplanet models.

2.2.1 Aquaplanet sub-model development

Earth aquaplanet simulations have evolved over the years to incorporate a wide variety of physics schemes. Two standards schemes seen in dry physics that are also included in aquaplanet physics are radiation and boundary layer schemes. Simpler Aquaplanet models have incorporated the radiation schemes mentioned in the dry physics models (section 2.1), like Newtonian Cooling, single band gray radiative transfer and dual band two stream approximation (e.g. Thatcher and Jablonowski 2016; Frierson et al. 2006; O'Gorman and Schneider 2008 respectively). However, they have also surpassed those of the dry Earth cases and followed in the footsteps of the Hot Jupiter simulations by including a comprehensive radiative transfer scheme (e.g. Merlis et al. 2013a; Jucker and Gerber 2017; Clark et al. 2018). While the precise form of comprehensive scheme employed differs, they all accounted for multiple frequencies within the shortwave and longwave spectrum and the absorption of different gases. A more in-depth look into the differences between the two schemes can be found in section 2.2.2.

While the simplest boundary layer scheme is Rayleigh friction, Thatcher and Jablonowski (2016) used it not only near the surface of the boundary layer to represent the frictional drag, but also throughout the entire boundary layer to represent horizontal momentum mixing. Furthermore, Frierson et al. (2006) incorporated a more complex boundary layer scheme that accounts for both drag and turbulence, and is used by some of the dry cases.

Drag is incorporated using drag coefficients that act on momentum, temperature and water. They are used in the calculation of the surface fluxes of sensible heat, evaporation and momentum. Drag coefficients could be equal (Frierson et al. 2006), or could be calculated differently as in the case of Clark et al. (2018). Turbulence is parameterized using vertical diffusion, more specifically a K-profile approximation, which is a 1D (column) resolved process that relies on computed diffusion coefficients for momentum, dry static energy and specific humidity (Frierson et al. 2006).

Even though the planetary boundary layer and radiation schemes are sufficient for dry physics models, the same cannot be said for aquaplanet simulations. The simplest physics of an aquaplanet simulation is a moist variant of the Held–Suarez test case, adding in boundary layer surface fluxes for sensible and latent heat and a large scale condensation scheme (Thatcher and Jablonowski 2016). Therefore, in many of these simulations some sort of vertical transport of moisture is modeled, such as convection or condensation.

Due to the incorporation of moisture within aquaplanet simulations, the complexity of convection increases from the dry case to also model convection of moisture and its effects. While convection is a major factor of the general circulation, GCMs can be run without it and Frierson et al. (2006) did this by coupling only a large-scale condensation parameterization. However, to improve upon this approximation the large-scale condensation scheme can be coupled with a convection scheme. For example, Frierson et al. (2007) couple it with a simplified Betts–Miller convection scheme, which is a type of convective adjustment scheme that relaxes the temperature and moisture field to a specified equilibrium profile with a specific relaxation time. O'Gorman and Schneider (2008) also follow the same combination of schemes. However, they adjust the convection scheme by modifying how enthalpy conservation is enforced. Overall, convection is only a part of the circulation and effects of moisture on a planet's climate, but incorporating simplified convection schemes in idealized simulations allows researchers to account for the transport of moisture in the general circulation in an idealized case.

An interesting improvement to aquaplanet simulations is the incorporation of a crude parameterization of land surface conditions. Both Merlis et al. (2013b) and Clark et al. (2020) have a soil parameterization that accounts for the differences in heat capacity and differences in the treatment of evaporation of land compared to the default ocean boundary slab. Merlis et al. (2013b) also accounts for the lack of ocean energy flux over land. While a vertical (column) soil model is not normally considered in an atmospheric test case, it does affect the atmosphere through the land surface heat flux. Incorporating this scheme builds upon the complexity of the physics, but allows researches to explore and understand the effects that soil dynamics (e.g. vertical diffusion of heat) may have in an idealized setting.

2.2.2 Hierarchy of moist physics

As in the dry physics models, the evolution of moist physics, or more specifically moist physics in Earth aquaplanet simulations, builds incrementally. Complexity increases

with the addition of different process parameterizations or by incorporating more complex models of existing effects. Starting with the base aquaplanet of Frierson et al. (2006), the scheme includes a single band gray radiative transfer model, a boundary layer with drag and diffusion coefficients and large scale condensation. These authors further expand upon the physics by incorporating a simplified Betts–Miller convection scheme to build upon the complexity of the transport of moisture (Frierson et al. 2007). Later O'Gorman and Schneider (2008) updated the drag and convection schemes by allowing an unstable boundary layer and changing how the enthalpy conservation was enforced respectively. Furthermore, the single-band two stream approximation evolved to the dual band incorporating the atmospheric absorption of shortwave radiation (O'Gorman and Schneider 2008).

One major jump in realism that occurs next in the hierarchy of the aquaplanet simulations is the addition of a full radiative transfer scheme, first seen by Merlis et al. (2013a) and later by Jucker and Gerber (2017) and Clark et al. (2018). Merlis et al. (2013a)'s radiation scheme include a shortwave and longwave scheme. The shortwave scheme incorporates 18 frequency bands, the absorption of H_2O, CO_2, O_3 and O_2, molecular scattering, ozone profiles and the absorption and scattering by aerosols and clouds. The longwave radiation scheme uses the Simplified Exchange Approximation method to calculate infrared (IR) radiative transfer. The method accounts for absorption and emission of principle gasses and halocarbons and the absorption of aerosols and clouds. Both the longwave a shortwave schemes contain a parameterization for water vapor. In contrast, Jucker and Gerber (2017) use a rapid radiative transfer model that uses the correlated-k method for both shortwave and longwave radiation, in conjunction with a line-by-line model to get the k-distributions. The model includes an ozone profile and absorption of water vapor, CO_2 and O_3. However the roles of clouds and aerosol processes were neglected by Jucker and Gerber (2017), which is a vast difference from Merlis et al. (2013a). Clark et al. (2018) utilized a very similar scheme to Merlis et al. (2013a), but did not include any cloud radiative effects.

Lastly, to build upon the addition of full radiation, both Merlis et al. (2013b) and Clark et al. (2020) added a crude parameterization of land surface to the physics of the simulation. The models includes certain land surface process, for example a limited evaporation reservoir and differences in heat capacity to the ocean, in the lower boundary conditions. Furthermore, Merlis et al. (2013b) accounts of the lack of ocean energy flux divergence over land cells and neglects orography and albedo differences between land and the ocean. This evolution through small changes or additions of new schemes, builds a branch of the hierarchy creating a more realistic climate with more effects as each step is taken. Figure 2.3 displays this branch of the hierarchy indicating the base aquaplanet of Frierson et al. (2006) and its physics, and builds in complexity as one steps down the tree, indicating processes that are added or changed beside the arrows towards a new aquaplanet simulation.

While the previous moist cases and simulations have been presented for Earth, non-Earth planets have also been simulated using moist physics, more specifically aquaplanet

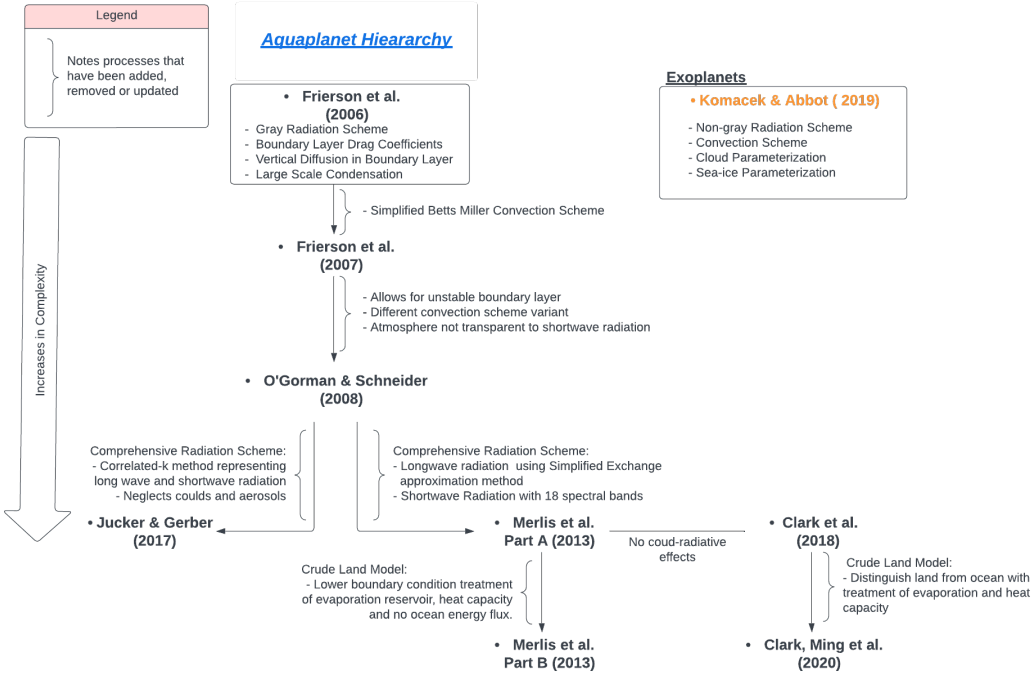

FIGURE 2.3: Hierarchy of the major Aquaplanet simulations, starting with the simulation presented by Frierson et al. (2006) and stating its physics involved. The figure builds in complexity as one moves down the tree, where the notes beside the arrows indicate any processes that have been added, removed or changed.

simulations. The simulations use the physics presented by Frierson et al. (2006) and O'Gorman and Schneider (2008) with slight modifications to the parameters (e.g. Haqq-Misra and Heller 2018; Guendelman and Kaspi 2019) or to one of the schemes, as in the case of Pierrehumbert and Ding (2016) and Merlis and Schneider (2010) updating the convective adjustment scheme and representing longwave water vapor feeback in the radiation scheme respectively. However, Komacek and Abbot (2019) introduced a more complex aquaplanet case for terrestrial planets incorporating a k-correlated radiative transfer and a convection scheme, but more importantly parameterizations for clouds and sea ice, which are not usually seen in idealized models. In general, aquaplanet simulations are idealized models that allow researchers to retain a semblance of simplicity in the model while still including important physical effects. These simulations build another branch in the climate hierarchy that is growing and evolving with time, but from dry physics models to moist aquaplanet simulations there are still gaps that need to be explored.

2.3 Climate hierarchies and gaps

There are many idealized physics models within the research community that make up the climate hierarchy. Nevertheless, important gaps remain. The separation of models into a hierarchy can differ based on the questions asked, and review articles by Jeevanjee et al. (2017) and Maher et al. (2019) provide different perspectives on the climate hierarchy and highlight their gaps. Significant gaps include the processes that govern clouds, circulation and convection, as well as a gap between truly realistic "operational" models and idealized research moist models (Maher et al. 2019; Jeevanjee et al. 2017). The trade-off which Held (2005) originally pointed out between realism and understanding remains for moist GCMs, especially for cloud physics. However, although current efforts are focused on moist models, gaps between the simple dry physics and moist models still need to be addressed.

Turbulence effects, modeled primarily as enhanced vertical and horizontal diffusion of momentum and energy, is a major research area in dry idealized physics that is still not fully understood, but has a huge effect on the atmosphere dynamics. Turbulence enhances the mixing and transport of momentum, heat and, in the moist case, moisture. On Earth turbulence is very important within the planetary boundary layer and thus idealized models have included an under-resolved diffusion scheme (e.g. Frierson et al. 2006; Heng et al. 2011) to simulate this phenomenon. Nevertheless, on Earth, but more importantly on other planets, turbulence also occurs above the boundary layer. For example, within the atmosphere of Venus small scale turbulence is almost always present at about 140 km (Izakov 2012).

The soil is another area that is not usually represented in dry physics model of the atmosphere. While a soil model may be classified as a land process, it has major impacts on the atmosphere. The soil contributes to the net surface flux and surface energy budget of a planet as it temporarily stores and then releases energy. Soil models have been incorporated in the more complex Aquaplanet cases (e.g.Merlis et al. 2013b; Clark et al. 2020). Therefore, the incorporation of a soil model in physics packages could aid in our understanding of how the soil affects a dry atmosphere, while additionally providing more accurate boundary layer constraints. While Held (2005) argued for more work on moist idealized GCMs, he did not wish to de-emphasize the study of dry GCMs, but to rejuvenate it. Held highlights that these dry models will be a gateway into gaining insights and relating them to the comprehensive case (Held 2005).

In attempt to lessen the gap present between dry and moist physics, in the following chapter, this thesis introduces and explains in detail a specific simple dry physics model. This model builds upon the current Earth and Non-Earth dry physics models, incorporating a gray radiation model, dry convective adjustment, a boundary layer scheme and vertical diffusion. In addition, this new model incorporates a multilayer soil model, which increases its complexity beyond those of the current dry physics packages, while maintaining simplicity by leaving out the effects of moisture.

Chapter 3

Simple Dry Physics Model

The following chapter introduces the simple dry physics model which is the focus of the rest of the thesis. This particular simple dry physics model was introduced by Hourdin (1992) and includes sub-models for radiation, convection, turbulence, the atmospheric boundary layer and the soil. Hourdin proposed three variants of the dry physics model, with parameters chosen appropriately for Mars, Venus and Titan. The Venus Global Climate Model (GCM) was used to investigate the phenomenon of "superrotation".

Our goals in focusing on this particular dry physics model is to present and investigate a fairly realistic model with all assumptions and approximations fully described. The simple dry physics model is also referenced as a physics package, as a major objective of the model is the ability to couple with different dynamical cores and the potential to model many planets, including gas giants. The final reason for focusing on this particular model is to develop and test a package that can be coupled to both adaptive and non-adaptive dynamical cores. This sub-grid scale physics parameterization package allows for future investigation into the scale-dependence of certain physics processes and could help reduce the need of climate model tuning with increases in resolution.

This chapter reviews and explains each sub-process included in the model and situates this climate model in the hierarchy described in the previous chapter.

3.1 Physics package usage, input and output

The vertical physics model is intended to be coupled with a dynamical core. This coupling is usually done via a split step method, where the "dynamics" and "physics" components take alternate times steps. The prognostic variables of the physics package are temperature, zonal velocity and meridional velocity. When a physics step is taken, the package outputs the tendencies of the prognostic variables.

One of the major objectives of the package is its versatility in modeling different planets. In order to accommodate this goal, the package initialization allows users to read in input parameters to tailor the simulation to the desired planet. See Appendix A for a full list of the model parameters and their default values. Beyond these parameters, calls to initialization routines set up the logistics of the grid.

3.2 Physics model assumptions

An important aspect of any physics model is to explicitly state all its assumptions and approximations. This not only allows for full transparency, but also avoids inconsistent assumptions when the physics and dynamics are coupled. The basic assumptions of this physics package are dry thermodynamics, compressible flow (i.e. atmosphere, not ocean), hydrostatic approximation, and a floating (Lagrangian) vertical coordinate.

3.2.1 No moisture and compressiblilty approximations

A major approximation of this package is the assumption that no moisture is taken into account. Therefore, the physics package considers the dry case (see section 1.5 for moisture explanation). Secondly, the model assumes the compressible flow. A fluid is compressible if changes in pressure causes significant changes in density. When modeling the atmosphere, the density of dry air changes significantly with changes in atmospheric pressure. Therefore, these two basic assumptions of no moisture and compressibility need to be ensured when coupling with a dynamical core.

3.2.2 Hydrostatic approximation

A fundamental approximation in this simple physics model is the hydrostatic approximation (1.1). The coupled dynamical model must therefore also assume hydrostatic balance (see section 1.2.1). The hydrostatic approximation constrains the vertical coordinates in the model and simplifies the vertical equation of motion. An important implication of the hydrostatic approximation is that dry convection must be parameterized.

3.2.3 Floating vertical coordinate

There are many possible spatial coordinate systems that can be used when modeling a planet. For example, the Cartesian coordinate system, with coordinates (x, y, z), where z is the vertical height above mean sea level. In the case of simplified Atmospheric Global Climate Models (AGCMs), where the dynamics and the physics are coupled, the dynamics works on 2D horizontal planes and the physics works on 1D vertical columns. While z might be one's first choice for a vertical coordinate, other vertical coordinates include pressure, mass and sigma (a normalized pressure coordinate).

Vertical fluxes of heat causes air parcels to expand and compress, and in turn change the density ρ (and associated buoyancy), which is represented in the mass continuity equation by

$$\frac{\partial \rho}{\partial t} + \frac{\partial}{\partial z}(w\rho) = 0, \tag{3.1}$$

where w is the vertical velocity (Dubos 2021).

When altitude z is the vertical coordinate the vertical velocity must be diagnosed from the density, which can be a tedious process. An easier option, implemented in this physics package, is to use a Lagrangian vertical coordinate, sometimes known as

a floating vertical coordinate. In the case of a Lagrangian vertical coordinate ζ, the z coordinate has the form $z = z(\zeta, t)$ and there is no explicit vertical velocity (and no mass flux across vertical layer interfaces) since the horizontal layers move vertically with the local vertical velocity. Therefore, the incremental mass dM is

$$dM = \rho dz = m d\zeta = \rho \frac{\partial z}{\partial \zeta} \partial \zeta \tag{3.2}$$

and $dM/dt = 0$, where $m = \partial M/\partial \zeta = \rho \partial/\partial \zeta$ (Dubos 2021).

3.3 Numerical integration and boundary coupling

3.3.1 Time integration

To solve the system of differential equations at the next time step a numerical integration method is employed. The explicit Euler method is a first-order method commonly used to numerically integrate a system of differential equations. Given an autonomous system of ODEs,

$$\frac{d\mathbf{S}}{dt} = \mathbf{F}(\mathbf{S}(t)), \tag{3.3}$$

where $\mathbf{F}(\mathbf{S}(t))$ is called the "tendency". The stencil of the Explicit Euler method is given by the linear Taylor series approximation of $\mathbf{S}(t*) = \mathbf{S}(t + \tau) + O(\tau^2)$

$$\mathbf{S}(t*) = \mathbf{S}_t + \tau \mathbf{F}(\mathbf{S}_t) \tag{3.4}$$

where:

- t is the current time
- τ is the time step (assumed fixed)
- $t* = \mathrm{t} + \tau$ is the time at the next discrete time
- $\mathbf{S}_t$ is the numerical approximation of $\mathbf{S}(t)$, $\mathbf{S}_t \approx \mathbf{S}(t)$.

A variety of time integration methods have been developed from the Explicit Euler method by making different approximations for the tendency of $\mathbf{S}$, $\mathbf{F}(\mathbf{S})$, (e.g. Runge-Kutta schemes). These methods differ in their order of accuracy and numerical stability properties. In the Explicit Euler method the tendency is simply approximated as $\mathbf{F}(\mathbf{S}_t)$, where the values of $\mathbf{S}$ are at time t. The implicit Euler method improves numerical stability by using the tendency for $\mathbf{S}$ at the the next time step ($\mathbf{F}(\mathbf{S}_{t*})$). This requires more computation since a linear system must be solved at each time step, in general. However, Implicit Euler has a much wider stable domain compared to the Explicit Euler method, allowing for a larger time step and increasing its desirability. The radiation model uses Explicit Euler, while the soil and turbulence models use Implicit Euler.

3.3.2 Boundary coupling

Since the sub-components of the physics are air and soil, the way in which they are coupled is integral when looking at the evolution in time. The two components are coupled via their boundaries, which is the horizontal interface between the soil and air (i.e. the ground), and the boundary conditions need to be taken into consideration and coupled when evaluating the tendencies of the two components. The simplest boundary coupling is explicit, and the boundary conditions are evaluated at time t from the previous state. Therefore, the time integration equation includes the boundary conditions $\mathbf{q_t}$,

$$\mathbf{S}_{t*} = \mathbf{S}_t + \tau \mathbf{F}(\mathbf{S}_t, \mathbf{q}_t). \tag{3.5}$$

Since the air and soil are strongly coupled, coupling the boundary conditions implicitly is desirable for improved stability. (Note that both the soil and air physics strongly affect temperature.) Therefore, the boundary conditions are evaluated at time $t*$. The tendency is approximated as

$$\mathbf{F}(\mathbf{S}(t), \mathbf{q}(t)) \approx \mathbf{F}(\mathbf{S}_t, \mathbf{S}_{t*}, \mathbf{q}_t, \mathbf{q}_{t*}) \tag{3.6}$$

$$\mathbf{S}_{t*} = \mathbf{S}_t + \tau \mathbf{F}(\mathbf{S}_t, \mathbf{q}_t) + \frac{\partial \mathbf{S}_{t*}}{\partial \mathbf{q}_{t*}}(\mathbf{q}_{t*} - \mathbf{q}_t), \tag{3.7}$$

where $\partial \mathbf{S}_{t*}/\partial \mathbf{q}_{t*}$ represents the dependence of $\mathbf{S}_{t*}$ on future boundary conditions (Dubos 2021).

3.3.3 Spatial discretization

The physics package models the effects of the small scale unresolved physics on each 1D vertical column on the sphere, taking the current state of the prognostic dynamical variables as inputs. The vertical discretization is a block cell discretization, with all prognostic variables located at the center of each layer cell, while the fluxes are located at the interfaces between each layer. Each column has N layers, which is an input parameter to the package from the dynamics. There are a total of $N + 1$ interfaces, where the surface (ground) interface has index 0 and top interface (top of atmosphere) has index N. The soil column is considered separately, with negative indices. Figure 3.1 displays a portion of a vertical atmosphere column with grid points $k - 1, k$ and $k + 1$, the related fluxes into each cell and the distance between interfaces. With the chosen floating vertical coordinate the size of each cell layer (Δz_k) may change over time.

3.4 Model parameterizations

The physics package includes parameterizations for radiation, small-scale turbulence, a planetary boundary layer surface scheme, convection and soil. All models are one dimensional in space, and therefore are applied independently to each 1D vertical column on the sphere (i.e. the physics package takes as input a set of vectors).

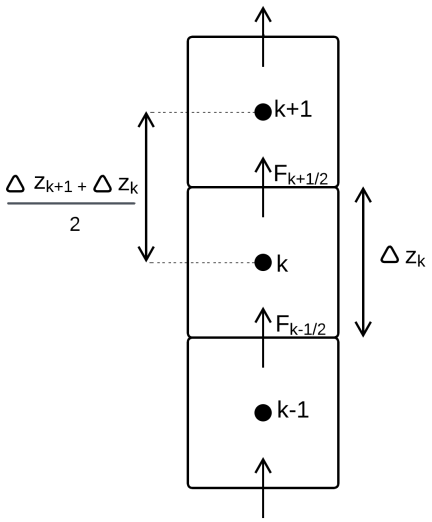

FIGURE 3.1: A portion of a single vertical column, displaying the block cell vertical discretization for layers $k-1, k$ and $k+1$. The prognostic variables are taken at the grid points at the center of each layer cell, while fluxes occur at the interfaces of the cell. With a floating vertical coordinate, the vertical size of each cell layer may change over time.

3.4.1 Radiation

Radiation is a process that has a major impact on the atmosphere. In general, since radiation is not a dynamical process and due to its vast complexity, the process is simplified through a parameterization.

The radiation model included in the physics package is based on the two-stream approximation. The two-stream approximation equations assume the plane-parallel assumption, in which radiation is a function of height and not the horizontal coordinates. The equations yield the downward and upward flux at a specific frequency ν and height z. They are defined as

$$\begin{aligned} F_+(\nu, z) &= F_+(\nu, 0)\tau_\nu(0, z) + \int_0^{z'} \pi B(\nu, T(z'))K(\nu, z')\tau_\nu(z', z)\, dz' \\ &= F_+(\nu, 0)\tau_\nu(0, z) + \int_0^{z'} \pi B(\nu, T(z'))\frac{\partial \tau_\nu(z', z)}{\partial z'}\, dz' \qquad (3.8) \\ F_-(\nu, z) &= F_-(\nu, \infty)\tau_\nu(z, \infty) + \int_{z'}^{\infty} \pi B(\nu, T(z'))K(\nu, z')\tau_\nu(z, z')\, dz' \\ &= F_-(\nu, \infty)\tau_\nu(z, \infty) - \int_{z'}^{\infty} \pi B(\nu, T(z'))\frac{\partial \tau_\nu(z, z')}{\partial z'}\, dz', \qquad (3.9) \end{aligned}$$

where the + subscript indicates an upward flux and the − subscript indicates a downward flux (Pierrehumbert 2010). $B(\nu, T(z')$ is Planck's function:

$$B(\nu, T(z')) = \frac{2h\nu^3}{c^2(e^{h\nu/kT(z')} - 1)}, \tag{3.10}$$

where h is Planck's constant.

$\tau_\nu(z, z')$ is the transmission function, which represents the proportion of the incident radiation, at frequency ν, which is transmitted through the atmospheric layer from z to z' (Pierrehumbert 2010). Therefore, it is the proportion of the flux that is not absorbed and in this model it is crudely represented by

$$\tau(z, z') = e^{-|\psi(z)-\psi(z')|^\alpha}, \tag{3.11}$$

where ψ is a monotonic function and α represents the absorption weight (Dubos 2021). This is known as a band averaged transmission function as it approximates the transmission function over a frequency band. The particular transmission function differs depending on the radiation band, thus the monotonic function in the physics package will differ among the bands. In general, transmission functions are multiplicative, however, due to band averaging of the transmission function this property is lost (Pierrehumbert 2010).

$K(\nu, z')$ represents the absorption, at z', of radiation at frequency ν, and is dependent on the infrared absorbers (i.e. gas) in the atmosphere,

$$K(\nu, z') = \sum_i \rho_i \kappa_i(p, T, \nu), \tag{3.12}$$

where $\kappa(p, T, \nu)$ is the absorption coefficient of gas i and ρ is the density of the gas i.

In general the transmission function τ_ν is a function of $K(\nu, z')$. Due to the band averaging of the transmission function, $K(\nu, z')$ is not explicitly defined. However the band averaged transmission function does describe strong or weak absorption of a frequency band through α. A strong absorption depicts a steep decay of transmission and strong absorption of radiation over shorter paths (Pierrehumbert 2010). This means for longer paths the absorption in the first part of the path is stronger, while a weaker absorption is seen further along in the path. Therefore strong absorption is usually used for frequencies that are absorbed first in a path.

To solve for the net upward and downward irradiance, the fluxes need to be integrated over all frequencies. The physics packages uses the dual band two-stream approximations by crudely integrating the fluxes over two spectral bands, longwave (L) and shortwave (S). Therefore the net flux of radiation is

$$F_{rad} = \int_0^\infty F_-(\nu, z) - F_+(\nu, z)\, d\nu = F_L(z) - F_S(z), \tag{3.13}$$

where F_L and F_S are the net longwave and shortwave fluxes respectively.

Shortwave radiation

The shortwave net flux is a culmination of the upward and downward flux with respect to shortwave radiation,

$$F_S(z) = F_{S+}(z) - F_{S-}(z). \tag{3.14}$$

The two stream approximations contains terms for the proportion emitted from the ground or top of the atmosphere, transmitted through the atmosphere (the 1st term in both F_+ and F_- respectively) and the proportion emitted by the atmosphere (the second term). The simple physics case neglects the atmospheric emission of shortwave radiation, leaving the single initial terms as the upward and downward flux,

$$F_{S-}(z) = \tau_S(z, \infty)\mu S \tag{3.15}$$
$$F_{S+}(z) = \tau_S(0, z)F_{S+}(0) \tag{3.16}$$

where S is the downward flux at the top of the atmosphere, which in the case of shortwave radiation is the solar flux and μ is the cosine of the zenith angle (Dubos 2021). The solar flux represents the amount of flux from the solar star impinging on the outer atmosphere. The upward flux at height z (Equation 3.16) represents the proportion of the upward flux at the ground transmitted through the atmosphere, while the downward flux represents the proportion of the incident solar flux transmitted through the layer at z.

The boundary upward flux of radiation, $F_{S+}(0)$, is the portion of downward shortwave radiation that is reflected by the ground,

$$F_{S+}(0) = -(1 - \alpha)F_{S-}(0), \tag{3.17}$$

where α is the albedo, which depends on the reflective properties of the ground ($\alpha \approx 1$ for fresh snow, $\alpha \ll 1$ for forests). Therefore there is no shortwave radiation emitted by the ground itself, however the ground does emit longwave (heat) radiation and is taken into consideration in the longwave fluxes described below.

The transmission factors for the shortwave spectral band are approximated as

$$\tau_S(z, \infty) = e^{-\frac{\psi(z)}{\mu}} \tag{3.18}$$
$$\tau_S(0, z) = e^{-\frac{\psi(0)-\psi(z)}{\mu_0}} \tag{3.19}$$
$$\psi(z) = c_S \frac{p(z)}{p_{ref}}, \tag{3.20}$$

where p_{ref} is a reference pressure close to the surface and c_S is a tunable parameter measuring the opacity of the atmosphere to shortwave radiation (Dubos 2021). μ is the cosine of the zenith angle and μ_0 is an average of μ, $\mu_0 = \frac{3}{5}$.

Longwave radiation

The longwave radiative fluxes in the simple physics package are represented using the gray gas approximation of the two-stream equations. As in the case of the shortwave net flux, the longwave net flux is determined by

$$F_L(z) = F_{L+}(z) - F_{L-}(z), \tag{3.21}$$

where $F_{L+}(z)$ and $F_{L-}(z)$ represent the upward and downward longwave fluxes respectively.

A further assumption in the gray gas model is the neglect of longwave solar emission meaning $F_{L-}(\infty) = 0$. Also, since the longwave radiative fluxes are the result of the two-stream approximations (equation 3.4.1) integrated over infrared frequencies, the integration over infrared frequencies of the second term is well approximated by the Stephan–Boltzmann law (Pierrehumbert 2010). More specifically,

$$\int \pi B \frac{\partial}{\partial z'} \tau(\nu, z, z')\, d\nu \approx \sigma T(z)^4 \frac{\partial}{\partial z'} \tau_L(z, z'), \tag{3.22}$$

where σ is the Stephan–Boltzmann constant. Therefore, the downward and upward flux of longwave radiation can be approximated as

$$F_{L-}(z) = \int F_-\, d\nu = -\int \sigma T(z')^4 \frac{\partial \tau_L(z, z')}{\partial z'} dz' \tag{3.23}$$

$$F_{L+}(z) = F_{L+}(z = 0)\tau_L(0, z) + \int \sigma T(z')^4 \frac{\partial \tau_L(z', z)}{\partial z'} dz'. \tag{3.24}$$

The boundary upward flux is comprised of the heat flux emitted from the ground itself and the fraction of the downward atmospheric longwave radiation that is reflected by the ground (i.e. not absorbed by the ground). Therefore,

$$F_{L+}(0) = \epsilon \sigma T_s^4 + (1 - \epsilon) F_{L-}(0), \tag{3.25}$$

where ϵ and T_s^4 represent the emissivity and the the surface temperature (Dubos 2021). The emissivity and the albedo, mentioned in the shortwave section are both characteristics of the ground, but they describe the effects for different wavelengths. The albedo is the fraction of shortwave radiation reflected by a surface, while the emissivity is the effectiveness of a surface, the ground in this case, to emit longwave (heat) radiation. Both parameters are an input to the initialization of the physics package. Rearranging equation 3.26 reveals the net longwave flux at the boundary,

$$F_L(0) = F_{L+}(0) - F_{L-}(0) = \epsilon(\sigma T_s^4 - F_{L-}(0)). \tag{3.26}$$

The transmission factors for the longwave spectral band are represented as

$$\tau_L(z, z') = e^{-\sqrt{|\psi(z')-\psi(z)|}} \tag{3.27}$$

$$\psi(z) = c_L^2 \frac{p^2(z)}{p_{ref}^2}, \tag{3.28}$$

where c_L is a tunable constant representing the longwave radiation opacity of the atmosphere (Dubos 2021).

Upon discretization, the longwave equations are computed as,

$$F_{L-}(l) = \sum_{k>l} (\tau_L(l, k_-) - \tau_L(l, k_+))\sigma T(k)^4 \tag{3.29}$$

$$F_{L+}(l) = F_{L+}(z=0)\tau_L(0, z) + \sum_{k<l} (\tau_L(k_+, l) - \tau_L(k_-, l))\sigma T(k)^4, \tag{3.30}$$

where l is the layer interface and k is the center of the layer (Dubos 2021). Therefore k_+ and k_- represent the interfaces above and the below layer k respectively.

The warming or cooling of a layer is affected by the net change in radiation with height and is derived from the conservation of energy equation. This gives an impression for the temperature tendency

$$\frac{\partial T}{\partial t} = -\frac{1}{\rho c_p} \frac{\partial F_{rad}}{\partial z}, \tag{3.31}$$

where c_p is the specific heat capacity of the air (Arya 1988).

Finally, the change in net radiative transfer with respect to the surface temperature is (Dubos 2021)

$$\frac{\partial F_{rad}(l)}{\partial T_s} = 4\epsilon\sigma T_s^3 \tau_L(0, l). \tag{3.32}$$

This relation is used for the implicit coupling at the boundary.

3.4.2 Small-scale turbulence

Turbulence has a major impact on the dynamics of atmospheric flow. In general, turbulence spans a large range of spatial and time scales, from sub-millimetre to kilometres. More importantly for us, the computational cost of computing an integral time scale of a homogeneous 3D turbulent flow scales like Re^3, where Re is the non-dimensional Reynolds number characterizing the turbulence. Since $Re = O(10^8)$ for the atmosphere, it is clear that turbulence cannot be fully represented at the resolved scales and at least some turbulent length scales must be parameterized. This parameterization represents the effects of turbulence at the unresolved small scales on the resolved large scales.

When modeling turbulence, a statistical averaging method, like Reynolds averaging, is used due to the high variability of prognostic variables caused by turbulence. Turbulent

fluxes represent the fluctuation of desired quantities, for example heat or momentum, from the mean flow, and needs to approximated, due to the closure problem (more unknowns than equations) that occurs when Reynolds averaging is applied. There are a multitude of approximations, for example first order closure approximation (e.g. mixing length model) and second order approximations such as the k-ϵ model.

Recall that the prognostic variables are assumed to be quantities averaged over large scales L and long times T (i.e. they are the "large scale" or coarse-grained resolved by the dynamics model). The effect of the unresolved parameterized turbulence on the prognostic variables is modeled as an enhanced vertical diffusion in their tendencies. As mentioned earlier, turbulence is active on a continuous and wide range of length scales. In a turbulent flow turbulent kinetic energy (TKE) is transferred progressively from large scales to smaller scales, until it is eventually dissipated as heat at the dissipation scale $O(LRe^{-3/4})$, where L characterizes the large scales. TKE is dissipated as heat at the rate ϵ, which therefore also corresponds to the dissipation rate of the large scale resolved kinetic energy K due its conversion into (unresolved) TKE, denoted k. To ensure conservation of energy, ϵ must be included as a source term in the heat equation (3.39).

Since turbulence is assumed to act as an enhanced diffusion, the vertical flux of a quantity q is given by

$$F_q = -\rho K_z^q \frac{\partial q}{\partial \zeta}, \tag{3.33}$$

where

- ρ is the density,
- K_z^q is a variable "eddy viscosity" (to be modeled),
- $\partial q/\partial \zeta$ is the vertical gradient of q (Stull 1988).

In general, the value of the eddy viscosity K_z^q depends on q. However, the physics package assumes that the eddy diffusivity is the same as the eddy viscosity, $K_z^\theta = K_z^u$ (Hourdin 1992).

The eddy viscosity is computed based on a mixing length model, where K_z^u is proportional to the vertical shear and the square of a "mixing length" l. The mixing length is the mean distance over which the quantity q becomes fully mixed by the turbulence. In addition, the eddy viscosity is proportional to a nonlinear term that measures the net production of turbulence by buoyancy and velocity shear instabilities.

$$K_z^u = l^2 \left|\left|\frac{\partial \mathbf{u}}{\partial z}\right|\right| \sqrt{1 - \frac{Ri}{Ri_c}}. \tag{3.34}$$

Computing the eddy viscosity K_z^u therefore requires the vertical gradient of the horizontal velocity (the shear), the gradient Richardson's number (Ri), the critical Richardson's number ($Ri_c = 0.4$) and the mixing length l. Note that all these quantities can be diagnosed from the prognostic variables provided by the dynamics.

The mixing length is modelled by

$$l(z) = \left(\lambda^{-1} + \frac{1}{\kappa(z+z_0)}\right)^{-1}, \tag{3.35}$$

where κ is the Von Karman constant and λ is a tunable constant (Dubos 2021).

The gradient Richardson's number (Hourdin 1992) is approximated as,

$$Ri = \frac{\frac{g}{\theta}\frac{\partial\theta}{\partial z}}{\left|\left|\frac{\partial \mathbf{u}}{\partial z}\right|\right|^2}, \tag{3.36}$$

the ratio between the buoyant production and consumption of turbulence (represented by the numerator) and the wind shear production of turbulence. Ri_c is a dynamic stability criteria: when $Ri < Ri_c$, there is a net production of turbulence. In the case of $Ri > Ri_c$, a minimum turbulent kinetic energy (e_{min}) is imposed to ensure a minimum vertical dissipation. In this case, the diffusion coefficient is modeled by (Hourdin 1992),

$$K_z^u = l\sqrt{e_{\text{min}}}. \tag{3.37}$$

The physics model for velocity is therefore simply given by a diffusion equation (Fick's second law),

$$\frac{\partial \mathbf{u}}{\partial t} = \frac{\partial}{\partial \zeta}\left(K_z^u \frac{\partial \mathbf{u}}{\partial \zeta}\right), \tag{3.38}$$

where the eddy viscosity K_z^u is given by (3.34). Note that the diffusion equation leads to dissipation of large scale kinetic energy K at the rate ϵ. The SGS physics model for heat includes a turbulent diffusion term, a radiative flux term and a source term due to heating (due to the dissipation of TKE and, indirectly, from the dissipation of K),

$$h_\theta \frac{\partial \theta}{\partial t} = \frac{\partial}{\partial \zeta}\left(h_\theta K_z^\theta \frac{\partial \theta}{\partial \zeta}\right) - \frac{\partial F_{rad}}{\partial \zeta} + \epsilon, \tag{3.39}$$

where θ is the potential temperature, h is the enthalpy, $h_\theta = \partial h/\partial\theta$. Recall that we assume that $K_z^\theta = K_z^u$.

The equation for resolved kinetic energy $K = 1/2\|\mathbf{u}\|^2$ is derived from the prognostic equation for velocity (3.38) by taking its inner product with $\mathbf{u}$ and rearranging,

$$\frac{\partial K}{\partial t} + \frac{1}{\rho}\frac{\partial \mathbf{F}_K}{\partial \zeta} = -\epsilon \tag{3.40}$$

where $\mathbf{F}_K = \mathbf{u}\cdot(\frac{1}{\rho}F_u\hat{\mathbf{z}})$ is the vertical flux of K, and

$$\epsilon = -(\frac{1}{\rho}F_u\hat{\mathbf{z}})\cdot\frac{\partial \mathbf{u}}{\partial z} = K_z^u\left|\left|\frac{\partial \mathbf{u}}{\partial z}\right|\right|^2. \tag{3.41}$$

Since our turbulence model is only a first order closure approximation, there is no need for a model equation for ϵ: it is diagnosed directly from the prognostic variables. It is assumed that the part of the resolved kinetic energy that is dissipated at rate ϵ is instantaneously converted to heat (rather than first being converted to TKE). The heat equation (3.39) must therefore include a corresponding source term ϵ.

In contrast, in the second-order k-ϵ model, the eddy viscosity $K_z^u \propto k^2/\epsilon$, where k is the (unresolved) small scale TKE. K_z^u therefore depends on two unresolved quantities that must be modeled. They are computed by solving two coupled time-dependent model equations for their tendencies.

With a block cell vertical discretization, as explained in section section 3.3.3, the tendency equation for momentum, discretized at cell layer k is

$$D_t \mathbf{u}_k = -\frac{1}{\rho_k} \frac{\mathbf{F}_{k+1/2} - \mathbf{F}_{k-1/2}}{\Delta z_k}, \tag{3.42}$$

$$\mathbf{F}_{k+1/2} = \left(K^u \frac{\partial u}{\partial z} \right)_{k+1/2} = K^u_{k+1/2} \frac{u_{k+1} - u_k}{\frac{1}{2}(\Delta z_{k+1} + \Delta z_k)} \tag{3.43}$$

$$\mathbf{F}_{k-1/2} = \left(K^u \frac{\partial u}{\partial z} \right)_{k-1/2} = K^u_{k-1/2} \frac{u_k - u_{k-1}}{\frac{1}{2}(\Delta z_k + \Delta z_{k-1})}, \tag{3.44}$$

where $D_t \mathbf{u}_k$ is the material derivative of momentum and $\mathbf{F}_{k-1/2}$ is the vertical turbulent momentum flux at interface $k + 1/2$. The tendency equation for heat follows the same scheme as the momentum equation,

$$h_\theta D_t \theta_k = -\frac{1}{\rho_k} \frac{\mathbf{F}_{k+1/2} - \mathbf{F}_{k-1/2}}{\Delta z_k} \tag{3.45}$$

$$F_{\theta,k+1/2} = \left(K^u \frac{\partial \theta}{\partial z} \right)_{k+1/2} = K^u_{k+1/2} \frac{\theta_{k+1} - \theta_k}{\frac{1}{2}(\Delta z_{k+1} + \Delta z_k)} \tag{3.46}$$

$$F_{\theta,k-1/2} = \left(K^u \frac{\partial \theta}{\partial z} \right)_{k-1/2} = K^u_{k-1/2} \frac{\theta_k - \theta_{k-1}}{\frac{1}{2}(\Delta z_k + \Delta z_{k-1})}, \tag{3.47}$$

where the turbulent dissipation rate ϵ is neglected and $\mathbf{F}$ is the total heat flux, incorporating both the turbulent and radiative heat flux. These equations are completed by Neumann (flux) boundary conditions at the bottom and top of each vertical column. The flux at the top of the atmosphere is assumed to be zero for both velocity and potential temperature, $F_{u,N} = F_{\theta,N} = 0$, while the fluxes at the ground, $F_{u,0}, F_{\theta,0}$ are provided by the surface flux parameterization scheme discussed in the following section.

The radiative heat flux is computed by the radiative transfer scheme and is an input to the turbulence model. During a time step the inputs to the model are the surface temperature and surface heat flux at the surface boundary, while the outputs of the model are the tendencies for velocity and potential temperature due to the parameterized SGS processes.

3.4.3 Surface flux scheme

The surface heat and momentum drag flux are computed using the inputs of z, θ and u, at the very first layer center of the column ($k = 1$). The parameterization for the fluxes are the bulk formulae of Louis (1979), which is based on the Monin–Obukhov similarity theory for boundary layer turbulence that describes vertical profiles of velocity and potential temperature as a function of height z and the Obukhov length L, z/L. The flux model uses the following parameters, derived by Louis (1979):

$$
\begin{aligned}
a &= \frac{\kappa}{\ln(z/z_0)} & c^* &= 2bC^*a^2\left(\frac{z}{z_0}\right)^{1/2} \\
b &= 4.7 & f^* &= 1 - \frac{2bRi_B}{1 + c^*\sqrt{-Ri_B}} \quad (if\ Ri_B < 0) \\
C^u &= 7.4 & f^* &= \frac{1}{(1 + bRi_B)^2} \quad (if\ Ri_B > 0) \\
C^\theta &= 5.3 & C_D^u &= a^2 u f^u \\
Ri_B &= \frac{gz(\theta - \theta_0)}{\theta u^2} & C_D^\theta &= \frac{a^2 u}{R} f^\theta \\
R &= 0.74, &&
\end{aligned}
$$

where z_0 is roughness length, θ_0 is the potential temperature at z_0, Ri_B is the bulk Richardson's number, κ is the von Karman constant, $* = u, \theta$ and C_D^* are drag coefficients. a represents the drag coefficient in the neutral surface condition case, while the coefficient calculated for $Ri_B < 0$ and $Ri_B > 0$ represents the drag coefficients in the unstable and stable cases respectively. The fluxes have the following form:

$$\mathbf{F}_u = -\rho C_D^u \mathbf{u}, \tag{3.48}$$

$$F_\theta = -\rho C_D^\theta (\theta - \theta_0). \tag{3.49}$$

It is important to note that this parameterization was created empirically using observation data of earth, which includes moisture. Therefore the scheme may not be suitable for modeling dry planets and might requiring tuning when modeling planets whose condensible substances are not water.

3.4.4 Soil

The inclusion of a multi-layer soil model is rare in simple physics models. However, our model includes a simple soil heat flux parameterization in order to provide more accurate and realistic conditions at the surface boundary. In this model the only prognostic variable of the soil is its depth-dependent temperature $T_s(z, t)$, with $z < 0$. The heat flux in the soil is

$$F_s = -k\frac{\partial T_s}{\partial t} \tag{3.50}$$

where

- k is the thermal conductivity in W [K m]$^{-1}$.

From Fick's second law the temperature tendency in the soil is given by the diffusion equation (Hourdin 1992),

$$\frac{\partial T_s}{\partial t} = -\frac{1}{C_p}\frac{\partial F_s}{\partial z} = \frac{k}{C_p}\frac{\partial^2 T_s}{\partial z^2}, \tag{3.51}$$

The heat fluxes are computed at the interfaces of each soil layer in a column, where the interface depths are characterized by:

$$z'_l = \frac{\alpha^l - 1}{\alpha - 1}\sqrt{T}, \tag{3.52}$$

where l represents the index of the interface (Hourdin 1992). Both T and α are tunable constants, and the current default is $\alpha = 2$. The first interface below the surface is $(z'_1 = \sqrt{T})$ and its default portrays the damping depth of the diurnal wave. The damping depth is the depth of a wave of period P whose amplitude is reduced by e (Arya 1988). More generally, the depth of penetration of a wave of period P, in days, is $\sqrt{P}$ (Hourdin 1992). More layers included in the soil model allows for the release of energy at more (longer) time scales, for example a diurnal, monthly and annual time scales.

The spatial discretization of the soil model uses the block cell vertical discretization, where the indexes of the interfaces increases down the soil column, as seen in Figure 3.2. Fluxes at interface l are computed by:

$$F_{s,l} = k\frac{T_{s,l+1/2} - T_{s,l-1/2}}{\frac{1}{2}(\Delta z'_{l+1/2} + \Delta z'_{l-1/2})}, \tag{3.53}$$

where $\Delta z'_{l+1/2} = z'_{l+1} - z'_l$. Therefore, the soil temperature tendency of soil layer $l + 1/2$ is defined by

$$\frac{\partial T_s}{\partial t} = -\frac{1}{C_p}\frac{F_{s,l} - F_{s,l-1}}{z'_l - z'_{l-1}}. \tag{3.54}$$

If there are L_s layers, the Neumann boundary conditions for the soil column are

$$\begin{aligned} F_{s,0} &= F_r + F_H, && (\textit{Flux at ground boundary, } l = 0) \\ F_{s,L_s} &= 0, && (\textit{Flux of bottom soil interface } l = L_s) \end{aligned}$$

where

- F_r is the surface radiative flux
- F_H is the surface heat flux.

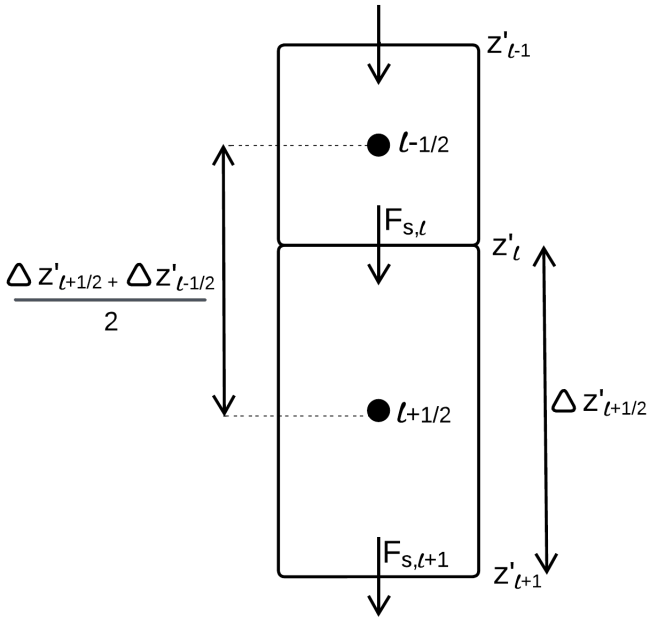

FIGURE 3.2: A portion of a single vertical soil column, displaying the block cell vertical discretization with interface $l-1$, l and $l+1$, where interface indexes increase down the column. The prognostic variables are taken at the grid points at the center of each layer cell ($l+1/2$ or $l-1/2$), while fluxes occur at the interfaces of the cell.

3.4.5 Convection

Convection must be parameterized because the dynamics makes the hydrostatic approximation. The small scale turbulence model only simulates turbulent diffusion, not convection. It could therefore produce an unstable vertical temperature stratification, characterized by $\partial\theta/\partial z < 0$ (Hourdin 1992). The dry convective adjustment scheme of the physics model mitigates any instability by relaxing the temperature to an adiabatic profile.

A layer is unstable if its potential temperature is greater than that of the layers above. The convection parameterization scheme checks each column to see if a layer is unstable. If a particular layer of the 1D vertical column is unstable, local mixing is applied. This local mixing is modeled by a temperature relaxation to a mass weighted temperature average of the unstable layers. This scheme also takes into account the transport of momentum that occurs with convection, through a mixing of momentum in the unstable layers. For each unstable layer in a column only the proportion α of the cell is mixed,

where

$$\alpha = \frac{\int |\overline{\theta} - \theta| \, dp}{\int \theta \, dp}, \tag{3.55}$$

and $\alpha < 0$, which is always verified (Hourdin 1992).

3.5 Placement within the climate hierarchy

While the simple dry physics models is less complex than any aquaplanet simulation, due to the exclusion of moisture, it does relate to the more complex models through the inclusion of a soil scheme. In relation to the current dry physics hierarchy, the dry physics model is vastly different due to the inclusion of a simple soil parameterization. While soil is a process of land, the incorporation of this model is a feature of the simple dry physics package that sets it apart from dry physics models for both Earth and non-Earth planets.

With regards to the remaining sub-models of the simple dry physics package, the dual band two-stream radiation model is an intermediate scheme that many dry non-Earth and wet aquaplanet idealized models incorporate in their physics. The Monin–Obukhov planetary boundary layer scheme and mixing layer turbulence models are used in many aquaplanet and some non-Earth models. Therefore, the simple dry physics package is comparable in complexity to many dry non-Earth and aquaplanet cases with regards to the radiation, planetary boundary layer and turbulence models. However, compared to dry Earth cases, our simple dry physics model is more complex than the usual Newtonian cooling and fixed height boundary layer diffusion schemes. The convection scheme is comparable to many dry models as it is a simple convective adjustment scheme.

In general this physics package adds another branch of complexity to the dry physics hierarchy due to its inclusion of the simple soil model. Nonetheless the inclusion of simpler radiation, convection and boundary layer schemes keeps the physics package simple while maintaining an air of realism.

Ultimately the goal of focusing on this particular simple dry physics model is to present and investigate a physics model that has the potential to couple with a multitude of dynamical cores, model different planets and can be used as a test case in adaptive research. Including schemes for radiation, convection and turbulence, this dry physics model is comparable to many non-Earth and aquaplanet physics. In the end what sets the simple dry physics model apart, is the incorporation of a soil parameterization.

Chapter 4

Equilibrium State of the Uncoupled Physics Model

While the physics model is intended to be coupled with a dynamical core, it is useful to characterize its dynamics and equilibrium states in the absence of a dynamical model. This ensures that the physics model is not producing surprising results, and helps us understand its intrinsic timescales and equilibrium solutions.

The goal of this chapter is to present the diagnostics for the driver to run the physics uncoupled to a dynamical core, as well as results from a series of simple experiments. The results include time series for vertical profiles of temperature and velocity, as well as the statistically stationary (equilibrium) temperature profile. This equilibrium profiles is compared with the simple Held–Suarez physics model (Held and Suarez 1994) and the standard atmosphere.

4.1 Features of the driver

The driver is the facilitator of the entire simulation and it acts in place of the dynamical core. It does not produce any dynamics, but sets the constants of the planet being modeled, the physical model constants (e.g. the number of columns, the number of vertical layers and length of the simulations), the initial values of the prognostic and diagnostic variables and the latitude and longitude of the columns of the atmosphere used by the physics. Also, as the facilitator, the driver runs the package initialization routine and calculates the values of the prognostic variables at the next physics time step based on prognostic variable tendencies (the time derivatives) calculated by the physics package. The constants used in the physics-only simulations are found in Table 4.1 and 4.2, while the package initialization of input parameters uses the default values, except in the case of the real gas constant, as explained in section 3.1. These constants and parameters are Earth-like. Specifically, the axial tilt of the planet used for the simulations is 23°, indicating that the effects of seasons should be present in the temperature time series.

To keep the initial temperature condition simple, the temperature of the initial state, in Table 4.2, represents an isothermal temperature profile. While it would be more realistic to have an initial temperature depend on latitude, a horizontally uniform isothermal profile is a simple initial condition that has been used in Dynamical Core Intercomparison Projects (DCMIPs) (e.g. Kent et al. (2014)). Furthermore, the top boundary pressure places some layers in the stratosphere, allowing the simulation to include its temperature trend prediction for the lower stratosphere. To observe higher into the atmosphere, more atmospheric layers are required. However, this may not be possible with the available computational power. The variables initialized by the driver for each column include the pressure at the interfaces, the pressure at the center of each layer, the zonal velocity of each layer and the meridional velocity of each layer. The following sub-sections explain the chosen initializations and grid coordinates utilized in the physics package only simulations.

solar days	86 400 s
planet radius	6.4×10^6 m
gravity	9.8 m $[\text{s}]^{-1}$
heat capacity of dry air C_p	1004 J kg $[\text{K}]^{-1}$
gas constant of dry air	287 J kg $[\text{K}]^{-1}$
axial tilt/obliquity	23°

Table 4.1: The planet-dependent constants set in the driver based In this section the planet and its corresponding constants are based on Earth.

Variable	**Value**
number of columns	1000
number of layers per column	30
number of days for the simulation	3650 days
simulation time step	1 hr
planet surface pressure	10^5 Pa
pressure at the top interface	10^{-2} Pa
initial temperature of all layers	250 K

Table 4.2: The constants and values for physics model simulations. The values depicted are the ones used in the simulation exploring the physics package equilibrium.

4.2 Pressure initialization

The initialization of pressure at the layers and layer interfaces depends on the vertical coordinate. Based on the chosen vertical coordinate, the pressure is initialized such that the change in pressure between the interfaces are equal (i.e. equal pressure increment coordinates). Therefore, given the total number of layers of a column N and the pressure

at the top p_{top} and surface p_{surf} of the atmospheric region, the change in pressure and the pressure at an interface l and layer center k is given by:

$$\begin{aligned}
\Delta p &= \frac{p_{top} - p_{surf}}{N}, \\
p_l &= p_{surf} + l(\Delta p), && \textit{(pressure at interface } l\textit{)} \\
p_k &= p_{surf} + l(\Delta p) - \frac{1}{2}\Delta p. && \textit{(pressure at layer } k\textit{)}
\end{aligned}$$

4.3 Velocity initialization

The zonal and meridional velocity are initialized using an Ekman layer vertical profile. The equations of motion are given by balance of forces between the Coriolis force, the pressure gradient and the vertical turbulent diffusivity:

$$-fv = -\frac{1}{\rho}\frac{\partial p}{\partial x} + K_m \frac{\partial^2 u}{\partial z^2} \tag{4.1}$$

$$fu = -\frac{1}{\rho}\frac{\partial p}{\partial y} + K_m \frac{\partial^2 v}{\partial z^2}, \tag{4.2}$$

The solutions to these equations are

$$u = u_g(1 - e^{-z/d}\cos(z/d)) \tag{4.3}$$

$$v = v_g(1 - e^{-z/d}\sin(z/d)), \tag{4.4}$$

where the model parameters are

- $d = \sqrt{2K_m/f}$, the thickness of the Ekman layer.
- $\mathbf{u}_g = (u_g, v_g)$, is the geostrophic wind (given by setting $K_m = 0$).

To avoid discontinuities at the poles, the zonal and meridional initial values are set, in all layers and horizontal positions, by multiplying equations (4.3) and (4.4) with $\cos\theta$, where $d = 10000$ m, $U_0 = 30$ m/s and θ represents the latitude of the column.

The Ekman solution is not commonly used as an initial condition for Earth climate simulations. Geostrophic balance solutions are more common (e.g. Willson et al. (2023)). However, the upper layer of the planetary boundary layer, which can cover 90% of the boundary is an Ekman layer (Rohli and Li 2021). The use of an Ekman layer as the initial velocities is a simplification of the flow, especially near the surface, as it assumes the flow of the entire atmosphere is that of the Ekman layer. Nevertheless, the goal is to start the system off in balance, and once the physics or dynamics is applied to the initial state, it is expected the results will reach an statistical equilibrium steady state.

4.4 Latitude and longitude coordinates of columns

To ensure that the simulations include a statistical uniform sample of columns over the entire Earth, the following equations are used to calculate each pair of latitude (θ) and longitude (ϕ) coordinates in radians:

$$\theta = \arcsin(U(-1, 1)), \qquad (Latitude)$$
$$\phi = U(0, 2\pi), \qquad (Longitude)$$

where $U(x, y)$ is a number uniformly distributed between x and y. These distributions ensure that there are more points chosen at the mid-latitudes, instead of a uniform distribution of columns at the poles and mid-latitudes. To ensure sufficient sampling over the sphere we set the number of columns to 1000. Figure 4.1a and 4.1b displays the location of each column. These figures show a good distribution and covering of the sphere.

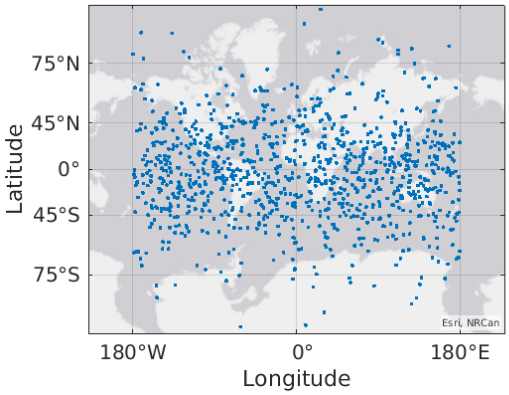

(a) 1000 columns on 2D graph.

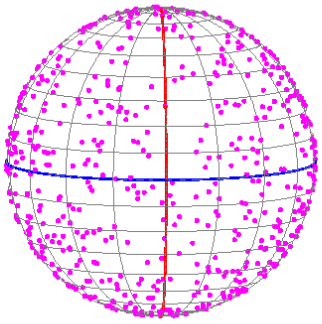

(b) 1000 columns on 3D sphere.

FIGURE 4.1: Figure (a) is a 2D depiction of the coordinates of all 1000 columns on the Earth. Figure (b) displays the coordinates of some of the columns near the prime meridian in red and the equator in blue on a sphere.

4.5 Temperature and velocity time series

An important property of the physics model is its ability to reach a steady state or statistical equilibrium in a reasonable time (say, several years) in the absence of coupling to a dynamical core. This allows climatology to be characterized with a feasible computational cost. A simulation of 30 years was run and the mean averages for each prognostic variable over each layer was calculated and plotted on a time series graph.

Figure 4.2 displays a 30 year times series of the temperature averaged over the entire sphere, for every third vertical layer (11 layers). The figure shows the temperature times

series in fact reaches a statistical equilibrium with a repeated annual cycle after about two years, in each vertical layer.

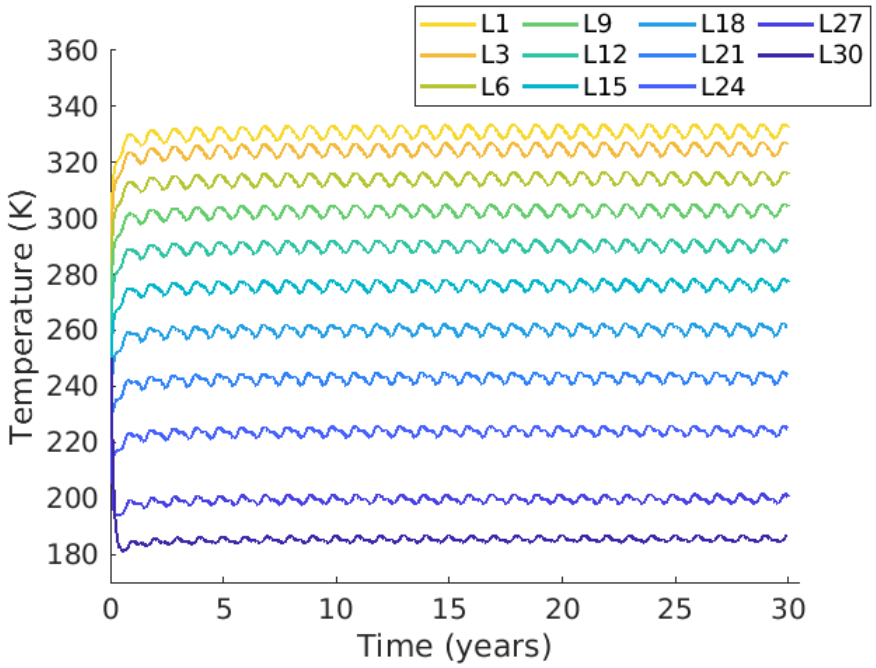

Figure 4.2: 30 year time series of the average temperature over the sphere for every third layer out of the 30 layer atmosphere. The series displays the temperature reaching a statistical equilibrium with an annual cycle.

Figure 4.3a and 4.3b plots the 30 year times series of both the average zonal and meridional velocity over the sphere for every other layer of the lower 15 layers of the atmosphere of the model. The figures display that, without coupling to the dynamics, both velocities decay over the 30 years in the lower layers. Figure 4.3c and 4.3d displays the 30 year times series of the averaged velocities of the upper layers to observe their trend. Most of the upper layers decay to zero over the 30 year period. We expect the velocities to decay towards zero, as there is friction at the surface and no horizontal dynamics. Conversely the velocities in the stratosphere layers 28 and 30 appear not to have decayed over the 30 years. However, upon closer inspection, these two layers do decay very slightly. Due to the higher altitude of theses layers it is expected that surface friction will have a delayed and diminished effect. When the horizontal dynamics are included in the simulations, the difference in temperature between the poles and equator causes a horizontal pressure gradient that drives atmospheric flow.

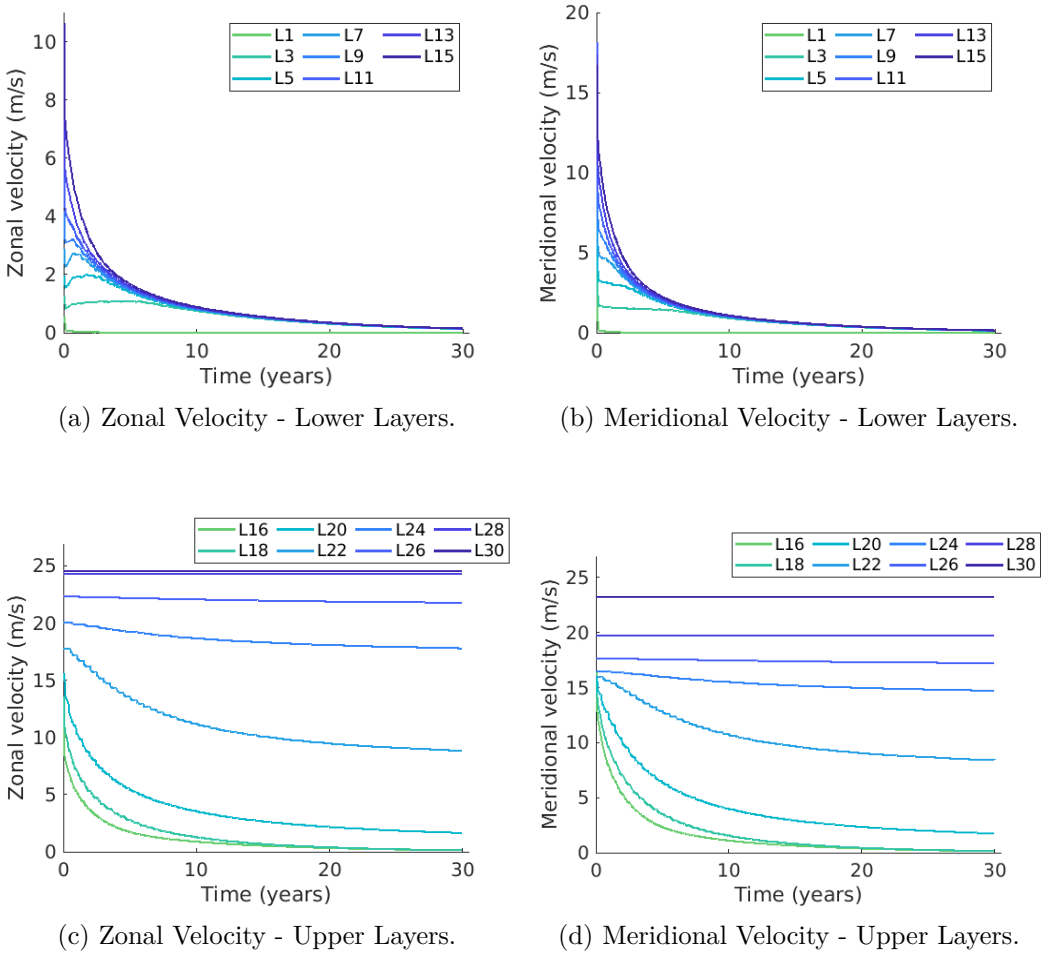

(a) Zonal Velocity - Lower Layers.

(b) Meridional Velocity - Lower Layers.

(c) Zonal Velocity - Upper Layers.

(d) Meridional Velocity - Upper Layers.

FIGURE 4.3: Figures 4.3a and 4.3b displays average zonal and meridional velocity for alternating layers of the lower 15 layers. Figures 4.3c and 4.3d displays average zonal and meridional velocity for alternating layers of the upper 15 layers out of the total 30 layers for the simulations. All figures display a time series of the physics package only 30 year simulation.

4.6 Temperature profile comparisons

A crucial result of the model is the profile of the prognostic variables at the end of the simulation. A profile is the mean average of the variable in question over the entire sphere at each layer, and therefore portrays the difference in the parameter with altitude. In the case of the physics package uncoupled to dynamics, due to the decay of the velocities, only the mean temperature profile at the end of simulation is observed and compared to the simplest physics model, Held–Suarez (Held and Suarez 1994).

The Held–Suarez physics model includes a relaxation of the temperature to a radiative equilibrium value (T_{eq}) and a layer dependent linear damping of the velocities (to model

a planetary boundary layer). The equations of the model are

$$\frac{\partial v}{\partial t} = -k_v(\sigma)v, \tag{4.5}$$

$$\frac{\partial T}{\partial t} = -k_T(\phi,\sigma)[T - T_{eq}(\phi,p)], \tag{4.6}$$

where

- $T_{eq} = max\{200K, [315K - 60Ksin^2\phi - 10Klog(\frac{p}{p_0})cos^2\phi](\frac{p}{p_0})^\kappa\}$
- $k_T = k_a + (k_s - k_a)max(0, \frac{\sigma-\sigma_b}{1-\sigma_b})cos^4\phi$
- ϕ represents a point of latitude
- $k_v = k_f max(0, \frac{\sigma-\sigma_b}{1-\sigma_b})$
- $\sigma_b = 0.7$
- $\sigma = \frac{p}{p_{surf}}$ where p_{surf} = surface pressure
- $k_a = \frac{1}{40}$ day^{-1}
- $k_f = 1$ day^{-1}
- $k_s = \frac{1}{4}$ day^{-1}
- $p_0 = 1000$ mb
- $\kappa = R/c_p$ where R = real gas constant & c_p = specific heat capacity (Held and Suarez 1994).

The temperature tendency of the Held–Suarez model shows that, when not coupled to a dynamical core, the model will eventually relax the temperatures to the T_{eq}. Therefore, the Held–Suarez T_{eq} values, averaged over the entire sphere, were calculated with the pressure, specific heat capacity and real gas constant observed for the physics model driver. The simple physics model was run for 30 years and the profile for temperature was assessed with the Held–Suarez T_{eq} values.

In addition to comparing the simple physics package output to the Held–Suarez model, it is also important to ensure the temperature profile is similar to that of a standard profile of Earth. Therefore, the results were compared with the International Standard Atmosphere (ISA) (*Internantional Standard Atmosphere* 2005), which is a standard model for Earth that provides temperature values over a range of altitudes. Figure 4.4 displays a temperature profile with the simple physics results, the Held–Suarez equilibrium temperature and the ISA values. The Held–Suarez equilibrium temperature is closer to the ISA profile than the simple physics package is. However, due to the simplicity of the Held–Suarez model, it was designed to follow the temperature trend of the atmosphere. While the simple physics has some similarity in terms of shape of the profile, a couple of areas were quite distinct from the ISA profile.

The uncoupled simple dry physics model has temperatures near the surface which are noticeably hotter than those of the ISA and Held–Suarez. The hotter surface and near surface temperatures are attributed to the lack of moisture effects in the dry physics package. When moisture is included in the physics, a couple of effects occur. First, there is a larger radiative cooling on the ground, due to the upward flux of infrared radiation. Secondly, the inclusion of the latent heat flux moderates the surface temperature, producing a cooler surface temperature (Pierrehumbert 2010). Therefore since the ISA results includes the effects of moisture and the Held-Suarez results attempt to mimic the Earth's temperature with moisture, it is expected that the simple physics package surface and near surface temperatures are warmer. In the troposphere the temperature gradient of the simple dry physics model is closer to that of the Held–Suarez profile than that of the ISA. The simple dry physics model's troposphere extends to unrealistically high altitudes: the temperature should start decreasing at around 10 km. This is likely due to the abundance of ozone molecules in the stratosphere. Ozone absorbs ultraviolet light, causing the heating of the stratosphere. The radiation sub-model does not currently include a separate absorption band for UV light in the upper atmosphere, leading to a continuous decrease in temperature in the stratosphere, as seen in Figure 4.4.

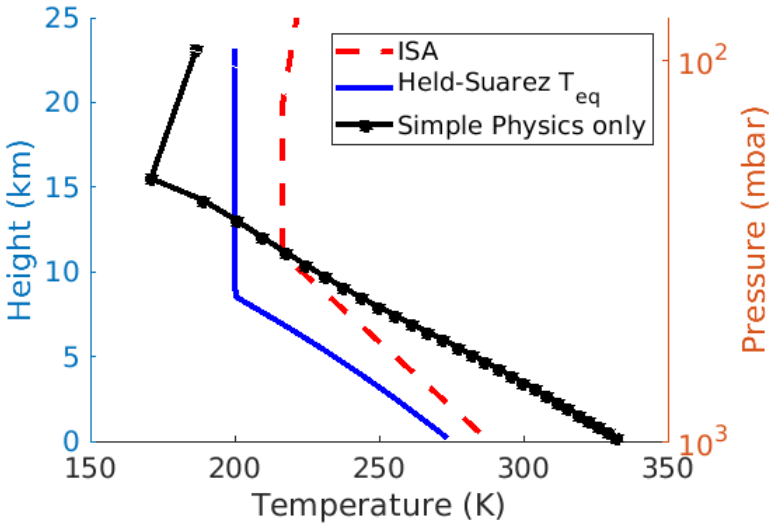

Figure 4.4: Mean average temperature of the simple physics model, after 30 years, in comparison with the ISA and the Held-Suarez equilibrium temperature. Similarity among the ISA and Held-Suarez profiles presents an interesting difference with the simple physics.

Chapter 5

Physics-Dynamics Coupling

As mentioned in the introduction, there are different components that make up a Global Climate Model (GCM) (e.g. atmosphere, ocean, land). In general, the components are created and tested individually and therefore need to be coupled together. The coupling between components occurs at the boundaries and its goal is to depict the interactions and feedbacks between the components. However coupling has its challenges as components often have different spatial grids and time steps.

Components, like the atmosphere and the ocean, separate their processes out into the dynamics and the physics based on the grid resolution chosen and the complexity of the processes. For an explanation behind the dynamics and physics see section 1.2.1 and 1.2.2. There are different types of coupling, as explained in section 1.2.3. However, the split step (i.e. time splitting) method is a typical coupling applied to models. A challenge, regardless of the chosen coupling, involves the time step of both the dynamics and the physics, as models are not constrained to a single time step for both. Moreover guaranteeing that assumptions are not violated by both and being cognisant of the format of the prognostic variables within the dynamics and physics are challenges that modellers must consider when coupling.

One of the major objectives of the simple dry physics package is its ability to be coupled with different dynamical cores. This allows the package to be used in inter-comparison projects and to model different planets. The following section will present an overview of the different possibilities available to couple a dynamical core with the physics package, while also addressing specific challenges that need to be taken into consideration. Furthermore, a comprehensive explanation of how the dynamical core WAVETRISK (Kevlahan and Dubos 2019) is coupled with the simple physics package is explored. Lastly the precision and sensitivity of the physics package will be elaborated upon.

5.1 General coupling to the physics package

To utilize the physics package as a test case, the package needs to be coupled with a dynamical core through the creation of an interface. The interface is the facilitator of the entire program and a design decision of the architect would be whether to integrate

the interface as a part of dynamics or physics compilation. This decision can be highly dependent on the dynamic's architecture of running a test case and whether the physics package code is integrated with the dynamics or if it is a separate entity.

The dynamics and physics must include the same constants and constraints, and as a result the interface will call the physics initialization routines with the constants and constraints set by the dynamics. This includes setting the plugins of the physics. Since the physics package is to be run as a test case, the interface will also need to set the initial conditions for the simulation. Lastly, as the facilitator, the interface will couple the dynamics and physics by calling the dynamics step and the physics step, usually in a split step (see section 1.2.3 for different types of coupling).

A few aspects that need to be taken into account when calling the physics for each time step are: the precision of both the dynamics and the physics, the format of the main prognostic variables stored (i.e. temperature versus potential temperature) and the data structure of the prognostic variables, which is highly dependent on the grid. With this in mind, the interface needs to gather the input required for the physics call, in the right data structure and precision, and upon the return of the tendencies, it will need to update the prognostic variables correctly. Overall the interface is the connector of the dynamics and the physics and can be vastly different among dynamical cores due to its dependence on the dynamical core architecture.

5.2 Physics model precision

The physics model is written in single precision, and therefore only uses 9 digits to represent floating point real values. When coupling with a dynamical core, it is desired that both programs are written in the same precision, but that is not always the case. Some dynamical cores are written in double precision to obtain a better accuracy, while at the cost of memory and time. One option is to convert the dynamic's values from double precision to single precision, before sending them to the physics, but this comes with a loss of accuracy. The second and more desirable options, when coupling the physics model with a dynamical core of double precision, is to compile the physics package with the Fortran flag, `-freal-4-real-8`. This flag converts all real numbers (single precision) in the physics package to real (8) values (double precision). Therefore values do not need to be converted from double to single precision and vice versa and avoids the loss of accuracy that comes with it.

5.3 Coupling WAVETRISK to the simple physics package

To couple the physics package with the adaptive dynamical core WAVETRISK, an interface was created. As mentioned above the interface is the main program, calling all initialization routines, as well as the physics and dynamics through a split step method for each time step. A design decision made when creating the interface, was to format the interface as one of the test cases for WAVETRISK. Beyond the extra considerations of

the physics package itself, this decision allowed for ease of integration and compilation of the entire program, as it treated the physics package as a black box requiring only the compiled physics code. Furthermore other key components that needed to be taken into account during the creation of the interface includes precision differences, the format of prognostic variables and the data structures of the variables.

As mentioned in section 5.2, the physics package is single precision, while WAVETRISK is written in double precision. To avoid conversions to and from both data types, the physics package was compiled with the flag mentioned in section 5.2, allowing the single precision package to work in double precision.

The key input variables required for a physics package time step includes temperature, zonal velocity and meridional velocity at each vertical layer, along with the pressure and geopotential of the vertical columns. Calculating the pressure and geopotential requires the simple integration from the surface upwards for each column and the utilization of the hydrostatic approximation. In comparison, the temperature and velocities require a more in-depth conversion. Wavetrisk saves the mass weighted potential temperature as its prognostic variable. Therefore, when calling the physics, the interface converts the value, at each vertical layer of a column, to potential temperature and then to the required temperature input, in Kelvin, of the physics. Upon return from the physics call, the interface converts the temperature tendencies back to mass weighted potential temperature using the reverse process. Regarding the zonal and meridional velocities, wavetrisk does not store the velocities at the center of the node, instead it stores three velocity edge values. To retrieve the zonal and meridional velocities at the node, interpolation using the three edge values and neighbouring columns' edge values is required. The inverse procedure is also applied when the physics returns the zonal and meridional tendencies for each column.

In general, the data structures storing the prognostic variables of both the dynamics and physics are different. WAVETRISK utilizes a hybrid data structure which is optimal for the grid chosen and for adaptivity and load balancing associated with the use of parallelism (see (Aechtner et al. 2014) for more on the grid architecture and data structure). Conversely, the physics package utilizes a regular data structure to store the values for each column. The regular data structure is a 2D array, with each row representing a different vertical column and each column of the array represents a vertical layer. Upon initialization of the physics package, the number of vertical columns to be sent at each time step is fixed. At each physics step, the package takes in the fixed number of vertical columns, the time step, the simulation day, the fraction of the day and the columns' their prognostic variable values, pressure and geopotential at each vertical layer. A major overhead of the simulation, even in the case of parallelism, is the retrieval and conversion of all vertical columns from the hybrid data structure to the required regular structure for the input of the prognostic variables, as well as the conversion of the output tendencies from the regular to hybrid data data structure.

The use of a 2D data structure constrains the package as it expects the user to call

the physics for all vertical columns at once. However, another major obstacle this structure produces is in the case of parallelism and adaptivity. WAVETRISK utilizes `mpi` and domain decomposition of the columns of the sphere. When adaptivity is used, a major concern is ensuring correct load balancing on each CPU. Therefore, WAVETRISK allows for the re-balancing of the domains on each CPU, to each ensure approximately equal computational loads. The complication arising with the ability of rebalancing is that the physics package saves the soil and surface temperatures internally. To reduce the overhead and overcome the rebalancing obstacle, we have modified the physics step to call the physics for vertical columns individually and the step is completed when the last column's tendency returns from the call. However, to allow for single column transmission, the physics package and WAVETRISK required some fine tuning and additions.

5.3.1 Changes and additions to the physics package and WAVETRISK

The major addition to the physics package is the creation of the single column module. It allows the model to call the physics package for each column individually by providing the soil and surface temperatures to the dynamics. This module contains a wrapper subroutine that the interface calls, including all required inputs for the original physics call plus the added soil and surface temperatures. Once the wrapper subroutine is called, it updates the soil and surface temperatures for the column and calls the original physics routine. The subroutine outputs the original tendencies and the new updated soil and surface temperatures for the interface to save. The module also contains a subroutine that allows for the change in latitude and longitude required when sending a different column at each physics call. A major change to the physics package is the input of the number of desired soil layers when initializing the parameters of the grid in the package. Originally this was fixed to 10, but a variable number of layers is desired to test the importance of the soil model.

The only major change to WAVETRISK was in the grid initialization. To send single columns to the physics with the possibility of rebalancing, WAVETRISK must save the soil temperatures and surface temperature of each column. The vertical layers were therefore extended, below the surface, employing negative and zero indexes for each vertical column to represent the soil layers ($k < 0$) and surface ($k = 0$) temperature respectively. The interface facilitates this by setting the number of soil layers, before all grids are initialized. The only drawback of extending the grid is that all prognostic variables' data structures needs to be extended, even though only the mass-weighted potential temperature negative indexes are used to save the soil and surface values. Therefore, there is additional unnecessary memory overhead. In future, it is recommended that only the required variable's data structure be extended, but this will require a more extensive update, not only to the architecture of the grid, but also to the architecture of the calls for the dynamics step.

Another design decision, was how the temperatures were stored. It was decided that the soil and surface temperatures would be stored in the mass-weighted potential temperatures data structure in the negative and 0 indexes respectively. More importantly,

the temperatures would not be converted to mass-weighted potential temperature, but would be retained as temperature (units of Kelvin). This decision was made to avoid the extra overhead that comes with the conversion, as the values are not used by the dynamics.

5.3.2 The workflow of the interface and physics call

To illustrate the sequence of steps taken by the interface figure 5.1 displays the workflow of the interface written to couple WAVETRISK to the physics package. Furthermore, to illustrate the coupling challenges mentioned above, figure 5.2 displays a flowchart of the algorithm used by the interface and required for the a single physics (split) step. The steps in black are the extra steps required to change prognostic variables to the required form, for example mass-weighted potential temperature to temperature or vice versa. The yellow step represents the call to the wrapper subroutine in the single column module added to physics package to allow the architecture of sending individual columns.

5.4 Sensitivity of the physics package

The sensitivity of the physics package was observed after the initial coupling of WAVETRISK to the physics package. The first test of this coupling was to compare the results for a physics only run by WAVETRISK coupled to the physics and the dummy driver (explained in the section 4.1). A difference of near zero was expected, but errors up to an order of (10^{-2}) were observed.

Therefore, additional tests similar to unit testing were used to find the errors and observed sensitivities for certain inputs in the physics package. The tests required us to strip down the interface to an almost identical copy of the driver and test the two facilitators for a single coordinate. The two facilitators stored the same prognostic variables and used the exact same initial conditions. Upon testing the two facilitators, in the physics only case, the initial instance of sensitivity arose from a rounding difference in the specified floating-point gas constant, resulting in a variation of (10^{-6}). The error observed after ten years in the output was on the magnitude of (10^{-6}), (10^{-3}) and (10^{-3}) for the temperature, zonal and meridional velocities respectively.

Furthermore, a similar observation occurred when testing the facilitators for a different set of coordinates, as the fraction of the day for each time step was calculated slightly differently. The fraction of the day for each facilitator were calculated respectively using,

$$\text{fraction of day} = \frac{\text{simulation time}}{86400} - (\text{number of simulation integer days}) \tag{5.1}$$

$$\text{fraction of day} = dt * \frac{\text{number of steps done in the day}}{86400}, \tag{5.2}$$

where 86 400 represents the number of seconds in a day and dt is the whole number time steps (i.e. 1 200 seconds). The difference between the outputted fraction of the day was due to the cancellation error of the subtraction in equation 5.1 and was of the

order (10^{-8}). The error observed in the output after a ten-year simulation was of the order (10^{-5}), (10^{-2}) and (10^{-2}) for the temperature, zonal and meridional velocities respectively. The fraction of the day is a sensitive input to the physics package because it is used to calculate the elapsed number of days, the zenith angle and the daylight fraction used in the physics radiation model.

Finally, a crude sensitivity analysis was conducted, using a 1 000 column uncoupled simulation, by introducing the small perturbation of $(10^{-6}K)$ to the initial temperature conditions in the atmosphere, while all other variables remained unchanged. After two simulation years, an average error of (10^{-8}) was observed between the output temperature values. More interestingly, for both the zonal and meridional velocity the average error produced was (10^{-5}). Figure 5.3 displays the forward error of the three outputs, with a running average of 30 days.

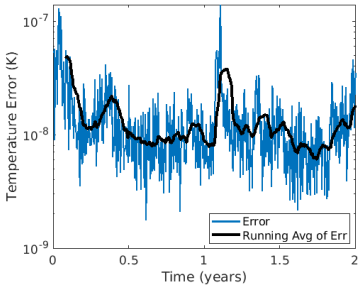

(a) Temperature Error

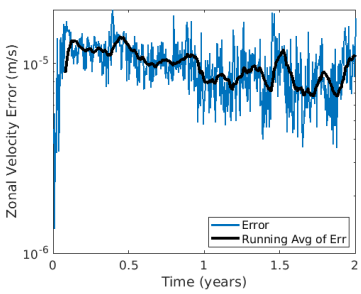

(b) Zonal Error

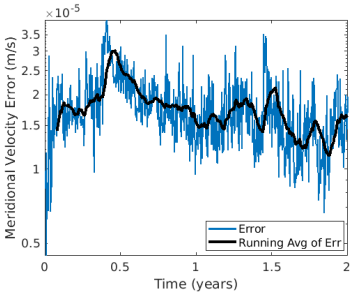

(c) Meridional Error

FIGURE 5.3: Forward Errors produced for the 3 prognostic variables when initial temperature condition was perturbed by (10^{-6}) K.

We concluded that the physics package may be sensitive to small perturbations, especially rounding errors that are produced in input parameters beyond the initial conditions. Based on these findings it is suggested that a more thorough investigation into the physics package is explored through the introduction of perturbations to different input variables in the physics model. This will allow for a more detailed explanation into each individual input parameter and its strength and relevance on the potential disparity of the output produced.

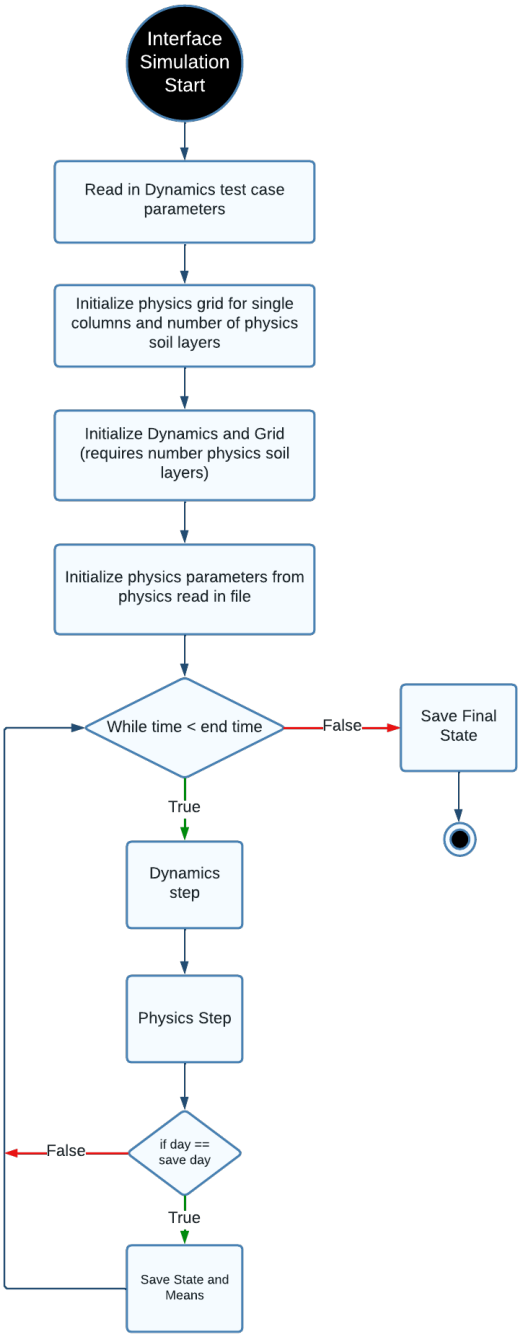

FIGURE 5.1: A flow chart of the interface coupling the physics and dynamics. The workflow shows the the steps of the simulation until the end.

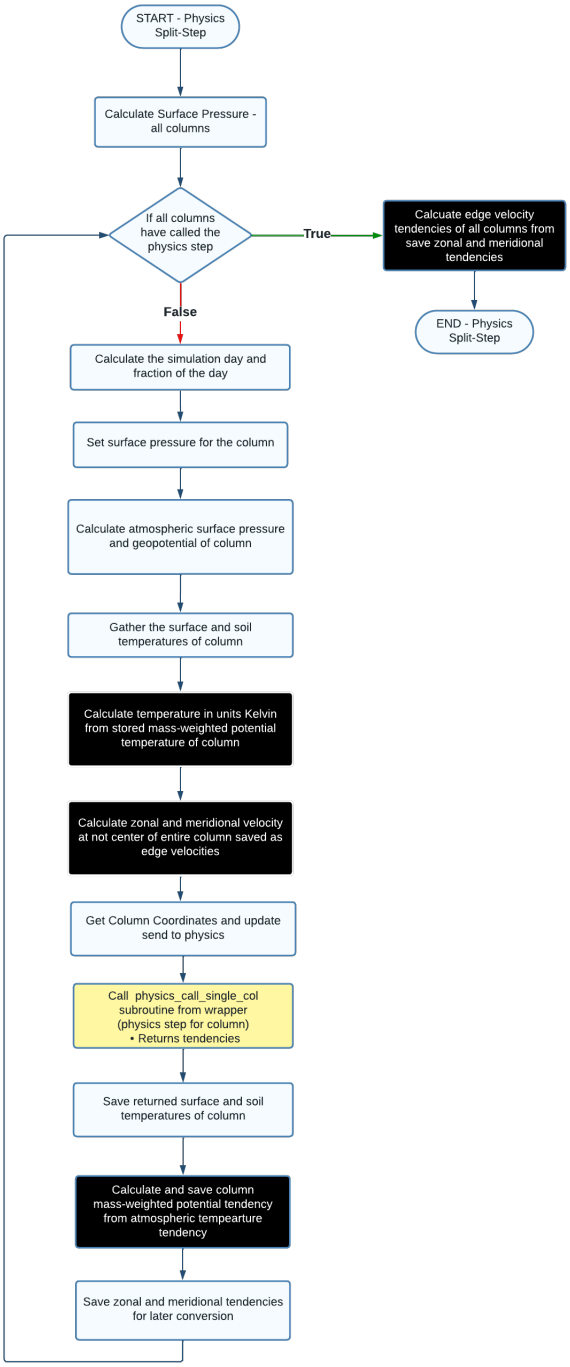

Figure 5.2: A flow chart of the physics step. Steps in black contain overhead concerning the conversion of the prognostic variables from one type to another (i.e. mass-weighted potential temperature to temperature (K)). The yellow process represents the physics call of the added single column module of the physics.

Chapter 6

Coupling Results

A central goal of the physics package is to provide a simple dry physics test case for both the adaptive and non-adaptive cases. The non-adaptive case is important, as it defines the climatology of the physics package and provides a benchmark for comparison when testing the adaptive case. The objective of this section is to present the results from running the physics package coupled with WAVETRISK running in the non-adaptive mode. The results focus on the effects of the soil model, the time convergence of the coupled model, the grid convergence of the coupling, the performance of the physics model and a temperature profile comparison to the International Standard Atmosphere (ISA) model and the physics only simulation. In summary, we aim to define the climatology of the simple dry physics package.

The initial conditions and parameters used for the physics are the same as the ones used in the uncoupled runs (section 4.1). These initial conditions are relevant to Earth, with the same planet constants as those in table 4.1. However most runs do not include seasons (i.e. obliquity of 0°), explained in section 6.1. The top interface pressure and surface pressure, found in table 4.2 are the same for all simulations. Furthermore, the initial temperature, found in table 4.2 and the velocity initializations, found in section 4.3, are used for all simulations. Further justification behind these conditions can be found in section 4.1.

There are 30 vertical atmosphere layers, where layer 1 represents the layer above the surface and layer 30 corresponds to the uppermost atmospheric layer, and 0 up to 10 soil levels. The horizontal resolutions, set by WAVETRISK, are $4°, 2°, 1°, 0.5°$ resolution ($\sim$ 480 km, 240 km, 120 km, 60 km).

In current operational climate models the number of vertical atmospheric layers is usually between 20 and 100, with a higher value to enable higher "tops" of the atmosphere (Chen et al. 2021). The atmospheric horizontal resolution of these models can range from $\sim$ 200 km to 50 km, with high resolution models approaching a horizontal resolution as small as 10 km (Chen et al. 2021). In contrast, in the 1990s approximately 10–15 vertical atmospheric layers and a $\sim$ 500 km horizontal resolution were typical (Le Treut et al. 2007). Therefore, the chosen 30 vertical layers and 480 km to 60 km horizontal resolution for the simulations are well within the range used in current models,

but also do require excessive CPU time for a simulation of five years using the available computational power (even on a non-adaptive grid).

6.1 Seasonality

Initial coupled simulations with seasons (i.e. obliquity of 23°), displayed an unexpected temperature trend over the sphere. Since the physics model parameters are consistent with those of Earth and the atmospheric height extends only to the troposphere and lower stratosphere, we expected that the temperature should be warmest at the equator and coolest at the poles at most vertical levels. However, as seen in figure 6.1, at day 136 of the fifth year, the southern and northern hemispheres display a warmer and cooler temperature respectively. In contrast at day 304 of the fifth year an opposite trend occurs with the northern hemisphere displaying the warmer temperatures. These 2D projections of the sphere are at a pressure height, within the troposphere, of 850 hPa ($\sim$ 1.5 km, $\sim$ layer 5). This trend is more typical of the stratosphere of Earth rather than the troposphere.

The incorrect representation of the temperature on the meridian plane could be a result of the simplicity of the radiation model, or the incorrect tuning of the model. On Earth, with a tilt of $\sim 23.5°$, it is expected that, at the top of the atmosphere, the solar insolation is weakest at the pole in the winter hemisphere and largest at the pole in the summer hemisphere compared to the equator. Therefore, if the atmosphere is transparent to solar radiation, then warmer and cooler poles are observed (Hourdin 1992). However, if the atmosphere significantly absorbs and reflects solar radiation, then the surface cooling of the poles will be much greater, for the same amount of insolation, than at the equator (Hourdin 1992). Therefore, the fact that the radiation model neglects the scattering of solar radiation could be the main reason for the observed meridian temperature trend. Another factor could be that the physics model is set to weakly absorb solar radiation, through the transmission function and may require tuning. More accurate results could be obtained by adding a third radiation absorption band in the UV for the upper atmosphere.

Conversely, simulations of WAVETRISK coupled to the physics package with zero planet obliquity (i.e. no seasons) displayed the expected trend of the troposphere. Figure‘6.2 presents the 2D projections of the sphere at a pressure of 850 hPa at the exact same time periods as the previous figure containing seasons. At both day 136 and 304, of the fifth year, the equator was the warmest and the poles were the coolest. Therefore, the remaining simulations, which test the effects of the soil, time convergence, grid convergence and performance of the package coupling to WAVETRISK will use zero obliquity (no seasons).

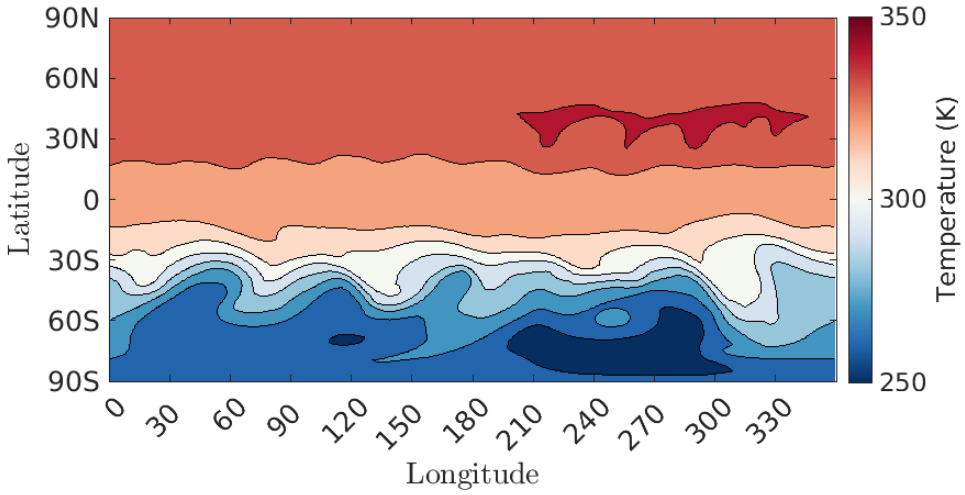

(a) Day 1596 Projection.

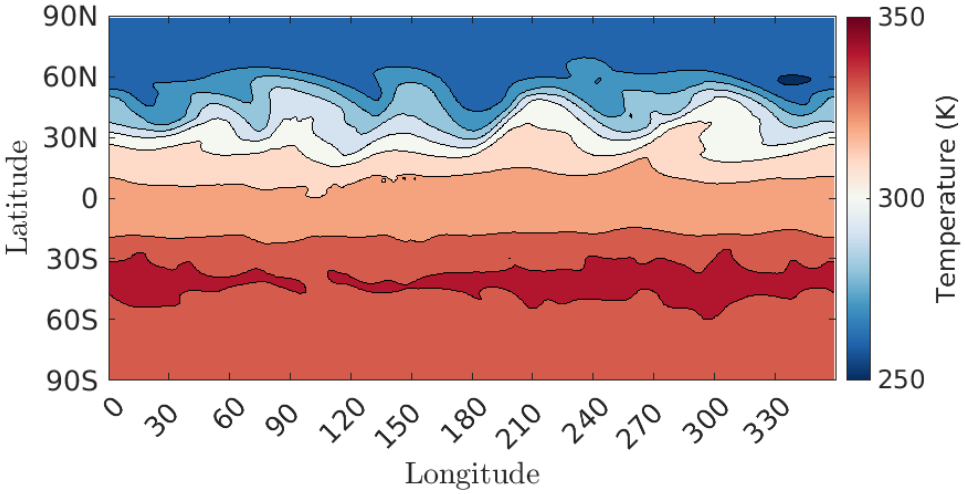

(b) Day 1764 Projection.

Figure 6.1: A 2D projection of a five-year wavetrisk with simple physics simulation, with seasons included. The projection displays the temperature across the sphere at a pressure level of 850 hPa ($\sim$ 1.5 km, $\sim$ layer 5). Figure 6.1a displays the projection at day 1596 (i.e. day 136 of the fifth year). The temperature trend displayed a warmer norther hemisphere and cooler southern hemisphere. Figure 6.1b displays the projection at day 1764 (i.e. day 304 of the fifth year). The temperature trend displayed a warmer southern hemisphere and cooler northern hemisphere.

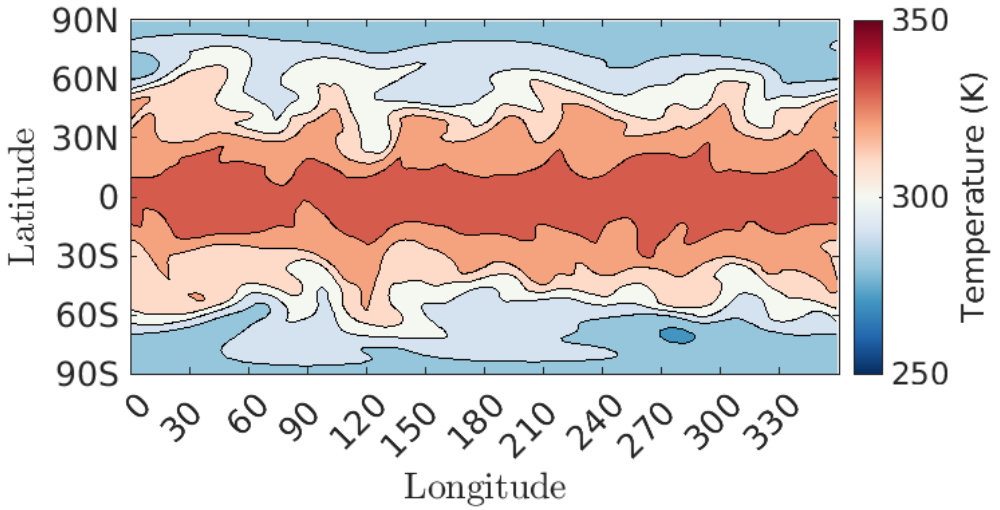

(a) Day 1596 Projection.

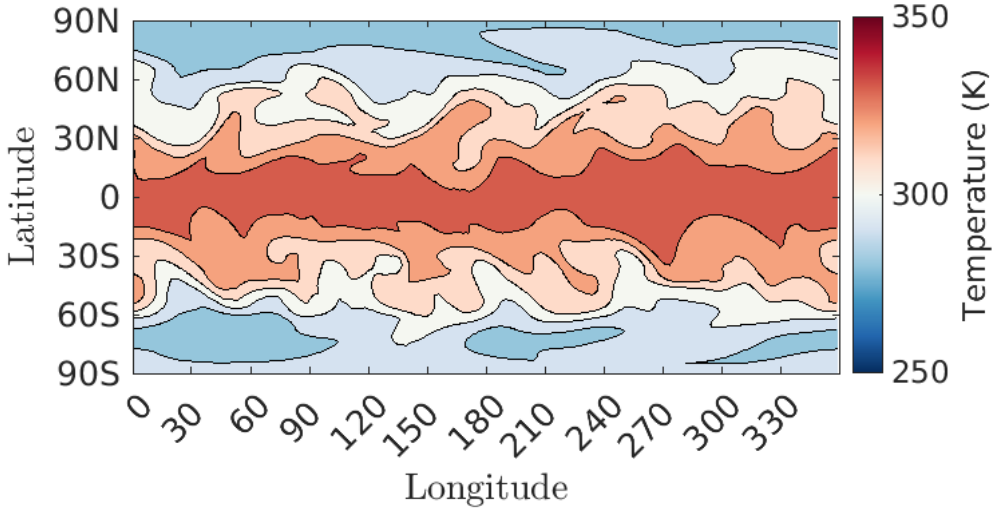

(b) Day 1764 Projection.

FIGURE 6.2: A 2D projection of a five year WAVETRISK with simple physics simulation, without seasons. The projection displays the temperature across the sphere at a pressure level of 850 hPa ($\sim$ 1.5 km, $\sim$ layer 5). Figure 6.2a displays the projection at day 1596 (i.e. day 136 of the fifth year). Figure 6.2b displays the projection at day 1764 (i.e. day 304 of the fifth year). The temperature trend displayed at the different times in a year, showed a warmer equator and cooler poles.

6.2 Effects of the soil model

The inclusion of a soil model in idealized Atmospheric Global Climate Model (AGCM) physics is uncommon. Therefore, the following section will explore the impact on the

temperature profiles when WAVETRISK couples with the physics including no soil model, as well as including a soil model with 4 soil layers, 7 soil layers and 10 soil layers. Including a soil model, allows for the retention and release of heat at different time scales. Refer to Appendix B.1 for information on the time periods associated with varying numbers of soil layers and their estimated depths. All temperature profiles contain the temperature averaged over the entire sphere and averaged over 2 years, with the same setup explained at the beginning of the chapter (6).

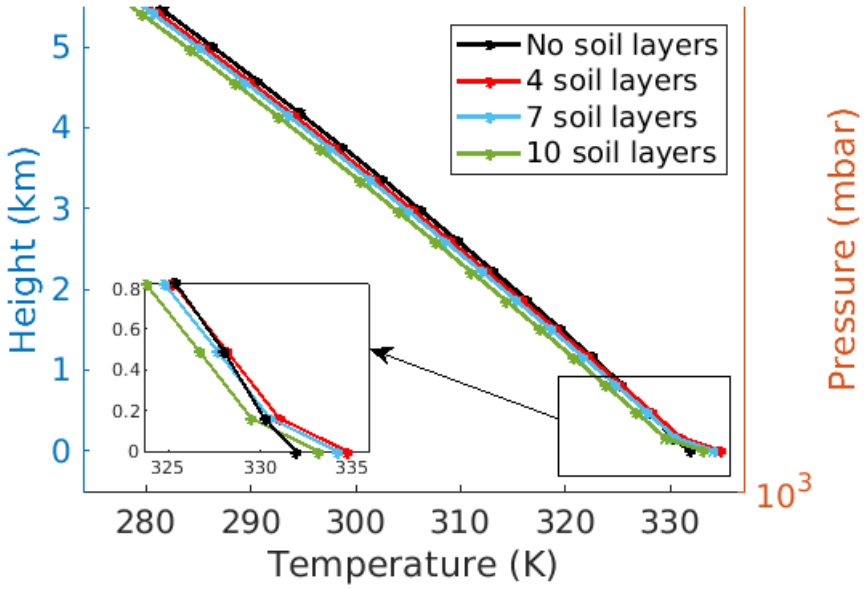

FIGURE 6.3: Temperature profile comparing simulations of WAVETRISK coupled to the physics package containing no soil layers, 4 soil layers, 7 soil layers and 10 soil layers. These are the results of 5 km in the lower atmosphere and the trend of an increase in soil layers introducing a cooler temperature profile is observed above the fourth layer in the lower atmosphere.

Figure 6.3 displays the temperature profiles in the first 5 km of the atmosphere. The outstanding feature is the trend in the surface layer and the first three atmospheric layers. The four layer soil case produces the warmest temperatures in the lowest four layers of the atmosphere. In the surface layer, there is no trend for surface layer temperature, but the 10 soil layer temperature case produces the coolest temperatures in the lowest three atmosphere layers. Overall, above the fourth atmospheric layer the figure shows a slight decreasing temperature trend with increasing numbers of soil layers.

The mid atmosphere temperature profile (Figure 6.4), displays the profiles 5–10 km into the atmosphere. A similar trend as the lower atmosphere is observed with the coolest profile attributing to the 10 soil layers and the warmest profile to the simulation without

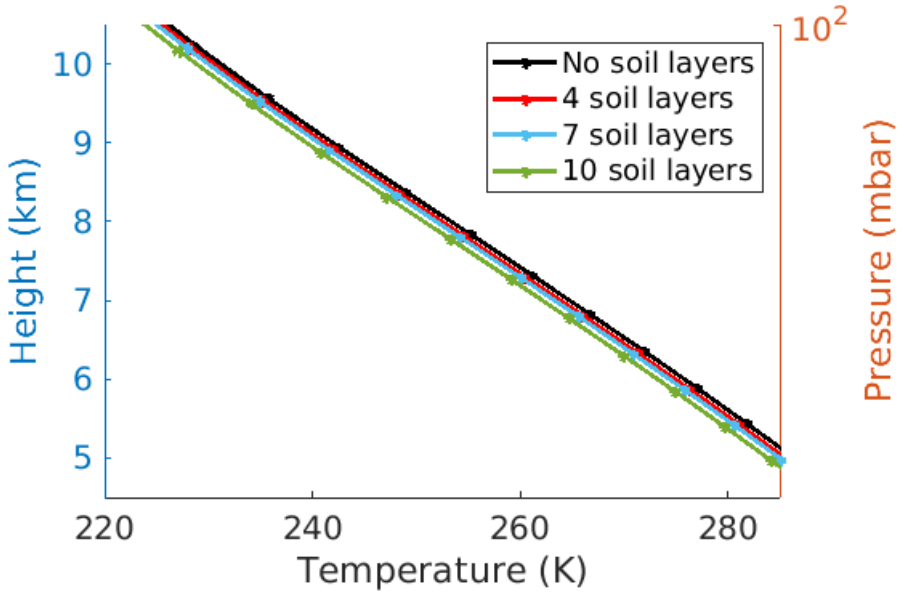

FIGURE 6.4: Temperature profile comparing simulations of WAVETRISK coupled to the physics package containing no soil layers, 4 soil layers, 7 soil layers and 10 soil layers. These are the results from 5–10 km in the atmosphere and the trend of an increase in soil layers introducing a cooler temperature profile is observed.

the soil model. However, it appears for altitudes greater than 10 km, the difference between the 4 soil layers case and the no soil profile diminishes.

Lastly, the upper atmospheric profile (Figure 6.5) follows a similar trend as the lower altitudes. Simulations with more soil layers produced cooler temperature profiles. However, in the top layer of the atmosphere all profiles appear to converge to a similar temperature. Since we use an equi-pressure vertical coordinate, the granularity in terms of height, between the last two layers in the upper atmosphere is low (2 km difference). Therefore, the trend here is unknown and any temperature convergence with altitude is poorly defined in the upper atmosphere.

Overall, more soil levels are associated with a cooler temperature profile for most of the atmosphere. This could be due to the fact that with more soil layers, there are increasingly longer time scales available to store and release heat. In contrast with no soil layers, the other terms in the boundary energy balance need to compensate. The average difference between the 10 soil layer profile and the no soil layer profile was ~ 1.7 K, with a difference at the surface of approximately 1.2 K. The largest difference occurred among the middle layers at a height of approximately 3 km. In comparison, the average difference between the 4 soil layer profile and the no soil profile was ~ 0.38 K and the average difference between the 7 soil layer profile and the no soil layer profile

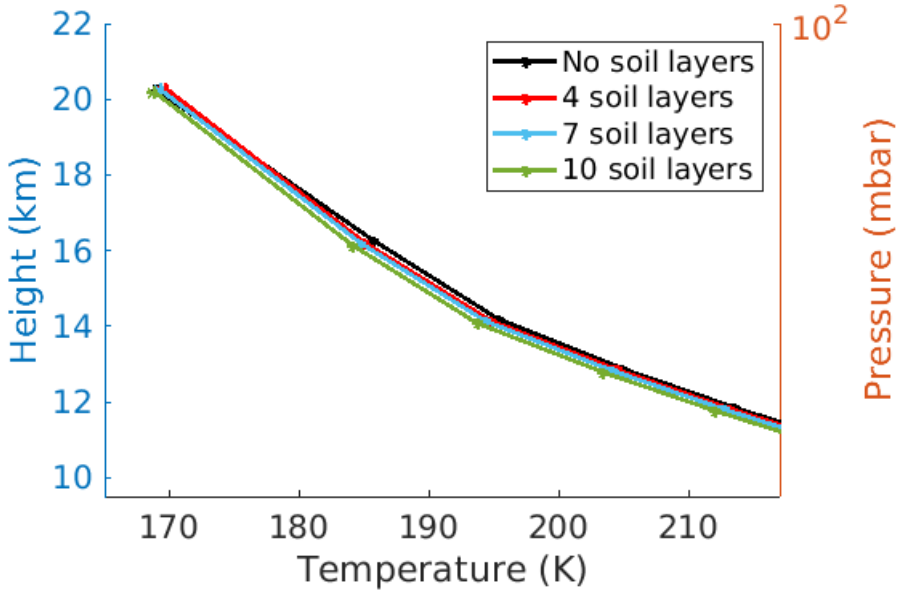

FIGURE 6.5: Temperature profile comparing simulations of WAVETRISK coupled to the physics package containing no soil layers, 4 soil layers, 7 soil layers and 10 soil layers. These are the results from 10–20 km in the atmosphere and the trend of an increase in soil layers introducing a cooler temperature profile is observed, except in the very top layer.

was ~ 0.81 K. See Table B.2, B.3 and B.4, in the Appendix, for the differences at each atmospheric layer.

A distinctive feature of the temperature profile is at the surface where, unlike the trend for the rest of the atmosphere, the coolest profile is in fact the no soil simulation and the warmer profiles are the 4, 7 and 10 soil simulations. These values are the mean temperatures over all time steps for 2 years. This ensures the different times scales and the lag in the release of heat from more soil layers are not skewing the results. Table 6.1 displays the mean surface temperatures over two years (year 3–5) for simulations with no soil layers, 4, 7 and 10 soil layers. The mean temperatures indicate the 4 soil and no soil simulations having the warmest and coolest mean surface temperatures respectively. The results at the surface could be an indication of an inaccuracy in the boundary conditions for simulations with no soil model, but also that the no soil boundary conditions are quantitatively different. If the no soil profile is disregarded, a consistent trend of an increase in temperature with a decrease in height, in the lower atmosphere, is observed. However further validation necessitates a broader range of profiles featuring varying quantities of soil layers.

Overall with only 4 profiles, we can not conclude if the model is convergent, with respect to the number of soil layers. However for most of the atmosphere, except near

Number of Soil Layers	None	4	7	10
Mean Surface Temperature	331.94 K	334.75 K	334.23 K	333.13 K

Table 6.1: The mean surface temperature for all time steps across two years for simulations with no soil layers, 4, 7 and 10 soil layers. The mean temperatures display the trend of the warmest surface temperature attributed to the 4 soil layer simulation and the coolest to the no soil layer simulation.

the surface and top, the observed trend of more soil layers producing a cooler profile is consistent with convergence. It is recommended that a more comprehensive study is conducted, including numerous profiles from simulations with varying amounts of soil layers, to validate the convergence. Furthermore the additional profiles can provide further affirmation of the convergence at the surface and the potential inaccuracy of the no soil simulation boundary conditions.

To understand how the temperature of the soil layers themselves vary with depth, figure 6.6 displays the results of a five-year simulation with 10 soil layers. While the first three soil layers reach an equilibrium temperature, the temperatures of the next four lower soil layers are still changing. The temperature of the bottom soil layer appears to not have increased, while layers 8 and 9 are still increasing in temperature after the five year simulation. Unsurprisingly, soil temperature decreases with depth and the deeper layers respond to surface heating on increasingly longer time scales. As explained in section 3.4.4, the soil layer responses are a function of time. More layers allow for more, longer, time scales of energy retention and release. Only temperature variations with longer periods will penetrate the deeper layers. Therefore, the maximum temperature of a layer decreases as the layer get deeper, as seen in the time series. Furthermore, for each time scale of a wave (e.g. diurnal, annual), there is a phase delay with respect to depth, which is longer for larger time scales (Arya 1988). With deeper layers displaying the effects of diffusivity at longer time scales, they also experience a delay in the time, with respect to the surface penetration, for the waves with longer periods to penetrate. This is portrayed in the time series by the delay in increase in temperature with depth. Lastly another expected trend, that is portrayed in the time series, is the lag in time of the occurrence of the maximum temperature of each layer (Arya 1988).

6.3 Time convergence

The goal of the time convergence experiment is to observe and classify the trend of the prognostic variables at each atmospheric layer. It is important that a reasonably well-defined statistical equilibrium climate state is reached and that the model does not diverge (i.e. it is stable). The time convergence results are the outputs of a five year simulation, using 10 soil layers, 30 atmosphere layers and 2° degree (240 km) horizontal resolution. The prognostic variables are the temperature and the zonal and meridional velocity. To help observe the trend, the time convergence results for the velocities are

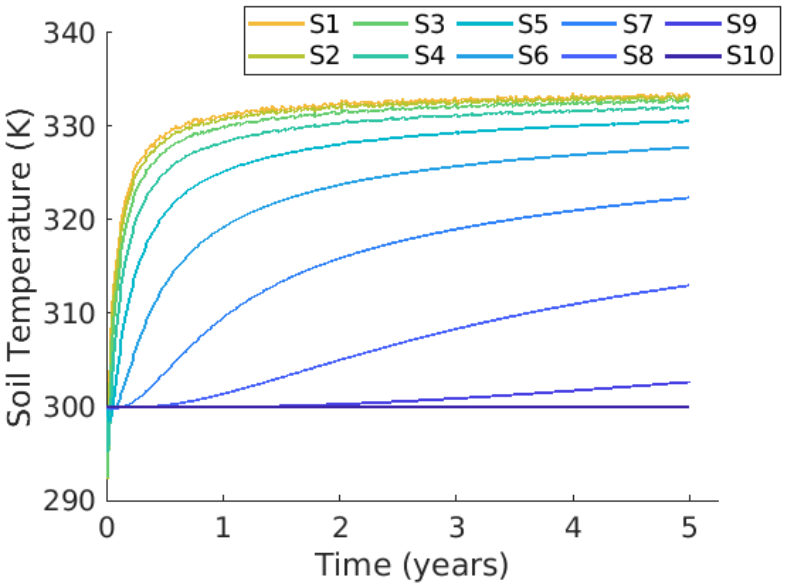

FIGURE 6.6: The time series of the soil temperature averaged over the sphere for a five year simulation with a 2° horizontal resolution. 'Sk' labels soil layer $k = 1, \ldots, 10$.

presented as the zonal and meridional kinetic energy (KE) per unit volume, including density in their calculations. To check the steady states of each prognostic variable, a standard deviation around the mean is computed. If it is within five percent of the mean, the prognostic variable is deemed to be at a steady state. The value of five percent was chosen (rather than a smaller value) because it is expected that climate variables are subject to intrinsic small scale variability (i.e. turbulence).

Figure 6.7 displays the time series of the temperature averaged over the sphere for every third atmospheric vertical layer. The figure also displays the surface temperature in black. The temperature appears to reach a statistical equilibrium within the first two years for all layers. After three years all standard deviations are within 0.2% of the mean. Therefore, we conclude that that the temperature reached a steady state within the first three years of the simulation. It is important to note, however, that after only two years all layers were already within the defined 5% tolerance, with the largest deviation being 2.3%. However, for three years and later most layers (layer 27 and lower) had a deviation of only about 10^{-2}.

Furthermore, as expected, the surface layer has the hottest equilibrium of all the atmospheric layers, followed by the first atmospheric layer near the surface. Higher layers have lower temperatures, as the layers are further up in the atmosphere, leaving the top layer with the coldest equilibrium. In comparison to the uncoupled temperature time series (Figure A.1 in Appendix A) with no seasons, the largest differences in the equilibrium temperature are found in the top two atmospheric layers with the coupled equilibrium being ~ 15.5 K cooler and ~ 15 K warmer for the uppermost and subsequent

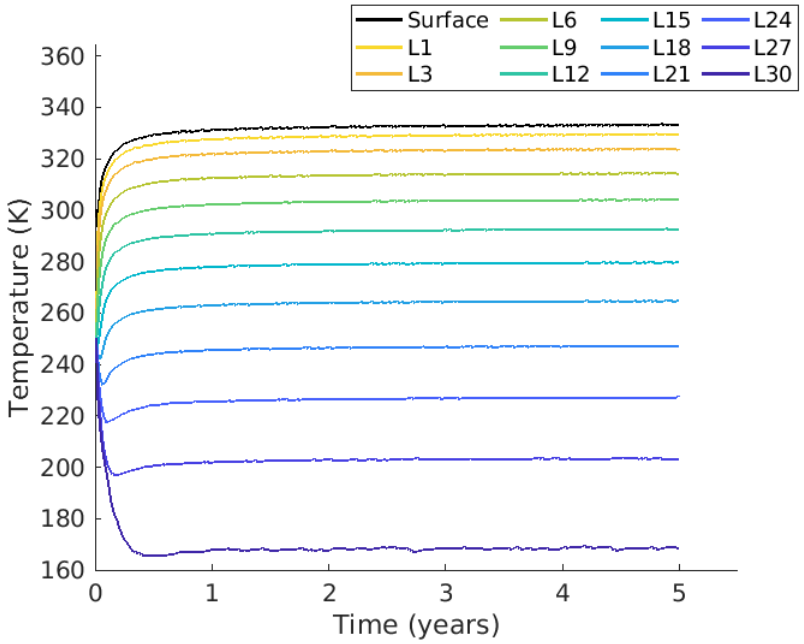

FIGURE 6.7: The time series of the temperature averaged over the sphere for every third atmospheric vertical layer of a five year simulation with a 2° horizontal resolution. 'Lk' symbolizes layer k of the 30 atmospheric vertical layers. The results are from a simulation including the 10-layer soil model and the temperature of each of the layers reach a statistical equilibrium.

layer respectively. All other layers seem to be visually within range of one another (see section 6.4 for a comparison into the vertical equilibrium trend). The standard deviations for all layers are smaller in the uncoupled simulations after 2 years and the coupled simulation equilibrium states appear to have more fluctuations, especially in the top atmospheric layer. This is due to the expected small variability in the coupling with the dynamics.

Figure 6.8 shows the zonal KE per unit volume for every third vertical layer averaged over the sphere. The figure displays a one year running average of the zonal KE to help observe the trend and reduce the noise. The zonal KE appears to include a long time scale fluctuation in the middle layers, although it has reached a statistical equilibrium after approximately two to three years. After examining the standard deviation after three years, the largest deviation from the mean, in layer 30, is just 1.9%. Meanwhile, the majority of layers, below layer 27, have deviations of less than 0.8% of the mean. Therefore,the zonal KE is considered to have reached a statistically steady state after three years. See appendix section B.4 for the ten year time series.

The time series indicates that the lowest atmospheric layer has the least zonal KE, which is due to the damping of the velocity near the surface. The KE increases as the

layers move further into the atmosphere until layer 21. In the subsequent layers the zonal KE begins to decreases as the layers continue to increase in height. This is due to the decrease in the mass of each layer with altitude.

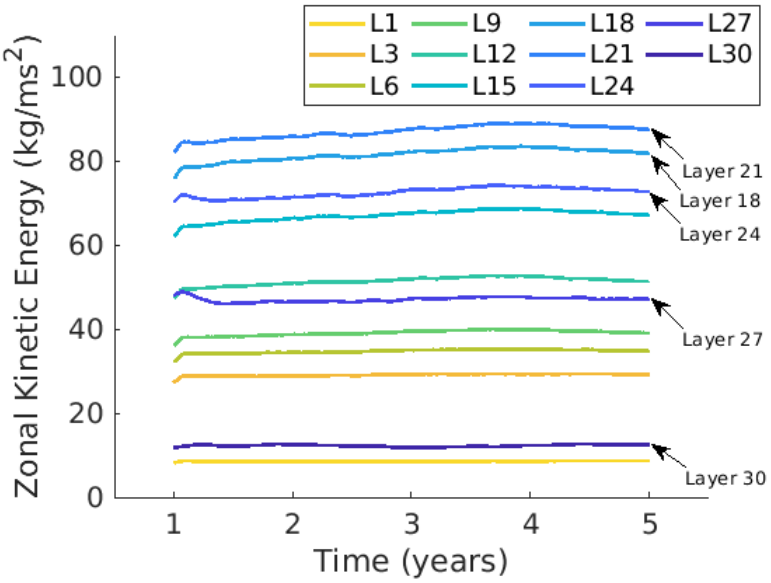

Figure 6.8: Five year time series with a 1 year running average of the zonal KE for every third atmospheric vertical layer. 'Lk' represents layer k out of 30. The simulation has a 2° horizontal resolution. The time series results reach a statistical steady state and are from the simulation including the soil model with 10 layers.

Similar to the zonal time series, the meridional KE per unit volume times series (Figure 6.9), containing every third vertical layer, displays a one year running average in order to smooth out the results and observe the trend. The meridional KE has extended fluctuations, beyond five years. The the middle layers appear to have reached statistical equilibrium within approximately three years. The standard deviations of the layers below the top two layers deviate by at most 1.6% of the mean meridional KE, with layer 29 and 30 showing deviations within 3.7% of the mean. Therefore, the meridional KE is also considered to have reached a stastical steady state within three years. See appendix section B.4 for the ten year time series.

The time series data reveals that from the initial atmospheric layer, the meridional kinetic energy (KE) starts to rise with altitude. Interestingly there is a small decrease in KE after layer 3 until layer 9, however the following layers continue to increase until layer 18. A more comprehensible picture of this trend can be seen in the vertical climatology (figure 7.6) in chapter 7. Subsequent layers, after layer 18, decrease in KE with height, due to the decrease in mass further in the atmosphere. In contrast to the zonal case, the lowest meridional KE is found in the top atmospheric layer, L30.

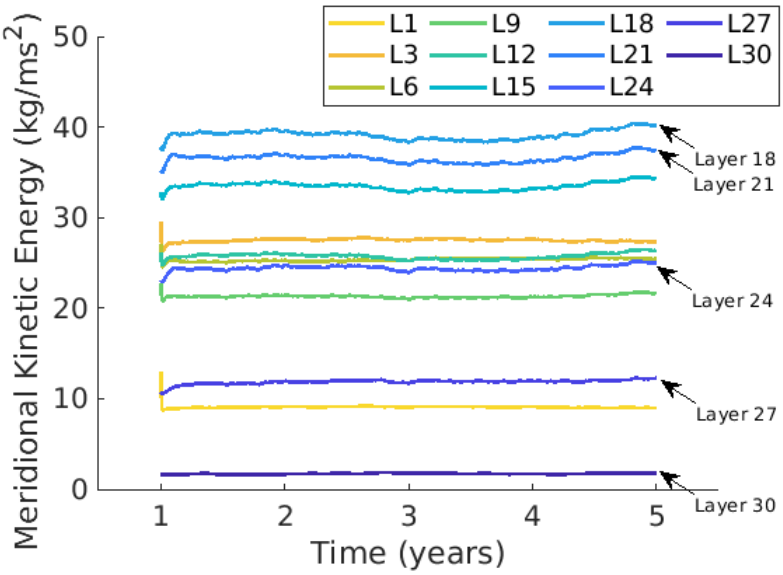

FIGURE 6.9: Five year time series with a one year running average of the meridional KE for every third atmospheric vertical layer. 'Lk' represents layer k out of the total 30 layers. The simulation has a 2° horizontal resolution and 10 soil layers. The results indicate the meridional KE reaches a statistical steady state by 3 years.

Overall the prognostic variables for the coupled physics package simulations reach a statistical steady state within 3 years, therefore deeming the model stable. The trend of the temperature equilibrium revealed a decrease in temperature with height, while the equilibrium of the KEs initially increased with height, but decreased due to the decrease in mass at lower pressures.

6.4 Temperature profile characterization and comparison

The temperature profile (Figure 6.10) displays profiles of the ISA, the Held–Suarez equilibrium temperature, the WAVETRISK coupled with the package results and the uncoupled physics package results. The coupled and uncoupled simulations were run for five years with 10 soil layers, 30 vertical layers and a horizontal resolution of 2°. The objective of the profile comparison is to characterize and highlight any differences among the profiles.

Overall, both the coupled and uncoupled runs have temperature profiles that are hotter near the surface and cooler near the top of the atmosphere compared to both the ISA and Held-Suarez T_{eq} profiles. The uncoupled surface temperature is greater than the coupled surface temperature by ~ 6 K. The difference between the coupled and uncoupled profiles diminishes with height until ~ 2 km, where they intersect. At higher altitudes the coupled simulation is increasingly warmer. The upper atmosphere profile of the coupled simulation appears to be slightly more realistic, with a decreased cooling

rate above the troposphere. Overall, the coupling of the physics with the dynamics produces a warmer mid to upper atmosphere and a slightly cooler lower atmosphere. For exact differences at each atmospheric layer see Table B.5.

In general, for Earth, the temperature in the stratosphere (around 11 km) starts to increase due to UV radiation absorption, as seen in the ISA profile. This is not the case in profiles with the physics package as the physics package lacks a band characteristic to the frequency of UV radiation. Furthermore, in comparison to the ISA profile, the temperature profiles including the simple physics package are much warmer near the surface. Of course, the most important difference is likely the neglect of moisture in the simple dry physics model (see section 4.6 for the full explanation).

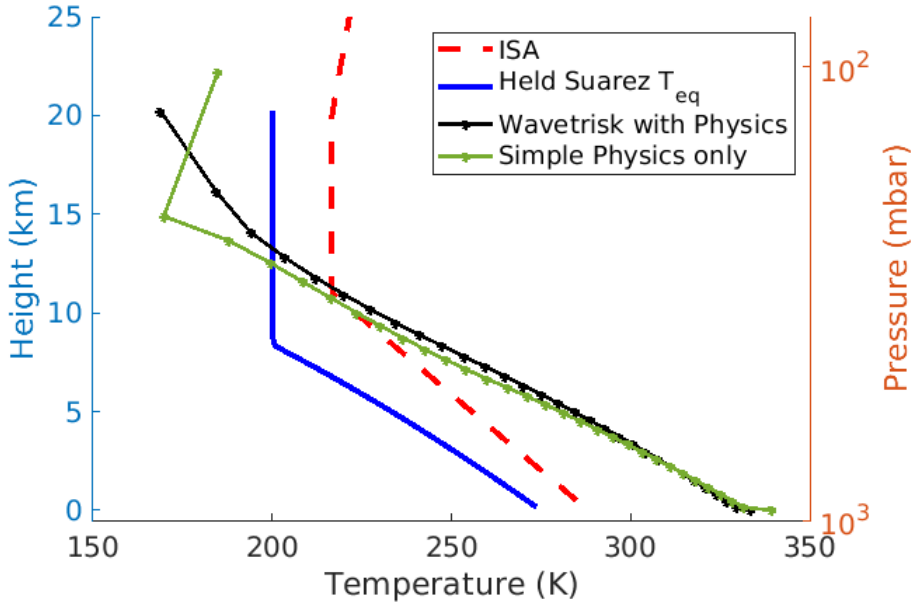

Figure 6.10: Temperature profile comparing wavetrisk coupled to the physics package with 10 soil layers with the ISA profile, the physics only profile and the Held-Suarez temperature equilibrium (Teq). In comparison to the uncoupled profile, the coupling with the dynamics produces a slightly warmer mid to upper atmosphere and a slightly cooler lower atmosphere.

6.4.1 Zonal profile

To better characterize the temperature profile, it is helpful to observe the zonal trends, as various regions exhibit distinct temperature characteristics. Figure 6.11 displays the profiles of the polar, mid and the equatorial latitudes from a five year simulation with 10 soil layers. The polar, mid and equatorial latitudes represents all latitudes between $0° - 23.5°$, $23.5° - 66.5°$ and $66.5° - 90°$ respectively.

As expected, especially in the troposphere, the polar latitudes have a cooler temperature profile than both the mid and equatorial latitudes. For most of the profile, the mid-latitudes are cooler than the equatorial profiles. However, the equatorial profile displays a steeper slope than the mid-latitudes profile, in so much at approximately 12 km the profiles intersect and the two layers below the top atmospheric layer have a greater mid-latitude temperature than equatorial temperature. Due to the lack of seasons in the simulation and the radiative simplicity of the physics package, it is not surprising that the the polar latitudes are cooler compared to equatorial latitudes. However, the upper atmosphere shows a different trend, which could be due to the approximations of the physics package or difference between the stratosphere and troposphere.

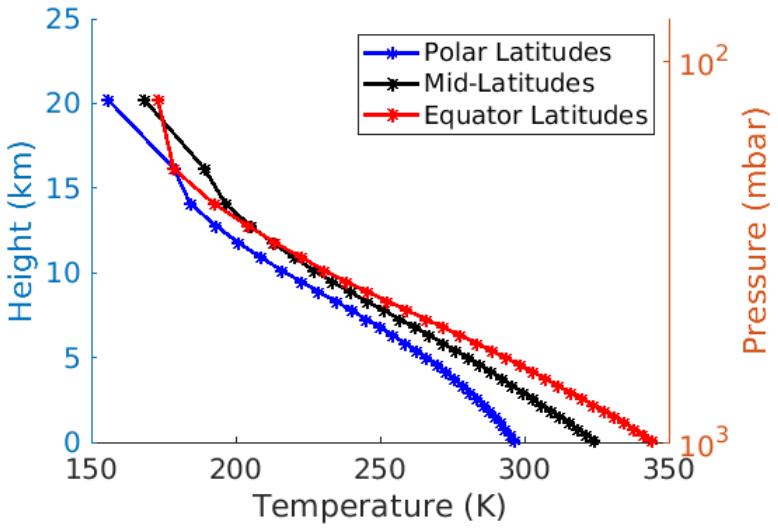

FIGURE 6.11: The profile of the temperature averaged over the sphere for different zonal regions at the end of a five year simulation. The polar latitudes, mid-latitudes and equatorial latitudes represents all latitudes between $0° - 23.5°$, $23.5° - 66.5°$ and $66.5° - 90°$ respectively. The results are from a simulation including the soil model. The trend of a cooler polar profile is observed. While the mid-latitudes are cooler than the equatorial latitudes up until $\sim$ 12 km.

6.5 Grid convergence

An important property of any discrete spatial model is grid convergence (i.e. that the numerical approximation error tends to zero as the horizontal or vertical grid spacing is decreased). In many applied situations there are no analytic solutions to the continuous equations, as in the case of climate modeling. Therefore, we follow convention by taking the finest resolution as an approximation of the exact solution and look at the differences between it and progressively coarser simulations. Since the convergence

properties of the dynamical core have already been established (Kevlahan and Dubos 2019), we are interested in checking that statistical properties of the simulation converge as the grid size is decreased. In other words, we conduct a convergence study of the physics model. This study focuses on the vertical temperature profile, and presents a temperature profile from each horizontal resolution simulation. The study includes the error between the highest resolution (0.5°) and the other resolutions. If the simulation is numerically convergent, we expect that as the resolution increases the difference between each subsequent temperature profile will decrease.

Four horizontal grid scales are considered in the study: 4° ($\sim$ 480 km), 2° ($\sim$ 240 km), 1° ($\sim$ 120 km) and 0.5° ($\sim$ 60 km). Furthermore, the setup of the simulations, except in the horizontal resolution, is exactly as explained in the introduction of this chapter: the 30 vertical levels and 10 soil layers. All simulations are run for one year. While it is optimal to at least reach a steady state, which was determined to be three years, that was unachievable with the available computational power at the finest resolution (CPU time for the one-year simulation increases like $(1/\Delta x)^3$). This means that the finest resolution is about 512 times as costly as the coarsest resolution for the non-adaptive case considered here. The fluctuations of the one-year mean values of the prognostic and diagnostic variables are less than 5% after one year, which is reasonably close to a statistically stationary state.

Figure 6.12 displays different portions of the temperature profile to display the trend. Within the first kilometre of the atmosphere (figure 6.12a) and at 5 km in the atmosphere (figure 6.12b) the trend of a decrease in the difference of subsequent profiles as the resolution increases is seen. The difference between the results is greatest at higher altitudes, from 13–20 km, although grid convergence is seen at all heights. However there is less vertical granularity, with respect to grid points, at these altitudes and the temperature is not realistic for the stratosphere due to the lack of a UV radiation band.

Table 6.2 displays the mean difference (absolute error) between each resolution (4° ($\sim$ 480 km), 2° ($\sim$ 240 km) and 1° ($\sim$ 120 km)) and the reference resolution of 0.5° ($\sim$ 60 km). The mean was calculated over the differences for all 30 layers. The mean values display a decrease in temperature difference as the resolution increases and approaches the finest resolution. For the differences at each atmospheric layer see table B.6 in Appendix B.5.

Figure 6.13 displays the absolute error of all three coarsest resolutions with respect to the finest resolution. More specifically the errors included are the 1-norm (mean of all layers) errors, 2-norm (of all layers) errors and the errors of 4 layers at different pressures in the atmosphere; Layer 5 ($\sim$ 850 hPa), 10 ($\sim$ 683 hPa), 20 ($\sim$ 350 hPa) and 30 ($\sim$ 17 hPa). All errors seem to have a first order rate of convergence, except layer 5. Initially layer 5 exhibits a steeper slope than that of linear convergence, however this could be the result of conducting the study for one year simulations, when the temperature has not fully reached its steady state. Therefore the coupled model's rate of convergence is approximately first order $O(dx)$.

Overall both the temperature profile and the mean differences display a decrease in temperature difference, with the finest resolution as the reference temperature, as the resolution increases towards the finest. Furthermore the temperature profiles portray a decrease in the difference between subsequent temperature profiles as the resolution refines. Therefore we deem the physics model to be linearly convergent.

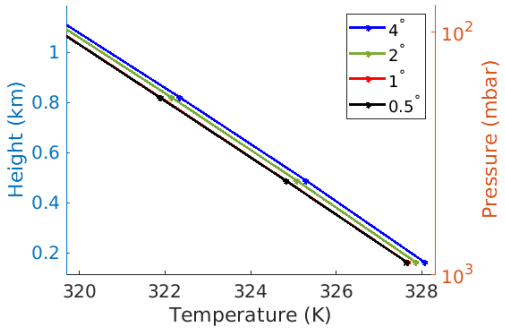

(a) Height of 1 km

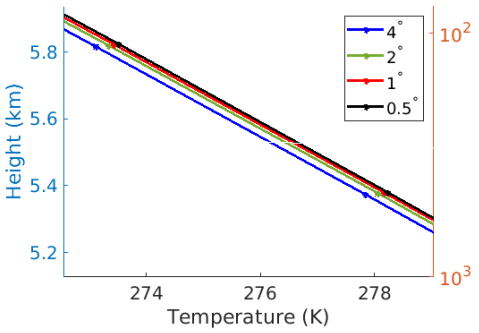

(b) Height of 5–6 km

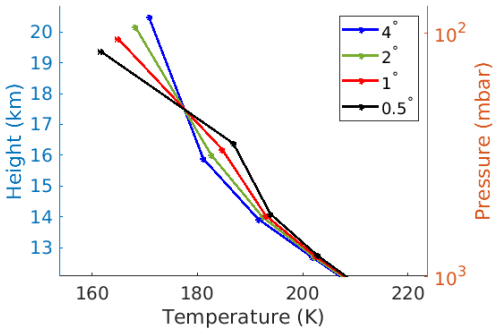

(c) Height of 13–20 km

Figure 6.12: Grid convergence profiles of the resolutions 4° (∼ 480 km), 2° (∼ 240 km), 1° (∼ 120 km) and 0.5° (∼ 60 km) at heights of 1 km, 5 km and 13–20km in the atmosphere. The trend of a decrease in subsequent profiles at the resolution decreases is observed.

Resolution	4°	2°	1°
Error	0.8675 K	0.5868 K	0.2666 K

Table 6.2: The mean temperature difference, at one year, between the coarsest resolutions (4° (∼ 480 km), 2° (∼ 240 km) and 1° (∼ 120 km)) and the finest resolution of 0.5° (∼ 60 km). The mean was calculated over the differences for all 30 layers. The mean values display a decrease in difference as the resolutions approach the finest grid resolution.

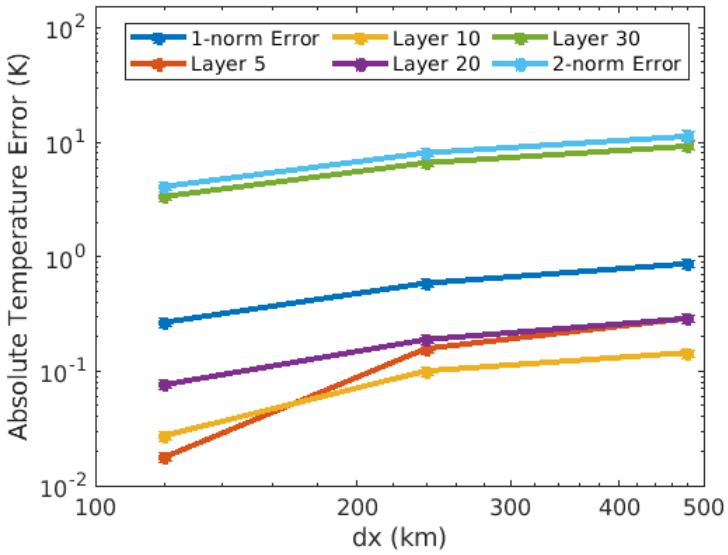

Figure 6.13: The absolute temperature error of the coarser resolutions (4° (∼ 480 km), 2° (∼ 240 km) and 1° (∼ 120 km)) with respect to the finest resolution of 0.5° (∼ 60 km). The plot displays the the 1-norm (mean of all layers) errors, 2-norm (of all layers) errors and the errors of 4 layers at different pressures in the atmosphere; Layer 5 (∼ 850 hPa), 10 (∼ 683 hPa), 20 (∼ 350 hPa) and 30(∼ 17 hPa). The rate of convergence appears to be linear for the means and all layers, except layer 5.

6.6 Performance testing of the physics and dynamics steps

The performance tests evaluate the computational overhead of the physics model dynamics across the four horizontal grid resolutions. The objective of the performance tests is to determine the additional computational cost of coupling to the physics package and its dependency on resolution. This helps us decide whether the physics package requires further numerical optimization, or whether the additional computational time is negligible compared to the dynamics.

Resolution	Total CPU time (s)	Dynamics CPU time (s)	Physics CPU Time (s)
4°	1.2670	0.6973 (54.9%)	0.5740 (45.2%)
2°	6.7387	3.6956 (55.5%)	2.9523 (44.4%)
1°	18.1970	9.9378 (54.6%)	8.2667 (45.4%)
0.5°	62.8238	31.4188 (50.0%)	30.6243 (48.9%)

Table 6.3: The results of a performance test run in serial including CPU time of a full time step, the dynamics step only and the physics step only. Furthermore, the percentages of the the full time step for the dynamics and physics step are included for the four resolutions. (Resolutions: 4° (∼ 480 km), 2° (∼ 240 km), 1° (∼ 120 km) and 0.5° (∼ 60 km).

Table 6.3 presents the total CPU wall-clock time of a single physics and dynamics time step (i.e. a full time step), the time allocated to the dynamics step, the time allocated to the physics step and their percentages with respect to the full time step. The results are observed for 4 resolutions, 4° (∼ 480 km), 2° (∼ 240 km), 1° (∼ 120 km) and 0.5° (∼ 60 km), with each resolution running on a single core to remove the overhead that comes with parallelism. The simulations were run on the same machine, in double precision for 30 time steps to allow the simulation to stabilize before taking the average of the following 20 time steps.

Across all resolutions, the dynamics step requires a slightly greater amount of time of the total time step, while the physics is approximately 3% more costly for the finest resolution (0.5°). This small increase is likely due the overhead from the memory access of gathering the prognostic variables and converting between data structures for each column. Overall in the serial case the overhead of the physics is ∼ 50% of the total time step. In general, the coupled simulations are run in parallel with multiple cores. Therefore table 6.4 displays the four resolutions of 4° (∼ 480 km), 2° (∼ 240 km), 1° (∼ 120 km) and 0.5° (∼ 60 km) run on their optimal number of cores of 40, 160, 320 and 640 cores respectively. Furthermore the full time step, dynamics step and physics step were run in double precision for 30 time steps to allow the simulation to stabilize before taking the average of the following 20 time steps.

Resolution	Cores (Nodes)	Total CPU time (s)	Dynamics CPU time (s)	Dynamics Scalability	Physics CPU Time (s)	Physics Scalability
4°	40 (1)	0.055	0.038 (69.6%)	-	0.017 (30.7%)	-
2°	160 (4)	0.14	0.066 (46.1%)	1.7	0.077 (51.3%)	4.3
1°	320 (7)	0.51	0.11 (21.3%)	1.4	0.39 (77.7%)	11.6
0.5°	640 (14)	2.1	0.36 (16.9%)	2.3	1.7 (83.3%)	26.4

Table 6.4: The results of a performance test for simulations run in parallel on the indicated number of cores. As the number of cores increase, the number of nodes required, shown in brackets, increases as well. Results include the CPU time of a full time step, a dynamics step only and a physics step only, as well as the scalability of the dynamics and physics step. Furthermore, the percentages of the the full time step for the dynamics and physics step are included for the four resolutions. Resolutions: 4° (∼ 480 km), 2° (∼ 240 km), 1° (∼ 120 km) and 0.5° (∼ 60 km).

For the smallest resolution (4°), the dynamics step take the most amount of time. The main conclusion is that the computational overhead of the physics model increases with increasing resolution when the coupled simulation is run in parallel. This is potentially due the overhead of parallel communication, especially since the physics percentage increases with the increase in number of cores. Another metric of performance is the weak scalability of the model. Weak scaling looks at the effects of increasing the problem size and the number of CPU cores. Theoretically, perfect weak scaling produces a value of one, even as the problem size and number of CPUs increases. The dynamics step scales quite well, however, as seen in table 6.4 the physics does not scale well, further emphasizing poor parallel efficiency of the physics.

An initial profiling of the parallel simulations, for one day without dynamics at the different resolutions, indicates that the inefficiency of the physics step is due to parallel communication overhead. The parallel overhead grows as the resolution increases, despite implementing non-blocking communication. A significant factor in this increase is the "MPI_Waitall" command of the necessary boundary update at the end of each physics step. As more nodes are required with an increase in CPU cores, potential contributing factors to the increase in parallel overhead with resolution include the communication across nodes and variations in performance across nodes. Furthermore, the one day profile reveals that as the resolution increases the extensive computation of the physics is a major contributor to the overall CPU time of the entire parallel simulation. The longwave and shortwave radiative transfer models, as well as the vertical diffusion model, significantly contribute to the substantial computational cost taking $\sim$ 40 seconds (s), 12 s and 15 s per grid cell respectively. The extensive computation of the physics could have an effect on the parallel overhead, especially if the load balancing across cores is not equal or if there is a performance difference across nodes. More specifically, when comparing profiles of parallel simulations with and without parallel communication, the computation of the physics adds to the overall CPU time when parallel communication was included. Therefore the cause of the parallel inefficiency of a simulation is a combination of the parallel overhead bottleneck and the physics extensive computation.

In conclusion, since the overhead of the physics model dominates at high resolutions when run in parallel, an effort should be made to increase its efficiency (e.g. improve parallel efficiency, not evaluating the physics separately at each grid point if it varies on a larger time scale).

Chapter 7

Climatology

The climatology of a climate model is a description of its statistical equilibrium state for a given set of conditions. Climatology is an important characteristic of a climate model, as it provides researchers with a baseline of the model dynamics for which to compare the effect of perturbations or different forcing scenarios. In many cases, the climatology of models is investigated using the concept of climate normals. Climate normals can be used to understand the dynamics of models and the dynamics of climate conditions in particular regions using simulation output and observational data respectively. A climate normal, sometimes referred to as climate average, is the mean representation of particular climate conditions, usually a climate variable, over a period of time, called the reference period. The current standard reference period for observational data of particular locations is 30 years. The reference period for climate models is specific to the model being considered.

The following section presents and analyzes the climatology of WAVETRISK coupled to the physics package with 10 soil layers, 30 atmospheric levels, no seasons and a horizontal grid resolution of 2°. The climate normals considered are for the prognostic variables, the temperature and kinetic energy (KE) (per unit volume), with a reference period of five years. Furthermore a comparison of the eddy KE between the coupled simple physics package simulation and a Held–Suarez simulation is presented. Note that the zonal and meridional KE climate normals include density, while the eddy KE does not.

The climate normal for the vertical temperature profile is averaged both spatially and temporally (over the reference period). The temperature climate normals also include two-dimensional (2D) projections of the period averaged temperature on the sphere. Each projection is taken at different slices of pressure in the atmosphere.

Figure 7.1 presents the resulting temperature profile, which is spatially averaged over the sphere at each layer and temporally averaged over five years. The temperature decreases monotonically with height. As seen in the instantaneous profile, in the results section (figure 6.10), the surface temperature is warmer than expected ($\sim$ 334 K) and the upper atmosphere is cooler than expected, with an upper atmospheric layer of $\sim$ 169 K. As discussed earlier, this is due to the lack of moisture and UV radiation band respectively.

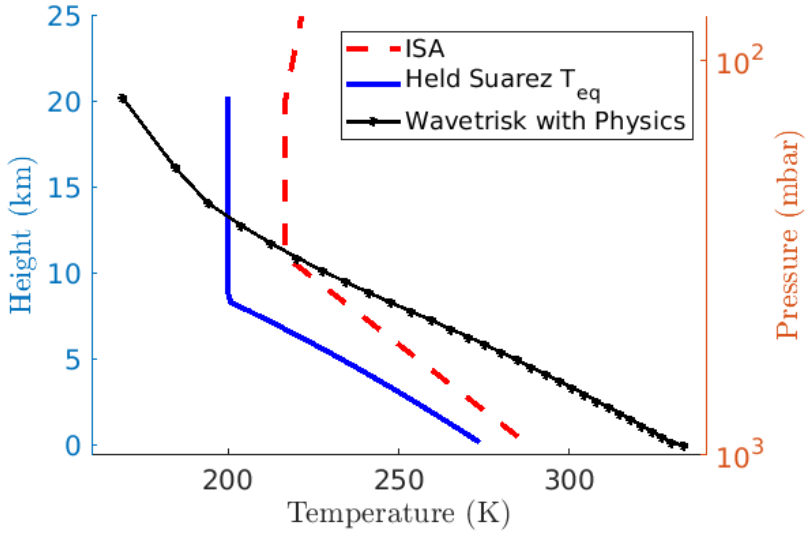

FIGURE 7.1: Temperature profile averaged over five years, after reaching steady state, from a WAVETRISK with physics simulation with 10 soil layers. The observed trend of the profile is a decrease in temperature with height. The figure also displays the International Standard Atmosphere (ISA) profile and the Held-Suarez temperature equilibrium (Teq) for comparison.

Figure 7.2 displays the 2D projection of the five year temperature normal from a WAVETRISK with simple physics simulation. Due to the averaging over five years, it is expected that the projection displays meridional structure and no zonal structure compared to the projections taken at an instantaneous time within the simulation. Figures 7.2a and 7.2b are computed at a pressure of 850 hPa and 350 hPa in the atmosphere respectively. Both display the expected structure, and also show the Earth's meridional temperature trend of a warmer equator and cooler poles. The climate normals also show that further up in the atmosphere, at 350 hPa, the temperature is cooler than at 850 hPa, as shown in the temperature profile (figure 7.1).

Due to the effect of averaging in climate normals, much of the turbulence structure is averaged out. To reveal the structure of turbulence, and compare the climatology to the instantaneous weather, figure 7.3 displays the the instantaneous temperature and vorticity projection at a pressure of 850 hPa for day 3 650 (ten years). Figure 7.3a displays the temperature projection, with the same meridional trend of a warmer equator and cool poles. However there are more fluctuations in the instantaneous projection which depicts the effects of turbulence. Figure 7.3b displays the instantaneous vorticity projection. We assume that the vorticity is a good diagnostic for visualizing turbulence. With the temperature and vorticity projections side by side, it can be observed that the temperature fluctuations follow the vorticity, therefore confirming that the temperature

is behaving approximately like a passive scalar and the turbulence structure determines the temperature structure. Overall, both the instantaneous projections and the climatology normals display very similar meridional temperature trends. However, averaging removes the effect of turbulence, while the instantaneous projections reveal the "weather" of the coupled climate model (not present in the uncoupled runs).

The climate normals for the zonal and meridional KE present the climatology in terms of the KE per unit volume (including density) from a WAVETRISK with simple physics simulation. The normals include 2D projections and zonally averaged vertical slices. The 2D projections are the time averaged zonal and meridional KE per unit volume across the sphere at different pressure levels in the atmosphere. While the vertical slices are the zonally and temporally averaged zonal and meridional KE per unit volume with respect to height and latitude.

Figure 7.4 displays the 2D projection of the five year averaged zonal KE per unit volume at a pressure of 850 hPa (figure 7.4a) and 350 hPa (figure 7.4b). While both projections display a bit of zonal variation in KE, especially in the latitude bands with the highest KE, an overall meridional trend is still dominant. At both pressures the mid-latitudes have the highest KE, which diminishes as the latitudes approach the equator and poles. At 850 hPa, there is more zonal structure, which is due to turbulence and the zonal KE diminishes toward $\sim 10 kg/ms^2$. In contrast at 350 hPa, there is a wider range of KEs, approaching zero and $\sim 10 kg/ms^2$ as the latitudes approache the equator and poles respectively. The difference in scale between the two pressures is 2.5 times, with the lower pressure having the highest KE at the mid-latitudes of $\sim\ 200 kg/ms^2$.

Figure 7.5 displays the 2D projection of the five year meridional KE per unit volume normal at a pressure of 850 hPa (figure 7.5a) and 350 hPa (figure 7.5b). As seen in the zonal KE climate normals, there is some variation in the zonal direction, but a prominent meridional trend also remains. Furthermore, the highest KE, at both pressures, occurs at the mid-latitudes. The KE at these altitudes shows a variable amount of zonal structure that diminishes towards the equator and poles. At 850 hPa there is more zonal structure due to higher turbulence levels and the gradual reduction in KE towards $\sim\ 10 kg/ms^2$ occurs near the poles and equator. In contrast, at 350 hPa, the meridional trend is more pronounced. The meridional KE approaches zero near the equator, while there is only a slight reduction near the poles to $\sim 30 kg/ms^2$.

In general, for both KE components, there is some zonal variation in KE, especially at the lower pressure, which indicates that there is still some effect of turbulence even after a five year averaging. The zonal bands of high KE, at the mid-latitudes, are indicative of a zonal jet, whose profile can be confirmed in the zonally averaged vertical profiles (figure 7.6). Note that there is a three times difference in scale between the zonal and meridional KE at 350 hPa, while the higher pressure scales are similar. Overall, for both KEs components, it can be seen that the scales for both pressures are within range of the spatially averaged steady state (figure 6.9 & 6.8) for their corresponding layer.

Figure 7.6 presents a five year zonally averaged vertical profile of the zonal and meridional KEs per unit volume. The profile presents the KEs as a function of latitude and normalized pressure, where the surface pressure $P_s = 10^3$ hPa. Figure 7.6a and 7.6b are the zonal and meridional KE vertical slices respectively. Both indicate the largest KE occurs at a normalized pressure of ~ 0.35 and a zonal jet profile at the mid-latitudes. Interestingly the meridional KE displays a smaller increase in KE at the normalized pressure of ~ 0.85. As seen in the 350 hPa 2D projections, there is a three time difference in scale between the zonal and meridional KE.

Overall the KE climate normals are indicative of the magnitudes of the zonal and meridional velocities, especially in the lower atmosphere. They indicate the peak zonal and meridional KE at a pressure of ~ 350 hPa and a zonal jet at the mid-latitudes.

To compare the zonal jet feature produced by the simple physics package, figure 7.7 displays the zonally and temporally averaged vertical profiles of the eddy KE from a simple Held–Suarez physics test case and the simple physics package. The eddy KE represents the variance of the the total KE (i.e. zonal and meridional KE) without density. The simple physics package results are those of a coupled simulation with the setup explained at the beginning of the chapter (i.e. a 2° horizontal resolution). The Held–Suarez results, produced by Kevlahan and Dubos (2019), are from an adaptive WAVETRISK simulation across the resolutions of 4°, 2° and 1°, using the initial conditions of Jablonowski and Williamson 2006. Both simulations had a model top of 10^3 hPa, but used different vertical coordinates and initial conditions.

The use of adaptivity and different initial conditions are significant differences among the cases. However the goal is to compare the zonal jet structure of the coupled simple physics results to that of the simplest physics model, as the zonal jet is a basic and important feature that can be found in the output of simple climate models. The major difference among the profiles is the large amount of eddy KE at the top of the mid-latitudes in the simple physics coupled profile. Other differences among the profiles includes the shape of the contours and the scale of the eddy KE. Overall in both cases, the largest variance occurs at a normalized pressure of $\sim$ 0.25 and the jets of both profiles were centered at at the mid-latitudes.

In conclusion, the climatology chapter presented the spatially and temporally averaged temperature profile, the five-year climate normals for temperature, zonal KE and meridional KE of the coupled simulation and compared the zonally averaged eddy KE of the coupled simulation to that of a simple Held–Suarez simulation. These normals and the profile are a benchmark of the expected climate of Earth for simulations using the physics package with no seasons.

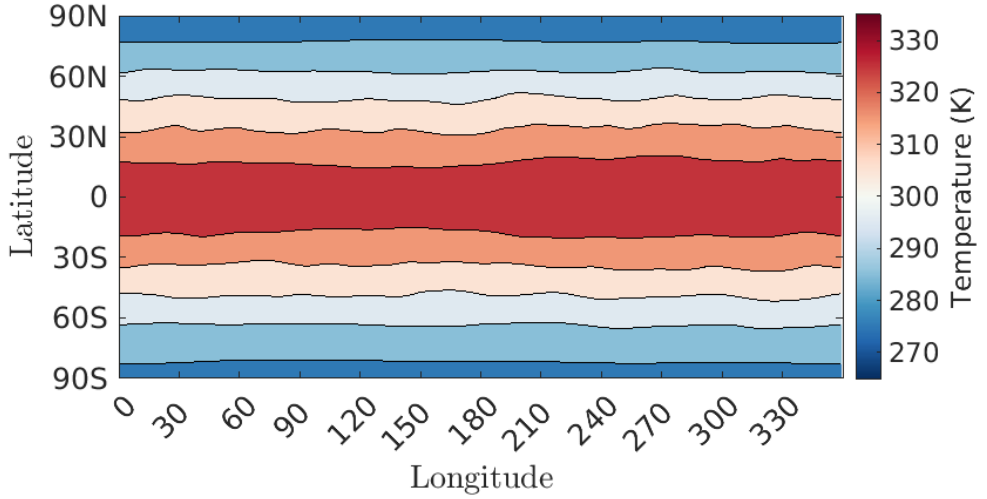

(a) Five Year Projection at 850 hPa (∼ 1.5 km, ∼ layer 5).

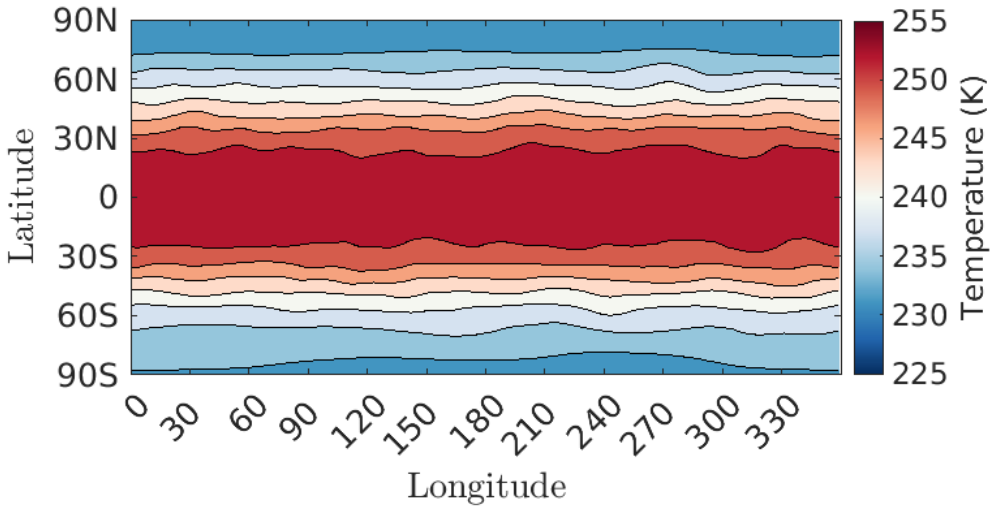

(b) Five Year Projection at 350 hPa (∼ 8 km, ∼ layer 20).

Figure 7.2: A 2D projection of a five year temperature normal from a wavetrisk with simple physics simulation, without seasons. Figure 7.2a displays the projection at a pressure of 850 hPa. Figure 7.2b displays the projection at a pressure of 350 hPa. The temperature displays a meridional trend with a warmer equator and cooler poles.

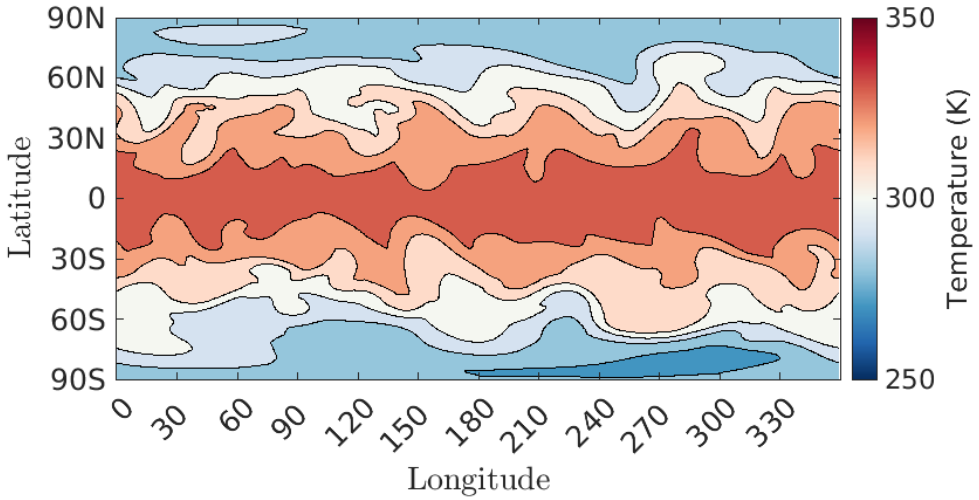

(a) Day 3650 Temperature Projection at 850 hPa (∼ 1.5 km, ∼ layer 5).

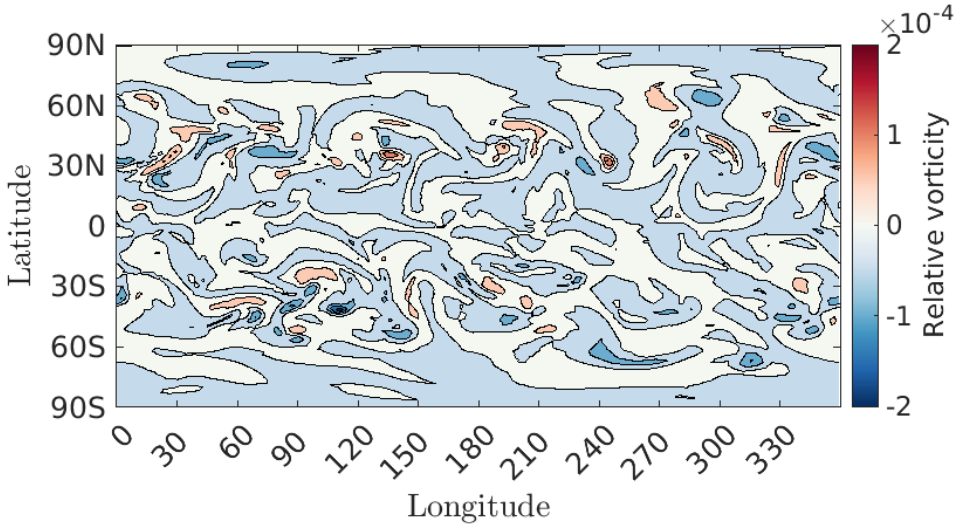

(b) Day 3650 Vorticity Projection at 850 hPa (∼ 1.5 km, ∼ layer 5).

Figure 7.3: A 2D projection of the temperature and vorticity at the end of a 10 year wavetrisk with simple physics simulation, without seasons. Figure 7.3a displays the temperature projection at a pressure of 850 hPa. Figure 7.3b displays the vorticity projection at a pressure of 850 hPa. The temperature displays a meridional trend with a warmer equator and cooler poles. In comparison to the five year climate normals (figure 7.2), the instantaneous plot display the instantaneous fluctuations and the effects of turbulence. The vorticity is commonly used to visualize turbulence and the temperature fluctuations follows the vorticity.

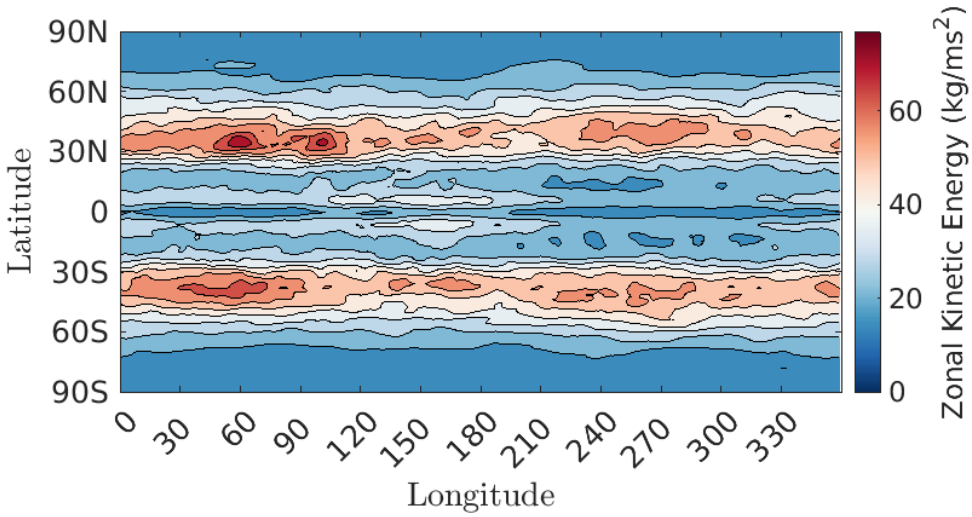

(a) Five Year Projection at 850 hPa ($\sim$ 1.5 km, $\sim$ layer 5).

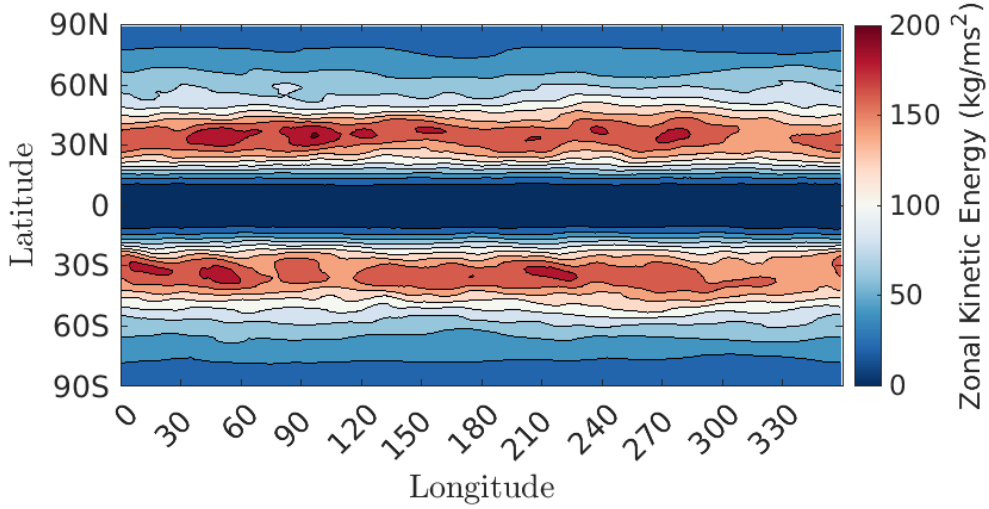

(b) Five Year Projection at 350 hPa ($\sim$ 8 km, $\sim$ layer 20).

Figure 7.4: A 2D projection of a five year zonal KE normal from a wavetrisk with simple physics simulation, without seasons. Figure 7.4a displays the projection at a pressure of 850 hPa. Figure 7.4b displays the projection at a pressure of 350 hPa. At both pressures, the higher KEs occur in the mid latitudes and gradually diminishes as the latitude approaches the equator or the poles. These high KE bands are indicative of zonal jets.

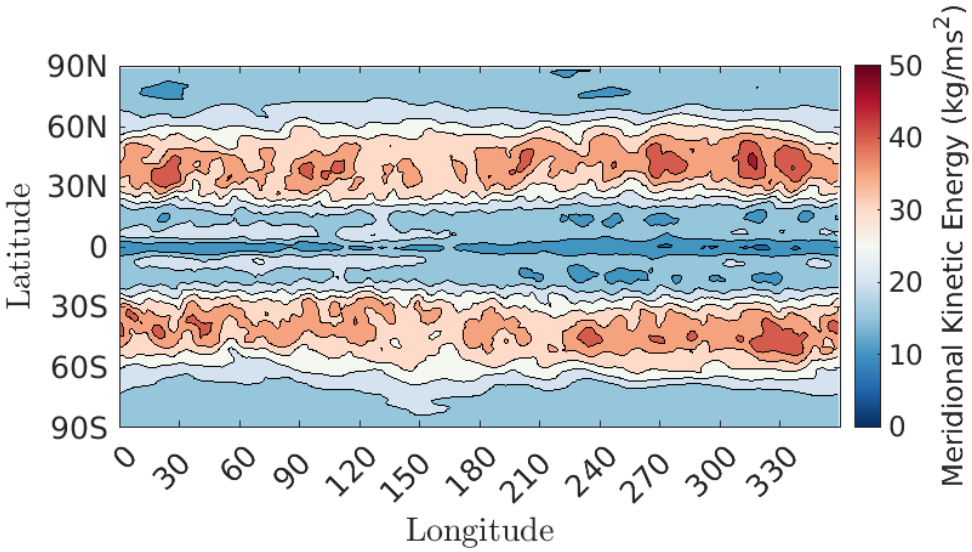

(a) Five Year Projection at 850 hPa ($\sim$ 1.5 km, $\sim$ layer 5).

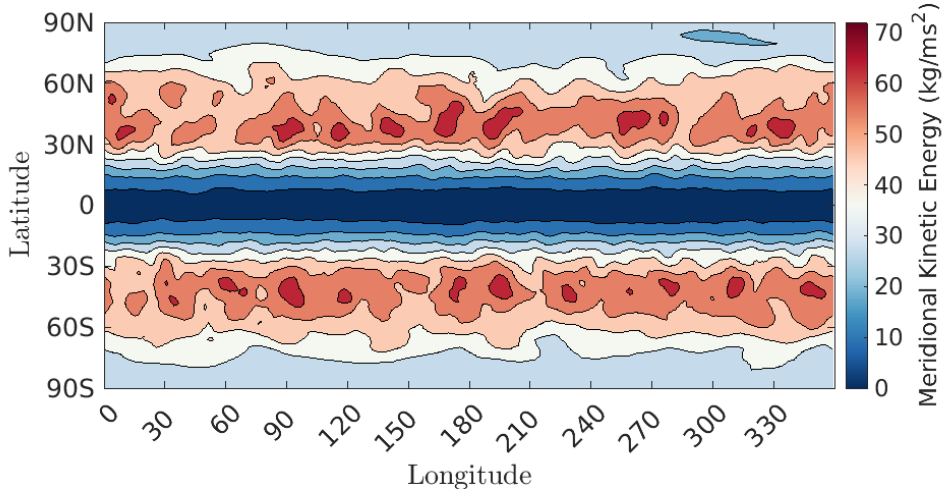

(b) Five Year Projection at 350 hPa ($\sim$ 8 km, $\sim$ layer 20).

Figure 7.5: A 2D projection of a five year temperature normal from a wavetriskwith simple physics simulation, without seasons. Figure 7.5a displays the projection at a pressure of 850 hPa. Figure 7.5b displays the projection at a pressure of 350 hPa. While both projections have some zonal structure, it is clear that most of the meridional KE is in the mid-latitudes gradually decreases as the latitude approaches the equator and the poles.

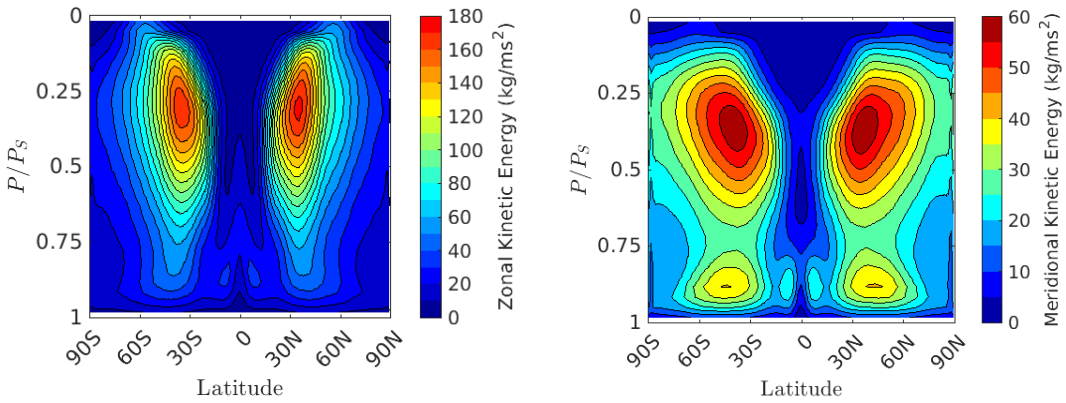

(a) Zonal KE. (b) Meridional KE.

FIGURE 7.6: Zonally averaged and 5 year temporally averaged zonal and meridional KE with respect to normalized pressure. The zonal KE (figure 7.6a) and meridional KE (figure 7.6b) display a zonal jet at the mid-latitudes.

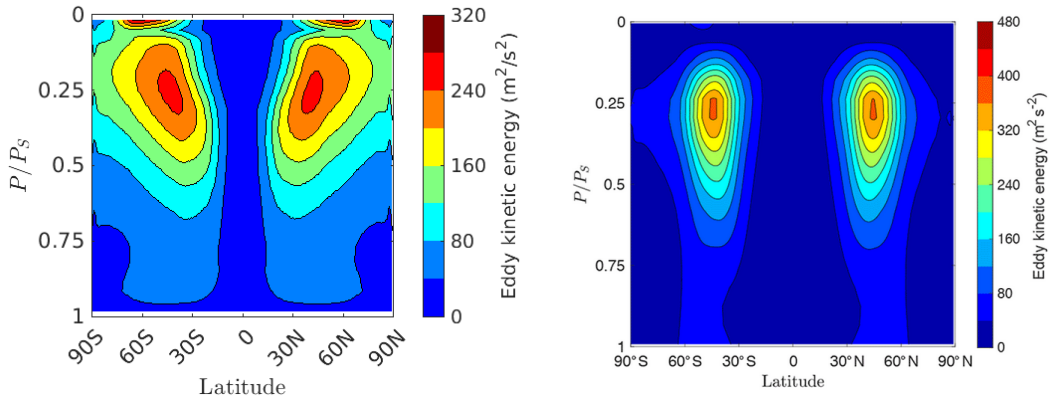

(a) Simple Physics Eddy Ke. (b) Held–Suarez Eddy KE.

FIGURE 7.7: Zonally temporally averaged eddy kinetic energy (KE) (i.e. variance) of a Held–Suarez simulation and the simple physics simulation. The KE is the total KE excluding density. The Held–Suarez profile, produced by Kevlahan and Dubos (2019), are from and adaptive simulation with different initial conditions. However the mid-latitudes zonal jet is apparent in both profiles. A major difference between the profiles is large amount of variance at the top of the mid-latitudes in the simple physics results.

Chapter 8

Conclusions and Next Steps

This thesis has introduced specific concepts required for understanding the concepts underpinning climate modeling of the atmosphere, summarized the taxonomy of the current generation of Atmospheric Global Climate Models (AGCMs), and presented and situated the simple dry physics package we implement here. We characterized the climatology of this physics both uncoupled to dynamics and coupled to the non-adaptive version of the WAVETRISK dynamical core. One of the main aims of investigating this physics package was to understand in depth a physics module, with clearly stated assumptions and approximations, that could be used in both non-adaptive and adaptive test cases. Therefore, researching the non-adaptive case for Earth was the first step in understanding the package and achieving this goal. Additional advantages of this particular physics package is its capability to model various planets and its potential to be easily coupled with a wide variety of dynamical cores.

The core assumption of the physics package is the exclusion of moisture, but it does include parameterizations for radiation, small-scale turbulence, planetary boundary layer, surface fluxes, convection, and soil. While the package is related to the more complex aquaplanet models by its inclusion of a simple soil model, it is precisely this inclusion that distinguishes it from most other dry physics models. The other schemes included in the package are either simpler or comparable to those used in the dry and wet physics hierarchy models. As a result, the physics package introduces another level of complexity to the dry physics hierarchy, through the incorporation of the simple soil model.

Before coupling the package with a dynamical core, an investigation into the characteristics of the package, when run uncoupled to a dynamical core, explored the trends of the temperature, zonal and meridional velocities and the vertical temperature profile in comparison to other standard profiles. It was observed that the globally averaged temperature of each atmospheric layer reaches a steady state, while the velocities decayed towards zero due to the lack of dynamical forcing. Furthermore, the vertical profile showed a warmer surface temperature and cooler upper atmosphere temperature in comparison to the standard atmosphere model for Earth and the Held-Suarez model temperature equilibrium, most likely due to the dry physics assumption and lack of a UV absorption band in the upper atmosphere.

To facilitate the coupling of the simple dry physics package with the WAVETRISK dynamical core, a new interface was created. The interface took account of the data structures of the prognostic variables of both the dynamics and physics, converting all inputs and outputs to the desired structure. Furthermore, a major design decision of the program was to call the physics for each single column individually. This was required due to the type of load-balancing employed by the dynamical core. Finally, to couple the package, expansions described in Chapter 5 were made to both WAVETRISK and the simple dry physics package to allow for the single column physics calculations.

Additional attributes examined for the package, while coupling with WAVETRISK, included precision and sensitivity. The package is written in single precision, which is not compatible with higher precision dynamical cores, however a compilation flag was included to increase to double precision. Lastly, it was observed that that physics can be quite sensitive to certain inputs. An initial test showed that while it is not highly sensitive to initial temperature perturbations, it is highly sensitive to other parameters. For example, the fraction of each day is required in the physics package step input. Since round off errors can be expected, a small perturbation at any point to this parameter can cause very different outputs.

Initial tests into the resulting effects of coupling the simple dry physics package with the dynamical core WAVETRISK were explored in the non-adaptive case. The goal behind coupling in the non-adaptive case was to gain benchmark characteristics and results that can be compared with those obtained when coupling in the adaptive case in the future. Upon the initial coupling to the package, with obliquity and other parameters set for Earth conditions, an unrealistic temperature trend was observed: a warmer summer pole and cooler winter pole (more associated with the stratosphere rather than the troposphere). Setting obliquity to zero led to a realistic warmer equator trend and therefore all subsequent runs did not include seasons.

First, an investigation into the effects of the inclusion of the soil model displayed that with more soil layers included, more time scales are available for retention and release of heat. Therefore, the vertical profile trend displayed an overall cooler profile for simulations with more soil layers, which is consistent with convergence. The only unexpected feature of the temperature profile, was near the surface where the simulation with no soil layers was the coolest, followed by the 10 soil layer and 4 soil layer profiles. The surface results could be indicative of the inaccuracy of the no soil simulation boundary conditions. However with only 3 profiles, we can not conclude if the model is convergent with respect to the number of soil layers.

The time convergence of the temperature, zonal kinetic energy (KE) and meridional KE were obtained for the coupling with 10 soil layers. In all three cases, the model is stable and converged to a steady state within 3 years. In comparison to the uncoupled time series the major points of interest were the temperature equilibrium differences at the top two atmospheric layers. The coupled temperature equilibrium was $\sim$ 15.5 K cooler at the top atmospheric layer and $\sim$ 15 K warmer at the second last layer. All other layers had a temperature equilibrium difference of $\sim$ 6 K or less.

The crude grid convergence study displayed a decrease in temperature difference as the resolution approached the finest reference grid, therefore deeming the model linearly convergent with a rate of convergence of $O(dx)$. In terms of the performance, when the coupled model is run in serial, the physics step contributes to $\sim$ 50 % of the overall time step across all resolutions. However, in parallel the computational overhead of the physics step increases with resolution, in so much that at finer resolutions the physics step is a significant contributor to the overall performance of a single time step. This is likely due to parallel communication overhead and an effort should be made to improve the efficiency of the physics step when run in parallel.

A correct vertical temperature profile, of the coupled simulation, is important and while the overall globally averaged temperature trend observed was a decrease in temperature with height, two major differences were noted compared with the standard temperature profile for Earth. The temperature near the ground was hotter and the temperature of the upper atmosphere was cooler than that of the International Standard Atmosphere (ISA). While the warmer surface temperature is attributed to the lack of moisture, the cooler top atmosphere is due to the simplicity in the radiation model. The addition of an extra UV band is required in order to display the expected trend of an increase in temperature upon entering the stratosphere. In comparison to the uncoupled simulation, the coupled surface temperature was cooler and the mid to upper atmosphere was increasingly warmer. The upper atmosphere of the coupled simulation profile seemed to be slightly more realistic, than that of the uncoupled, with a decreased cooling rate above the troposphere.

Lastly, the climatology of the package coupled to WAVETRISK was presented to provide five year climate normals and a temperature profile for the coupling. The temperature profile, averaged across a span of five years, exhibited a tendency of temperature decline with increasing altitude, while the 2D projections revealed the meridional pattern of a warmer equator and cooler poles. A comparison to the instantaneous temperature projection showed more fluctuations in the instantaneous temperature depicting the effects of turbulence. Therefore the climate temperature averaging removes the effects of turbulence, while the instantaneous projections reveals the weather of the coupled model. The 2D climatic averages for zonal and meridional KE per unit volume demonstrated higher KE levels in the mid-latitudes. These high KE zonal bands are know as zonal jets. The KE vertical structure was fully portrayed in the zonally averaged vertical profiles, displaying the highest level of KE at $\sim$ 350 hPa for both KEs.

The objective of the previous tests were to investigate the simple dry physics package coupled to the non-adaptive version of the dynamical core WAVETRISK for Earth-like parameters. The major differences compared with Earth climatology were the mean global temperature near the surface and at the top of the atmosphere. These differences are likely due to the neglect of moisture and the lack of a realistic upper atmosphere radiation model. However, these are only preliminary results using a single initial condition. In the immediate future it is suggested that the physics package be tested with different

initial conditions to ensure model stability. Moreover an investigation into the incorrect meridional temperature trend when the obliquity is 23° (i.e. seasons) is crucial.

Based on the initial sensitivity results we have obtained when coupling the simple dry physics with WAVETRISK, a sensitivity analysis of the simple dry physics package is recommended. We expect that a sensitivity analysis will provide a comprehensive list of variables and parameters that are sensitive to perturbations. More importantly, it will reveal their relative significance and relevance to the atmospheric climate. Since one goal of the physics package is its ability to be coupled with different dynamical cores, the sensitivity analysis will provide guidance for future couplings and test cases.

A key distinction of the simple dry physics package is its incorporation of the soil model. Based on the initial results comparing the profiles of simulations with varying amounts of soil layers, it is recommended that a more comprehensive study is conducted to validate the convergence with respect to the number of soil layers. The additional profiles can also enable further analysis into the convergence of the surface temperature and the potential inaccuracy of the no soil simulation boundary conditions.

A desired quality of the physics package coupling is efficiency when run in parallel. Currently the physics package lacks this quality and an immediate effort should be made to improve the efficiency and performance of the physics at high resolutions when run in parallel. After profiling the parallel simulation, the extensive computation of the physics and the subsequent boundary updates (requiring all processors to wait) are producing the parallel overhead of the high resolution simulations and requires optimization. A potential solution to improve performance at higher resolutions is the use of shared-memory parallelism (i.e. OpenMP) with the current distributed-memory (MPI) parallelism. Incorporating OpenMP threads within each MPI processor can speed up the evaluation of the physics at each time step. This can be done by dividing the vertical level physics calculation loop across the threads.

The major next step, beyond the immediate suggestions above, is to test the physics package coupled to WAVETRISK with the adaptivity turned on. This will allow us to compare the results with the non-adaptive results presented in this thesis, and also determine if the simple dry physics package needs to be modified when coupled to an adaptive dynamical core. For example, the question of whether some components of the physics package need to be made "scale aware". Furthermore, a future step includes the intercomparison of a range of dynamical cores coupled to the same simple dry physics package. With an understanding of the small differences among different dynamical cores, this intercomparison would be a good test of the consistency of the physics package (as well as a test of the robustness of the dynamical cores to different physics packages). Finally, testing the physics package with other planets could provide clarity on the robustness of the simple dry physics model with respect to different parameter sets and dynamical ranges and should reveal any deficiencies that need to be corrected. For example, Venus is a possible planet that can be simulated using the package and will provide insight into the package flexibility, especially since the climate of Venus is very different from that of Earth.

Appendix A

Chapter 3 Supplementary Material

A.1 Physics package input parameters

The input parameters, their variable name and default values of the simple dry physics package are below in the form "parameter (variable name), default value":

- Planet radius (planet_rad), $6.4e6m$
- Acceleration due to gravity (g), $9.8m/s^2$
- Specific heat capacity (cpp), $1004Jkg^{-1}K^{-1}$
- Molar mass of the main gas (mugaz), $28kg/kmol$
- Length of a day in seconds (unjours), $86400s$
- Number of days in a year (year_day), 365
- Planet perihelion distance (periheli), $150MMkm$
- Planet aphelion distance (aphelie), $150MMkm$
- Perihelion day (peri_day), 0
- Axial tilt/Obliquity (obliquit), $23°$
- Sea surface roughness length scale (Cd_mer), $0.01m$
- Soil surface roughness length scale (Cd_ter), $0.01m$
- Sea thermal inertia(I_mer), $3000Jm^{-3}K^{-1}$
- Soil thermal inertia(I_ter), $3000Jm^{-3}K^{-1}$
- Sea albedo (alb_mer), 0.112
- Soil albedo (alb_ter), 0.112
- Sea emissivity (emi_mer), 1

- Soil emissivity (emi_ter), 1
- Minimum turbulent kinetic energy (emin_turb), 10^{-16}
- Minimum turbulent mixing length (lmixmin), $100m$
- Attenuation of shortwave radiation coefficient (coefvis), .99
- Attenuation of longwave radiation coefficient (coefir), 0.08
- Radiation flag (callrad), true
- Turbulence flag (calldifv), true
- Convective adjustment flag (calladj), true
- Soil flag (callsoil), true
- Seasonal cycle flag (season), true
- Diurnal cycle flag (diurnal), true
- Display logging flag (lverbose), true
- Period lutings in days (period_sort), 1 day

It is important to note that beyond these input parameters, the physics package requires calls to initialization routines to determine the logistics of the grids.

A.2 Equilibrium state of the uncoupled physics model without seasons

Chapter 4 displays the equilibrium state of the uncoupled physics model with an axial tilt/obliquity of 23°. In chapter 6 some of the simulations are run without seasons (obliquity is 0°). Therefore the following figures will display the uncoupled physics model equilibrium results for the time series with an obliquity of 0°. All initial conditions and parameters are the same as presented in chapter 4, except for the axial tilt.

Figure A.1 displays the 30 year times series of the temperature averaged over the entire sphere, with zero obliquity, for every third vertical layer (11 layers). To check the steady state the standard deviation around the mean is computed for each layer. The deviation is less than 0.1% for all layers after 2 years. Therefore the temperature reaches a statistical equilibrium after 2 years, and differs from the results with seasons (figure 4.2) as it does not display the annual cycle.

Figure A.2a and A.2b plots the 30 year time series of both the average zonal and meridional velocity over the sphere, with zero obliquity, for every other layer of the lower 15 layers of the atmosphere of the model. The figures display that, without coupling to the dynamics, both velocities decay over the 30 years in the lower layers. Figure A.2c and A.2d displays the 30 year times series, from a simulation with zero axial tilt, of the averaged velocities of the upper layer velocities. A major difference between the

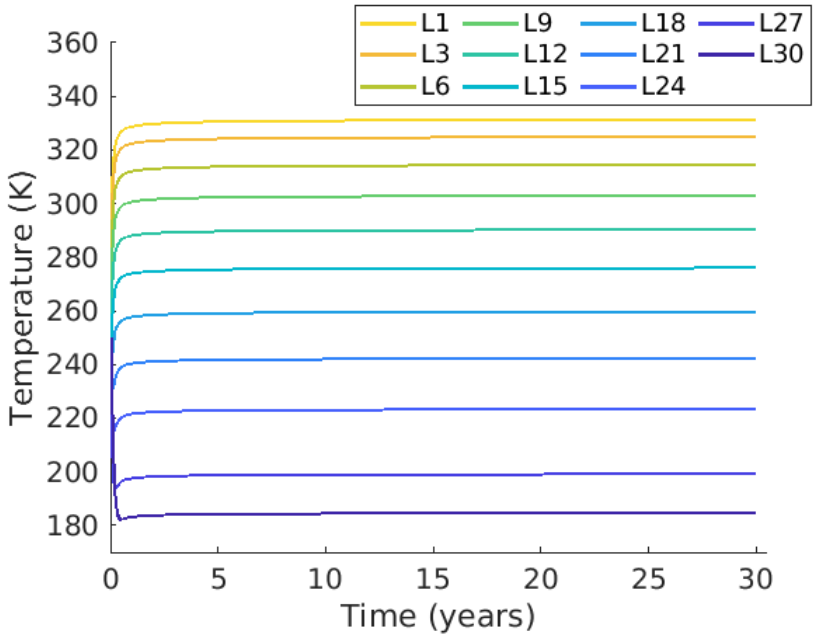

Figure A.1: 30 year time series of the average temperature over the sphere for every third layer out of the 30 layer atmosphere with zero axial tilt. The series displays the temperature reaching a statistical equilibrium.

velocities of the no season simulation and the season simulation, is that for the no season simulation more of the upper layers have little to no decay across the 30 years.

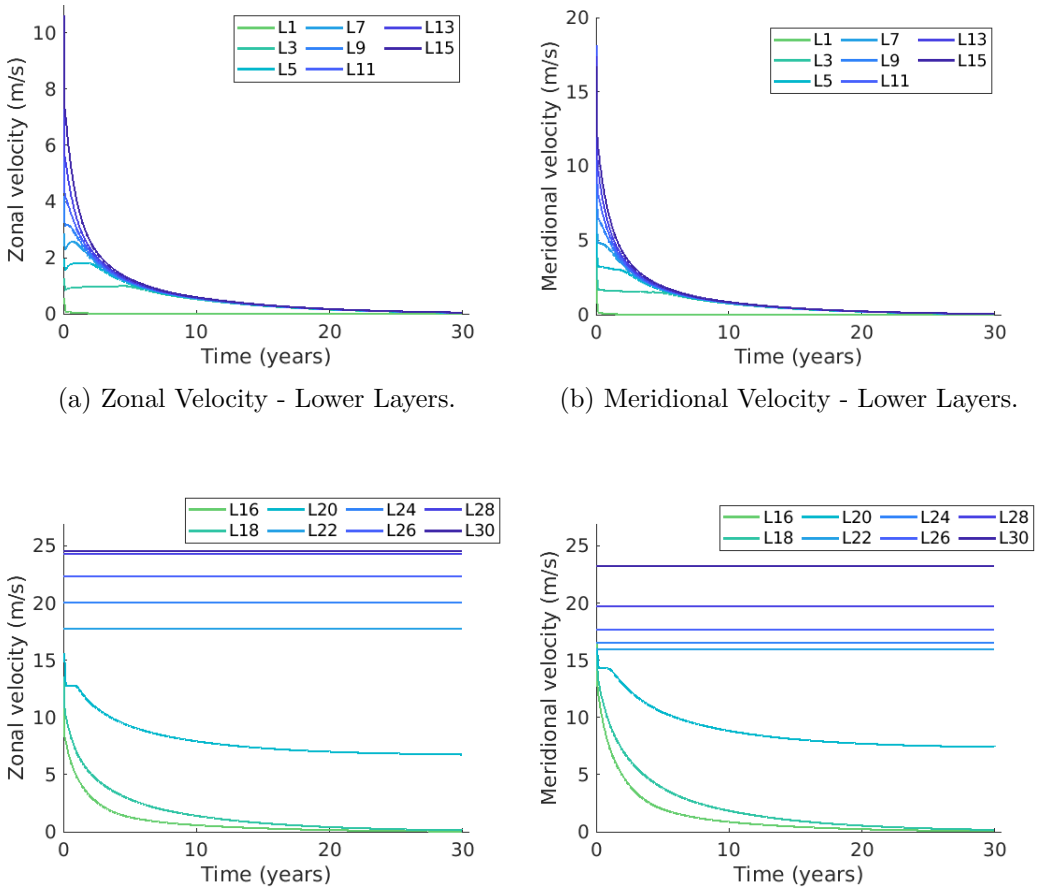

(a) Zonal Velocity - Lower Layers.

(b) Meridional Velocity - Lower Layers.

(c) Zonal Velocity - Upper Layers.

(d) Meridional Velocity - Upper Layers.

Figure A.2: Figures A.2a and A.2b displays average zonal and meridional velocity for alternating layers of the lower 15 layers. Figures A.2c and A.2d displays average zonal and meridional velocity for alternating layers of the upper 15 layers out of the total 30 layers for the simulations. All figures display a time series of the uncoupled physics package 30 year simulation with zero axial tilt.

Appendix B

Chapter 6 Supplementary Material

B.1 Soil layer time periods

Table B.1 displays the time period of each soil layer. In general the soil layers have units of $s^{1/2}$ and the thermal inertia (I) for the simulations was 3000 $\mathrm{Js^{-1/2}m^{-2}K^{-1}}$. The heat capacity ($C_p$) and the thermal conductivity (λ) are implicitly implied through the thermal inertia. To present an example of the estimated depths of each soil layer, an approximate value for the heat capacity, was chosen for Earth and used to calculate the thermal conductivity and depth. A value of $C_p = 2.2 \times 10^6$ $\mathrm{Jm^{-2}K^{-1}}$ was chosen and the resultant thermal conductivity is $\lambda = 4.09$ $\mathrm{Js^{-1}m^{-2}K^{-1}}$. To calculate the depth (m), found in the table, the equation, $z' = -z\sqrt{C_p/\lambda}$ is used, where z' is the soil depth ($s^{1/2}$) used in the model and z is the soil depth (m).

Layer	Period	Depth (m)
1	5.56 h	0.108
2	2.08 days	0.326
3	11. 34 days	0.761
4	1.74 months	1.63
5	7.42 months	3.37
6	2.52 years	6.85
7	10.23 years	13.81
8	41.24 years	27.74
9	1.66 centuries	55.59
10	6.64 centuries	111.29

TABLE B.1: The time periods of each soil layer and an example of estimated depth. The model used the thermal inertial (I) of 3000 $\mathrm{Js^{-1/2}m^{-2}K^{-1}}$. The calculated depth in the table assumes a chosen heat capacity (C_p) of 2.2×10^6 $\mathrm{Jm^{-2}K^{-1}}$ and thermal conductivity (λ) of 4.09 $\mathrm{Js^{-1}m^{-2}K^{-1}}$.

B.2 Temperature difference due to soil layers

Table B.2 displays the difference in temperature at each atmospheric layer and the surface, between simulations with 10 soil layers and no soil layers. A negative value indicates the no soil layer simulation temperature is smaller than the 10 soil layer simulation temperature. In general the temperature results from the 10 soil layer simulation was colder than that of the no soil layer results. The average difference in temperature is approximately 1.7 K.

Table B.3 displays the difference in temperature between simulations with 7 soil layers and no soi layers. The negative values indicate the 7 soil layer simulation has a greater temperature than the no soil simulations. The average difference in temperature is approximately 0.81 K.

Table B.4 displays the difference in temperature at each atmospheric layer between a simulation with 4 soil levels and no soil levels. The negative values indicate a greater temperature in the 4 soil layer simulation compared to the no soil simulation. The average difference in temperature is approximately 0.38 K.

B.3 Temperature 5 year coupling and uncoupling difference

Table B.5 displays the difference in temperature at 5 years of the coupled and uncoupled simulations of the physics package. The negative values indicate the uncoupled simulation had a higher temperature at the layer. The largest difference was at the top atmospheric layer.

B.4 Zonal and meridional kinetic energy (KE) 10 year time series

The Zonal and Meridional KE time series from figures 6.8 and 6.9 displayed the five year time series with a long fluctuation. To observe that it is indeed a fluctuation and a steady state is reached, the following figures (figure B.1 & B.2) display the ten year time series. From both time series, it can be observed that a steady state is reached by three years.

B.5 Grid convergence temperature differences for all layers

Table B.6 displays the absolute value of the difference in temperature between the coarsest resolutions of 4° ($\sim$ 480 km), 2° ($\sim$ 240 km) and 1° ($\sim$ 120 km) and the reference resolution of 0.5° ($\sim$ 60 km) for all atmospheric layers. The trend displayed is a decrease in temperature difference as the resolution approaches the reference resolution.

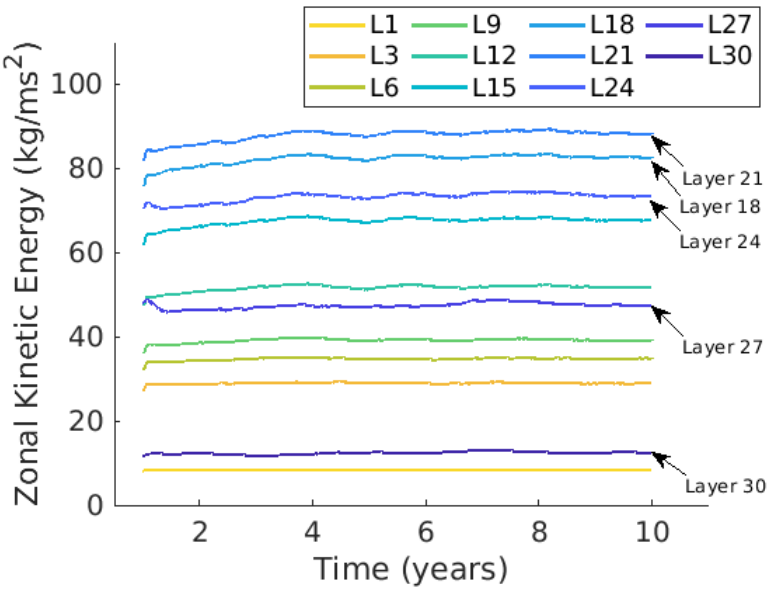

FIGURE B.1: Ten year time series with a 1 year running average of the zonal KE for every third atmospheric vertical layer. 'Lk' represents layer k out of 30 and the simulation contained a 2° horizontal resolution. The time series results are from the simulation including the soil model with 10 layers.

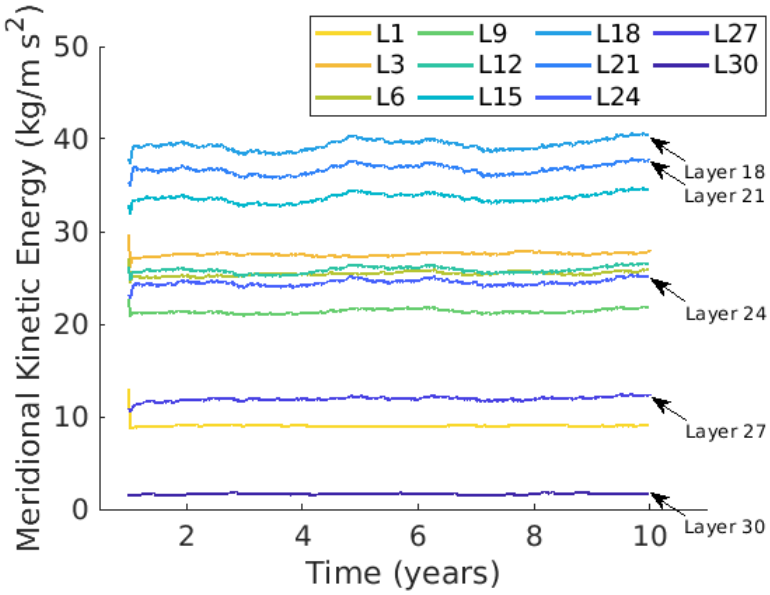

FIGURE B.2: 10 year time series with a 1 year running average of the meridional KE for every third atmospheric vertical layer. 'Lk' represents layer k out of the total 30 layers. The simulation had a 2° horizontal resolution and included a soil model with 10 layers.

Layer	Pressure (Pa)	Temperature Difference (K)
0	100 000	$-1.2127 \cdot 10^{0}$
1	$9.8333 \cdot 10^{4}$	$7.1086 \cdot 10^{-1}$
2	$9.5 \cdot 10^{4}$	$1.3278 \cdot 10^{0}$
3	$9.1667 \cdot 10^{4}$	$1.6185 \cdot 10^{0}$
4	$8.8333 \cdot 10^{4}$	$1.7978 \cdot 10^{0}$
5	$8.5 \cdot 10^{4}$	$1.9183 \cdot 10^{0}$
6	$8.1667 \cdot 10^{4}$	$2.008 \cdot 10^{0}$
7	$7.8333 \cdot 10^{4}$	$2.0759 \cdot 10^{0}$
8	$7.5 \cdot 10^{4}$	$2.1248 \cdot 10^{0}$
9	$7.1667 \cdot 10^{4}$	$2.1564 \cdot 10^{0}$
10	$6.8333 \cdot 10^{4}$	$2.1734 \cdot 10^{0}$
11	$6.5 \cdot 10^{4}$	$2.1786 \cdot 10^{0}$
12	$6.1667 \cdot 10^{4}$	$2.1741 \cdot 10^{0}$
13	$5.8333 \cdot 10^{4}$	$2.1618 \cdot 10^{0}$
14	$5.5 \cdot 10^{4}$	$2.1434 \cdot 10^{0}$
15	$5.1667 \cdot 10^{4}$	$2.1201 \cdot 10^{0}$
16	$4.8333 \cdot 10^{4}$	$2.0927 \cdot 10^{0}$
17	$4.5 \cdot 10^{4}$	$2.0618 \cdot 10^{0}$
18	$4.1667 \cdot 10^{4}$	$2.0271 \cdot 10^{0}$
19	$3.8333 \cdot 10^{4}$	$1.9872 \cdot 10^{0}$
20	$3.5 \cdot 10^{4}$	$1.9393 \cdot 10^{0}$
21	$3.1667 \cdot 10^{4}$	$1.8773 \cdot 10^{0}$
22	$2.8333 \cdot 10^{4}$	$1.7945 \cdot 10^{0}$
23	$2.5 \cdot 10^{4}$	$1.6922 \cdot 10^{0}$
24	$2.1667 \cdot 10^{4}$	$1.5998 \cdot 10^{0}$
25	$1.8333 \cdot 10^{4}$	$1.5459 \cdot 10^{0}$
26	$1.5 \cdot 10^{4}$	$1.5303 \cdot 10^{0}$
27	$1.1667 \cdot 10^{4}$	$1.4787 \cdot 10^{0}$
28	$8.3333 \cdot 10^{3}$	$1.5932 \cdot 10^{0}$
29	$5 \cdot 10^{3}$	$1.5713 \cdot 10^{0}$
30	$1.6667 \cdot 10^{3}$	$2.7466 \cdot 10^{-1}$

Table B.2: Differences at each atmospheric layer and the surface in the temperature profile of a simulation with 10 soil layers and a simulation with no soil layers. A negative value indicates the no soil layer simulation temperature is smaller than the 10 soil layer simulation temperature. The average difference in temperature is approximately 1.7 K.

Layer	Pressure (Pa)	Temperature Difference (K)
0	100 000	$-2.2861 \cdot 10^{0}$
1	$9.8333 \cdot 10^{4}$	$-3.0631 \cdot 10^{-1}$
2	$9.5 \cdot 10^{4}$	$3.3056 \cdot 10^{-1}$
3	$9.1667 \cdot 10^{4}$	$6.3332 \cdot 10^{-1}$
4	$8.8333 \cdot 10^{4}$	$8.1939 \cdot 10^{-1}$
5	$8.5 \cdot 10^{4}$	$9.435 \cdot 10^{-1}$
6	$8.1667 \cdot 10^{4}$	$1.0349 \cdot 10^{0}$
7	$7.8333 \cdot 10^{4}$	$1.1034 \cdot 10^{0}$
8	$7.5 \cdot 10^{4}$	$1.1524 \cdot 10^{0}$
9	$7.1667 \cdot 10^{4}$	$1.1843 \cdot 10^{0}$
10	$6.8333 \cdot 10^{4}$	$1.2023 \cdot 10^{0}$
11	$6.5 \cdot 10^{4}$	$1.2093 \cdot 10^{0}$
12	$6.1667 \cdot 10^{4}$	$1.2077 \cdot 10^{0}$
13	$5.8333 \cdot 10^{4}$	$1.1995 \cdot 10^{0}$
14	$5.5 \cdot 10^{4}$	$1.1865 \cdot 10^{0}$
15	$5.1667 \cdot 10^{4}$	$1.1699 \cdot 10^{0}$
16	$4.8333 \cdot 10^{4}$	$1.1511 \cdot 10^{0}$
17	$4.5 \cdot 10^{4}$	$1.1307 \cdot 10^{0}$
18	$4.1667 \cdot 10^{4}$	$1.1087 \cdot 10^{0}$
19	$3.8333 \cdot 10^{4}$	$1.0839 \cdot 10^{0}$
20	$3.5 \cdot 10^{4}$	$1.054 \cdot 10^{0}$
21	$3.1667 \cdot 10^{4}$	$1.0142 \cdot 10^{0}$
22	$2.8333 \cdot 10^{4}$	$9.5804 \cdot 10^{-1}$
23	$2.5 \cdot 10^{4}$	$8.8486 \cdot 10^{-1}$
24	$2.1667 \cdot 10^{4}$	$8.2268 \cdot 10^{-1}$
25	$1.8333 \cdot 10^{4}$	$7.9807 \cdot 10^{-1}$
26	$1.5 \cdot 10^{4}$	$8.1198 \cdot 10^{-1}$
27	$1.1667 \cdot 10^{4}$	$7.7948 \cdot 10^{-1}$
28	$8.3333 \cdot 10^{3}$	$9.1863 \cdot 10^{-1}$
29	$5 \cdot 10^{3}$	$9.3034 \cdot 10^{-1}$
30	$1.6667 \cdot 10^{3}$	$-1.9403 \cdot 10^{-1}$

Table B.3: Differences at each atmospheric layer and the surface in the temperature profile of a simulation with 7 soil layers and a simulation with no soil layers. A negative value indicates the no soil layer simulation temperature is smaller than the 7 soil layer simulation temperature. The average difference in temperature is approximately 0.81 K.

Layer	Pressure (Pa)	Temperature Difference (K)
0	100 000	$-2.8031 \cdot 10^{0}$
1	$9.8333 \cdot 10^{4}$	$-8.0588 \cdot 10^{-1}$
2	$9.5 \cdot 10^{4}$	$-1.6497 \cdot 10^{-1}$
3	$9.1667 \cdot 10^{4}$	$1.4194 \cdot 10^{-1}$
4	$8.8333 \cdot 10^{4}$	$3.3084 \cdot 10^{-1}$
5	$8.5 \cdot 10^{4}$	$4.5609 \cdot 10^{-1}$
6	$8.1667 \cdot 10^{4}$	$5.4851 \cdot 10^{-1}$
7	$7.8333 \cdot 10^{4}$	$6.1876 \cdot 10^{-1}$
8	$7.5 \cdot 10^{4}$	$6.7069 \cdot 10^{-1}$
9	$7.1667 \cdot 10^{4}$	$7.0645 \cdot 10^{-1}$
10	$6.8333 \cdot 10^{4}$	$7.2868 \cdot 10^{-1}$
11	$6.5 \cdot 10^{4}$	$7.4016 \cdot 10^{-1}$
12	$6.1667 \cdot 10^{4}$	$7.434 \cdot 10^{-1}$
13	$5.8333 \cdot 10^{4}$	$7.4046 \cdot 10^{-1}$
14	$5.5 \cdot 10^{4}$	$7.33 \cdot 10^{-1}$
15	$5.1667 \cdot 10^{4}$	$7.2252 \cdot 10^{-1}$
16	$4.8333 \cdot 10^{4}$	$7.1019 \cdot 10^{-1}$
17	$4.5 \cdot 10^{4}$	$6.9661 \cdot 10^{-1}$
18	$4.1667 \cdot 10^{4}$	$6.8176 \cdot 10^{-1}$
19	$3.8333 \cdot 10^{4}$	$6.6475 \cdot 10^{-1}$
20	$3.5 \cdot 10^{4}$	$6.4337 \cdot 10^{-1}$
21	$3.1667 \cdot 10^{4}$	$6.1317 \cdot 10^{-1}$
22	$2.8333 \cdot 10^{4}$	$5.6784 \cdot 10^{-1}$
23	$2.5 \cdot 10^{4}$	$5.0666 \cdot 10^{-1}$
24	$2.1667 \cdot 10^{4}$	$4.5463 \cdot 10^{-1}$
25	$1.8333 \cdot 10^{4}$	$4.3576 \cdot 10^{-1}$
26	$1.5 \cdot 10^{4}$	$4.5193 \cdot 10^{-1}$
27	$1.1667 \cdot 10^{4}$	$4.2148 \cdot 10^{-1}$
28	$8.3333 \cdot 10^{3}$	$5.9992 \cdot 10^{-1}$
29	$5 \cdot 10^{3}$	$6.7286 \cdot 10^{-1}$
30	$1.6667 \cdot 10^{3}$	$-5.6679 \cdot 10^{-1}$

Table B.4: Differences at each atmospheric layer and the surface in the temperature profile of a simulation with 4 soil layers and a simulation with no soil layers. The negative values indicate a greater temperature in the 4 soil layer simulation compared to the no soil simulation. The average difference in temperature is approximately 0.38K.

Layer	Pressure (Pa)	Temperature Difference (K)
1	98,333.33	−1.26
2	95,000	−1.01
3	91,666.67	−0.68
4	88,333.33	−0.32
5	85,000	$3.47 \cdot 10^{-2}$
6	81,666.67	0.39
7	78,333.34	0.78
8	75,000	1.19
9	71,666.67	1.62
10	68,333.34	2.05
11	65,000	2.49
12	61,666.67	2.93
13	58,333.34	3.37
14	55,000	3.8
15	51,666.67	4.24
16	48,333.34	4.68
17	45,000.01	5.12
18	41,666.67	5.57
19	38,333.34	5.88
20	35,000.01	5.78
21	31,666.67	5.46
22	28,333.34	5.06
23	25,000.01	4.66
24	21,666.67	4.34
25	18,333.34	4.11
26	15,000.01	4.03
27	11,666.68	4.49
28	8,333.34	6.18
29	5,000.01	14.9
30	1,666.68	−15.57

Table B.5: Differences at each atmospheric layer in the temperature at 5 years of the coupled and uncoupled simulations. The negative values indicate the uncoupled simulation had a higher temperature at the layer. The largest difference was at the top atmospheric layer.

Layer	Pressure (Pa)	4 Degree Error (K)	2 Degree Error (K)	1 Degree Error (K)
1	98,333.33	0.41	0.21	$6.01 \cdot 10^{-3}$
2	95,000	0.47	0.26	$1.14 \cdot 10^{-2}$
3	91,666.67	0.46	0.27	$1.62 \cdot 10^{-2}$
4	88,333.33	0.38	0.22	$7.27 \cdot 10^{-3}$
5	85,000	0.29	0.16	$1.77 \cdot 10^{-2}$
6	81,666.67	0.19	$7.73 \cdot 10^{-2}$	$3.84 \cdot 10^{-2}$
7	78,333.34	$9.12 \cdot 10^{-2}$	$7.81 \cdot 10^{-3}$	$4.12 \cdot 10^{-2}$
8	75,000	$2.91 \cdot 10^{-3}$	$4.67 \cdot 10^{-2}$	$3.61 \cdot 10^{-2}$
9	71,666.67	$7.27 \cdot 10^{-2}$	$8.06 \cdot 10^{-2}$	$3.21 \cdot 10^{-2}$
10	68,333.34	0.15	0.1	$2.73 \cdot 10^{-2}$
11	65,000	0.21	0.11	$2.51 \cdot 10^{-2}$
12	61,666.67	0.26	0.13	$2.62 \cdot 10^{-2}$
13	58,333.34	0.31	0.14	$3.3 \cdot 10^{-2}$
14	55,000	0.35	0.15	$4.54 \cdot 10^{-2}$
15	51,666.67	0.38	0.17	$6.15 \cdot 10^{-2}$
16	48,333.34	0.4	0.18	$7.81 \cdot 10^{-2}$
17	45,000.01	0.39	0.19	$8.94 \cdot 10^{-2}$
18	41,666.67	0.37	0.2	$9.33 \cdot 10^{-2}$
19	38,333.34	0.33	0.2	$9.04 \cdot 10^{-2}$
20	35,000.01	0.29	0.19	$7.62 \cdot 10^{-2}$
21	31,666.67	0.24	0.18	$5.2 \cdot 10^{-2}$
22	28,333.34	0.21	0.17	$2.67 \cdot 10^{-2}$
23	25,000.01	0.23	0.19	$4.11 \cdot 10^{-2}$
24	21,666.67	0.3	0.24	$6.57 \cdot 10^{-2}$
25	18,333.34	0.45	0.35	$8.81 \cdot 10^{-2}$
26	15,000.01	0.6	0.43	0.14
27	11,666.68	0.97	0.7	0.38
28	8,333.34	2.31	1.46	0.86
29	5,000.01	5.69	4.21	2.14
30	1,666.68	9.21	6.6	3.35

Table B.6: Differences at each atmospheric layer of the coarsest horizontal grid resolution (4° ($\sim$ 480 km), 2° ($\sim$ 240 km) and 1° ($\sim$ 120 km)) and the reference finest grid resolution of 0.5° ($\sim$ 60 km). The trend displayed is a decrease in temperature difference as the resolution approaches the reference resolution.

Bibliography

Aechtner, M., Kevlahan, N. K.-R., and Dubos, T. (Nov. 2014). A conservative adaptive wavelet method for the shallow-water equations on the sphere. *Quarterly Journal of the Royal Meteorological Society* 141(690), 1712–1726.

Amundsen, David S., Mayne, Nathan J., Baraffe, Isabelle, Manners, James, Tremblin, Pascal, Drummond, Benjamin, Smith, Chris, Acreman, David M., and Homeier, Derek (2016). The UK Met Office global circulation model with a sophisticated radiation scheme applied to the hot Jupiter HD 209458b. *A&A* 595, A36.

Chapter 4 Soil Temperatures and Heat Transfer (1988). In: *Introduction to Micrometeorology*. Ed. by S. P. Arya. Vol. 42. International Geophysics. Academic Press, 37–48.

Chen, D., Rojas, M., Samset, B., Cobb, K., Diongue Niang, A., Edwards, P., Emori, S., Faria, S., Hawkins, E., Hope, P., Huybrechts, P., Meinshausen, M., Mustafa, S., Plattner, G.-K., and Tréguier, A.-M. (2021). Framing, Context, and Methods. In: *Climate Change 2021: The Physical Science Basis. Contribution of Working Group I to the Sixth Assessment Report of the Intergovernmental Panel on Climate Change*. Ed. by V. Masson-Delmotte, P. Zhai, A. Pirani, S. L. Connors, C. Péan, S. Berger, N. Caud, Y. Chen, L. Goldfarb, M. I. Gomis, M. Huang, K. Leitzell, E. Lonnoy, J. B. R. Matthews, T. K. Maycock, T. Waterfield, O. Yelekçi, R. Yu, and B. Zhou. Cambridge, UK and New York, NY, USA: Cambridge University Press. Chap. 1.

Clark, S. K., Ming, Y., and Adames, Á. F. (2020). Monsoon Low Pressure System–Like Variability in an Idealized Moist Model. *Journal of Climate* 33(6), 2051–2074.

Clark, S. K., Ming, Y., Held, I. M., and Phillipps, P. J. (2018). The Role of the Water Vapor Feedback in the ITCZ Response to Hemispherically Asymmetric Forcings. *Journal of Climate* 31(9), 3659–3678.

Collins, S. N., James, R. S., Ray, P., Chen, K., Lassman, A., and Brownlee, J. (2013). Grids in Numerical Weather and Climate Models. In: *Climate Change and Regional/Local Responses*. Ed. by Y. Zhang and P. Ray. IntechOpen. Chap. 4.

St-Cyr, A., Jablonowski, C., Dennis, J. M., Tufo, H. M., and Thomas, S. J. (2008). A Comparison of Two Shallow-Water Models with Nonconforming Adaptive Grids. *Monthly Weather Review* 136(6), 1898–1922.

Dubal, M., Wood, N., and Staniforth, A. (2004). Analysis of Parallel versus Sequential Splittings for Time-Stepping Physical Parameterizations. *Monthly Weather Review* 132(1), 121–132.

Dubos, T. (Dec. 2021). private communication.

Ferguson, J. O., Jablonowski, C., Johansen, H., McCorquodale, P., Colella, P., and Ullrich, P. A. (2016). Analyzing the Adaptive Mesh Refinement (AMR) Characteristics

of a High-Order 2D Cubed-Sphere Shallow-Water Model. *Monthly Weather Review* 144(12), 4641–4666.

Flato, G., Marotzke, J., Abiodun, B., Braconnot, P., Chou, S., Collins, W., Cox, P., Driouech, F., Emori, S., Eyring, V., Forest, C., Gleckler, P., Guilyardi, E., Jakob, C., Kattsov, V., Reason, C., and Rummukainen, M. (2013). Evaluation of Climate Models. In: *Climate Change 2013: The Physical Science Basis. Contribution of Working Group I to the Fifth Assessment Report of the Intergovernmental Panel on Climate Change*. Ed. by T. Stocker, D. Qin, G.-K. Plattner, M. Tignor, S. Allen, J. Boschung, A. Nauels, Y. Xia, V. Bex, and P. Midgley. Cambridge, United Kingdom and New York, NY, USA: Cambridge University Press. Chap. 9, 741–866. ISBN: ISBN 978-1-107-66182-0.

Frassoni, A., Castilho, D., Rixen, M., Ramirez, E., Mattos, J. G. Z. de, Kubota, P., Calheiros, A. J. P., Reed, K. A., Silva Dias, M. A. F. da, Silva Dias, P. L. da, Campos Velho, H. F. de, Roode, S. R. de, Doblas-Reyes, F., Eiras, D., Ek, M., Figueroa, S. N., Forbes, R., Freitas, S. R., Grell, G. A., Herdies, D. L., Lauritzen, P. H., Machado, L. A. T., Manzi, A. O., Martins, G., Oliveira, G. S., Rosário, N. E., Sales, D. C., Wedi, N., and Yamada, B. (2018). Building the Next Generation of Climate Modelers: Scale-Aware Physics Parameterization and the "Grey Zone" Challenge. *Bulletin of the American Meteorological Society* 99(11), ES185–ES189.

Frierson, D. M. W., Held, I. M., and Zurita-Gotor, P. (2006). A Gray-Radiation Aquaplanet Moist GCM. Part I: Static Stability and Eddy Scale. *Journal of the Atmospheric Sciences* 63(10), 2548–2566.

Frierson, D. M. W., Held, I. M., and Zurita-Gotor, P. (2007). A Gray-Radiation Aquaplanet Moist GCM. Part II: Energy Transports in Altered Climates. *Journal of the Atmospheric Sciences* 64(5), 1680–1693.

Gettelman, A., Geer, A. J., Forbes, R. M., Carmichael, G. R., Feingold, G., Posselt, D. J., Stephens, G. L., Heever, S. C. van den, Varble, A. C., and Zuidema, P. (2022). The future of Earth system prediction: Advances in model-data fusion. *Science Advances* 8(14), eabn3488.

Gross, M., Malardel, S., Jablonowski, C., and Wood, N. (2016). Bridging the (Knowledge) Gap between Physics and Dynamics. *Bulletin of the American Meteorological Society* 97(1), 137–142.

Gross, M., Wan, H., Rasch, P. J., Caldwell, P. M., Williamson, D. L., Klocke, D., Jablonowski, C., Thatcher, D. R., Wood, N., Cullen, M., Beare, B., Willett, M., Lemarié, F., Blayo, E., Malardel, S., Termonia, P., Gassmann, A., Lauritzen, P. H., Johansen, H., Zarzycki, C. M., Sakaguchi, K., and Leung, R. (Oct. 2018). Physics–Dynamics Coupling in Weather, Climate, and Earth System Models: Challenges and Recent Progress. *Monthly Weather Review* 146(11), 3505–3544.

Guendelman, I. and Kaspi, Y. (Aug. 2019). Atmospheric Dynamics on Terrestrial Planets: The Seasonal Response to Changes in Orbital, Rotational, and Radiative Timescales. *The Astrophysical Journal* 881(1), 67.

Hammond, M. and Pierrehumbert, R. T. (Nov. 2017). Linking the Climate and Thermal Phase Curve of 55 Cancri e. *The Astrophysical Journal* 849(2), 152.

Haqq-Misra, J. and Heller, R. (June 2018). Exploring exomoon atmospheres with an idealized general circulation model. *Monthly Notices of the Royal Astronomical Society* 479(3), 3477–3489.

Held, I. (2005). The Gap Between Simulation and Understanding in Climate Modeling. *Bulletin of the American Meteorological Society* 86(11), 1609–1614.

Held, I. and Suarez, M. (1994). A Proposal for the Intercomparison of the Dynamical Cores of Atmospheric General Circulation Models. *Bulletin of the American Meteorological Society* 76(10), 1825–1830.

Heng, K., Frierson, D. M. W., and Phillipps, P. J. (Oct. 2011). Atmospheric circulation of tidally locked exoplanets: II. Dual-band radiative transfer and convective adjustment. *Monthly Notices of the Royal Astronomical Society* 418(4), 2669–2696.

Hong, H.-J. and Reichler, T. (2021). The Simplified Chemistry-Dynamical Model (SCDM V1.0). *Geoscientific Model Development* 14(10), 6647–6660.

Hourdin, F. (1992). Étude et simulation numérique de la circulation générale des atmosphères planétaires. PhD thesis. Université de Paris 7.

Innes, H. and Pierrehumbert, R. T. (Mar. 2022). Atmospheric Dynamics of Temperate Sub-Neptunes. I. Dry Dynamics. *The Astrophysical Journal* 927(1), 38.

Internantional Standard Atmosphere (2005). The Engineering ToolBox.

Izakov, M. (2012). On the Small Scale Turbulence Parameters in the Atmosphere of Venus and Their Use in the Global Circulation Models. *Solar System Research* 46, 278–290.

Jablonowski, C., Herzog, M., Penner, J., Oehmke, R., Stout, Q., and Leer, B. van (Jan. 2004). Adaptive Grids for Weather and Climate Models. In:

Jablonowski, C. and Williamson, D. L. (2006). A baroclinic instability test case for atmospheric model dynamical cores. *Quarterly Journal of the Royal Meteorological Society* 132(621C), 2943–2975.

Jeevanjee, N., Hassanzadeh, P., Hill, S., and Sheshadri, A. (July 2017). A perspective on climate model hierarchies. *Journal of Advances in Modeling Earth Systems* 9.

Jucker, M. and Gerber, E. P. (2017). Untangling the Annual Cycle of the Tropical Tropopause Layer with an Idealized Moist Model. *Journal of Climate* 30(18), 7339–7358.

Kent, J., Ullrich, P. A., and Jablonowski, C. (2014). Dynamical core model intercomparison project: Tracer transport test cases. *Quarterly Journal of the Royal Meteorological Society* 140(681), 1279–1293.

Kevlahan, N. K.-R. and Dubos, T. (2019). WAVETRISK-1.0: an adaptive wavelet hydrostatic dynamical core. *Geoscientific Model Development* 12(11), 4901–4921.

Koll, D. D. B. and Abbot, D. S. (Mar. 2015). Deciphering Thermal Phase Curves of Dry Tidally Locked Terrestrial Planets. *The Astrophysical Journal* 802(1), 21.

Komacek, T., Showman, A., and Tan, X. (Jan. 2017). Atmospheric Circulation of Hot Jupiters: Dayside-Nightside Temperature Differences. II. Comparison with Observations. *The Astrophysical Journal* 835.

Komacek, T. D. and Abbot, D. S. (Feb. 2019). The Atmospheric Circulation and Climate of Terrestrial Planets Orbiting Sun-like and M Dwarf Stars over a Broad Range of Planetary Parameters. *The Astrophysical Journal* (2), 245.

Komacek, T. D. and Showman, A. P. (Apr. 2016). Atmospheric Circulation of Hot Jupiters: Dayside-Nightside Temperature Differences. *The Astrophysical Journal* 821(1), 16.

Le Treut, H., Somerville, R., Cubasch, U., Ding, Y., Mauritzen, C., Mokssit, A., Peterson, A., and Prather, M. (2007). Historical Overview of Climate Change Science. In: *Climate Change 2007: The Physical Science Basis. Contribution of Working Group I to the Fourth Assessment Report of the Intergovernmental Panel on Climate Change*. Ed. by D. Griggs and B. A. Cambridge, United Kingdom and New York, NY, USA: Cambridge University Press. Chap. 1.

Lee, C., Lewis, S., and Read, P. (2007). Superrotation in a Venus general circulation model. *Journal of Geophysical Research:Planets* 112(E4).

Lee, G., Casewell, S., Chubb, K., Hammond, M., Tan, X., Tsai, S.-M., and Pierrehumbert, R. (Aug. 2020). Simplified 3D GCM modelling of the irradiated brown dwarf WD 0137349B. *Monthly Notices of the Royal Astronomical Society* 496, 4674–4687.

Louis, J. (1979). A parametric model of vertical eddy fluxes in the atmosphere. *Boundary-Layer Meteorology* 17, 187–202.

Maher, P., Gerber, E. P., Medeiros, B., Merlis, T. M., Sherwood, S. C., Sheshadri, A., Sobel, A. H., Vallis, G. K., Voigt, A., and Zurita-Gotor, P. (2019). Model Hierarchies for Understanding Atmospheric Circulation. *Reviews of Geophysics* 57, 250–280.

Mbengue, C. and Woollings, T. (2019). The Eddy-Driven Jet and Storm-Track Responses to Boundary Layer Drag: Insights from an Idealized Dry GCM Study. *Journal of the Atmospheric Sciences* 76(4), 1055–1076.

Mcfarlane, N. (July 2011). Parameterizations: Representing key processes in climate models without resolving them. *Wiley Interdisciplinary Reviews: Climate Change* 2.

Merlis, T., Schneider, T., Bordoni, S., and Eisenman, I. (2013a). Hadley Circulation Response to Orbital Precession. Part I: Aquaplanets. *Journal of Climate* 26(3), 740–753.

Merlis, T. M. and Schneider, T. (Apr. 2010). Atmospheric Dynamics of Earth-Like Tidally Locked Aquaplanets. *Journal of Advances in Modeling Earth Systems* 2(4).

Merlis, T. M., Schneider, T., Bordoni, S., and Eisenman, I. (2013b). Hadley Circulation Response to Orbital Precession. Part II: Subtropical Continent. *Journal of Climate* 26(3), 754–771.

O'Gorman, P. A. and Schneider, T. (2008). The Hydrological Cycle over a Wide Range of Climates Simulated with an Idealized GCM. *Journal of Climate* 21(15), 3815–3832.

Park, H., Kim, G., Cha, D.-H., Chang, E.-C., Kim, J., Park, S.-H., and Lee, D.-K. (2022). Effect of a Scale-Aware Convective Parameterization Scheme on the Simulation of Convective Cells-Related Heavy Rainfall in South Korea. *Journal of Advances in Modeling Earth Systems* 14(6). e2021MS002696 2021MS002696, e2021MS002696.

Pierrehumbert, R. T. (2010). *Principles of Planetary Climate*. Cambridge University Press.

Pierrehumbert, R. T. and Ding, F. (June 2016). Dynamics of atmospheres with a non-dilute condensible component. *Proceedings of the Royal Society A: Mathematical, Physical and Engineering Sciences* 472(2190), 20160107.

Polichtchouk, I., Cho, J.-K., Watkins, C., Thrastarson, H., Umurhan, O., and Torre Juárez, M. de la (Feb. 2014). Intercomparison of general circulation models for hot extrasolar planets. *Icarus* 229, 355–377.

Reed, K. A. and Jablonowski, C. (2012). Idealized tropical cyclone simulations of intermediate complexity: A test case for AGCMs. *Journal of Advances in Modeling Earth Systems* 4(2).

Rohli, R. V. and Li, C. (2021). Introduction to Near-Surface Atmospheric Dynamics. In: *Meteorology for Coastal Scientists*. Cham: Springer International Publishing, 347–353. ISBN: 978-3-030-73093-2.

Schneider, T. (2004). The Tropopause and the Thermal Stratification in the Extratropics of a Dry Atmosphere. *Journal of the Atmospheric Sciences* 61(12), 1317–1340.

Schneider, T. and Liu, J. (2009). Formation of Jets and Equatorial Superrotation on Jupiter. *Journal of the Atmospheric Sciences* 66(3), 579–601.

Schneider, T. and Walker, C. C. (2006). Self-Organization of Atmospheric Macroturbulence into Critical States of Weak Nonlinear Eddy–Eddy Interactions. *Journal of the Atmospheric Sciences* 63(6), 1569–1586.

Showman, A., Fortney, J., Lian, Y., Marley, M., Freedman, R., Knutson, H., and Charbonneau, D. (June 2009). Atmospheric Circulation of Hot Jupiters: Coupled Radiative-Dynamical General Circulation Model Simulations of HD 189733b and HD 209458b. *Astrophysical Journal - ASTROPHYS J* 699.

Showman, A. P., Tan, X., and Parmentier, V. (Dec. 2020). Atmospheric Dynamics of Hot Giant Planets and Brown Dwarfs. *Space Science Reviews* 216(8).

Skamarock, W., Oliger, J., and Street, R. L. (1989). Adaptive grid refinement for numerical weather prediction. *Journal of Computational Physics* 80(1), 27–60. ISSN: 0021-9991.

Stull, R. (1988). Turbulence Closure Techniques. In: *An Introduction to Boundary Layer Meteorology*. Dordrecht, The Netherlands: Kluwer Academic Publishers, 197–250.

Tan, X. and Komacek, T. D. (Nov. 2019). The Atmospheric Circulation of Ultra-hot Jupiters. *The Astrophysical Journal* 886(1), 26.

Temam, R. and Miranville, A. (2005). *Mathematical Modeling in Continuum Mechanics*. 2nd ed. Cambridge University Press, 189.

Temam, R. and Ziane, M. (2005). Chapter 6 - Some Mathematical Problems in Geophysical Fluid Dynamics. In: ed. by S. Friedlander and D. Serre. Vol. 3. Handbook of Mathematical Fluid Dynamics. North-Holland, 535–658.

Thatcher, D. R. and Jablonowski, C. (2016). A moist aquaplanet variant of the Held–Suarez test for atmospheric model dynamical cores. *Geoscientific Model Development* 9(4), 1263–1292.

Ullrich, P. A., Jablonowski, C., Kent, J., Lauritzen, P. H., Nair, R., Reed, K. A., Zarzycki, C. M., Hall, D. M., Dazlich, D., Heikes, R., Konor, C., Randall, D., Dubos, T., Meurdesoif, Y., Chen, X., Harris, L., Kühnlein, C., Lee, V., Qaddouri, A., Girard, C., Giorgetta, M., Reinert, D., Klemp, J., Park, S.-H., Skamarock, W., Miura, H., Ohno, T., Yoshida, R., Walko, R., Reinecke, A., and Viner, K. (2017). DCMIP2016: a review of non-hydrostatic dynamical core design and intercomparison of participating models. *Geoscientific Model Development* 10(12), 4477–4509.

Willson, J. L., Reed, K. A., Jablonowski, C., Kent, J., Lauritzen, P. H., Nair, R., Taylor, M. A., Ullrich, P. A., Zarzycki, C. M., Hall, D. M., Dazlich, D., Heikes, R., Konor, C., Randall, D., Dubos, T., Meurdesoif, Y., Chen, X., Harris, L., Kühnlein, C., Lee, V., Qaddouri, A., Girard, C., Giorgetta, M., Reinert, D., Miura, H., Ohno, T., and Yoshida, R. (2023). DCMIP2016: the tropical cyclone test case. *Geoscientific Model Development Discussions* 2023, 1–27.